8-16-2011 12:00 AM

Microrheology and microstructure of poly(vinyl alcohol)-based physical gels

Nan Yang, *The University of Western Ontario*

Supervisor: Jeffrey L. Hutter, *The University of Western Ontario*
Joint Supervisor: John R. de Bruyn, *The University of Western Ontario*
A thesis submitted in partial fulfillment of the requirements for the Doctor of Philosophy degree in Physics

Microrheology and microstructure of poly(vinyl alcohol)-based physical gels

(Spine Title: Microrheology of physical gels)

(Thesis Format: Integrated-Article)

by

Nan Yang

Graduate Program in Physics

A thesis submitted in partial fulfillment
of the requirements for the degree of
Doctor of Philosophy

The School of Graduate and Postdoctoral Studies
The University of Western Ontario
London, Ontario, Canada

THE UNIVERSITY OF WESTERN ONTARIO
THE SCHOOL OF GRADUATE AND POSTDOCTORAL STUDIES

CERTIFICATE OF EXAMINATION

Supervisors

Dr. Jeffrey L. Hutter

Dr. John R. de Bruyn

Advisory Committee

Dr. Lyudmila Goncharova

Examiners

Dr. Richard Holt

Dr. Michael Cottam

Dr. Jin Zhang

Dr. Anand Yethiraj

The thesis by

Nan Yang

entitled:

MICRORHEOLOGY AND MICROSTRUCTURE OF POLY(VINYL ALCOHOL)-BASED PHYSICAL GELS

is accepted in partial fulfillment of the
requirements for the degree of
Doctor of Philosophy

Date

Chair of the Thesis Examination Board

ABSTRACT

We study the microrheology and microstructure of physically cross-linked poly(vinyl alcohol) (PVA) gels using atomic force microscopy, dynamic light scattering and particle tracking. We compare the microscopic rheological properties with the bulk properties measured using conventional shear rheometry, and correlate the rheological properties to the structure of the materials.

We develop a new technique for investigating the viscoelastic properties of soft materials using the atomic force microscope. The electronic feedback of an atomic force microscope is modified by adding a small oscillatory voltage to the deflection signal, and the amplitude and phase of the motion of the sample stage is monitored by a lock-in amplifier to determine the viscous and elastic moduli of the sample. We apply this method to PVA hydrogels and suspended PVA nanofibers. We find the moduli of both the fibers and the hydrogels to show a significant frequency dependence.

We perform rheological and dynamic light scattering measurements on PVA/poly(ethylene glycol) (PEG) blends during aging. The properties of the blends change much faster with age than those of the pure PVA solution, and the blends undergo phase separation and gel over time. From dynamic light scattering experiments, we observe changes of the relaxation times in the blends as they age. We determine the gel point on the microscopic scale from the depression of the intensity autocorrelation function of the scattered light. We find that gelation of the PVA/PEG blends is induced by the growth of aggregates in the blends. By comparing the gel point determined by light scattering to that from the rheometry, we find that the macroscopic gel point is earlier than the microscopic one, indicating that the gel transition is length-scale dependent.

Particle tracking microrheology is used to investigate the microrheology and microstructure of these PVA/PEG blends as a function of PEG concentration and aging time. Dynamic light scattering probes the ensemble–averaged motion of all tracer particles in the scattering volume, while particle tracking tracks the motion of many individual tracers. The local

viscoelastic moduli are determined from the measurements using the generalized Stokes-Einstein relation. We find that addition of PEG to the PVA solutions influences the micro–environment significantly, and that phase separation happens before gelation as the blends age. We again find that the microscopic gel point occurs later than the macroscopic one, confirming the above results. The experimental results are consistent with a model in which the PVA/PEG blends consist of PVA-poor pores within a continuous PVA-rich domain which gels.

Keywords: Soft materials, physical gels, atomic force microscopy, rheology, microrheology, dynamic light scattering, particle tracking, viscoelasticity, phase separation, gelation.

STATEMENT OF CO-AUTHORSHIP

Chapters 4–6 in this thesis are based on the following papers:

N. Yang, K. K. H. Wong, J. R. de Bruyn and J. L. Hutter, Meas. Sci. Technol. **20**, 025703 (2009).

N. Yang, J. L. Hutter and J. R. de Bruyn, in preparation.

N. Yang, J. L. Hutter and J. R. de Bruyn, submitted to J. Rheology.

For all three papers, I carried out all the necessary experiments including sample preparation, measurements, data collection and analysis. I also wrote the manuscripts of all the papers. Dr. J. L. Hutter and Dr. J. R. de Bruyn supervised my work and revised the manuscripts. Dr. K. K. H. Wong provided the poly(vinyl alcohol) nanofibers used in the first paper.

ACKNOWLEDGEMENTS

I would like to acknowledge my supervisors Dr. Jeffrey L Hutter and Dr. John de Bruyn for introducing me to the interesting field of soft materials and rheology. I greatly appreciate their support, encouragement, and careful supervision throughout this research.

Special thanks go to the Natural Sciences and Engineering Research Council of Canada and the University of Western Ontario for funding this research. My thanks also go to my fellow graduate students in Dr. Hutter's group and Dr. de Bruyn's group and special thanks and memory to Dr. Ken K. H. Wong. The time spent with them in learning and discussions was really enjoyable.

I am highly indebted to my husband Junji Jia for his love and support. I thank him for his understanding and help. Without his helpful discussions and encouragement, I could not have finished this work as smoothly. I thank my lovely son Justin Jia, who brings me so much happiness. I also appreciate the help and support I have received from my parents and my parents-in-law during my studies.

TABLE OF CONTENTS

LIST OF FIGURES

LIST OF TABLES

Chapter 1

Introduction

1.1 Viscoelastic Properties of Soft Materials

Complex fluids such as polymer solutions, gels, emulsions, and colloidal suspensions play a ubiquitous role in everyday life. They encompass biomaterials, foods, personal care products, and a range of industrial products [1]. Complex fluids were first referred to as "soft" materials by P.-G. de Gennes in his Nobel lecture [2]. These materials can both store and dissipate energy when deformed by an external force. A simple solid stores energy in response to applied stress and behaves as a Hookean spring, while a simple liquid dissipates energy through viscous Newtonian flow [1]. Most soft materials exhibit both solid-like and liquid-like responses, which generally depend on the time scale or frequency at which the sample is probed. These materials are thus viscoelastic [3].

One intriguing example of a soft material is Silly Putty, which is a silicone polymer used as a toy for children. Silly Putty behaves like a solid on short time scales, but like a liquid over long times [4]. The liquid-like behavior can be seen clearly by allowing a ball of Silly Putty to relax on a wide-mesh screen. The material will flow through the screen over a matter of hours. On the other hand, it holds its own shape like a solid if we examine it over a period of seconds or minutes. Moreover, it has elasticity like a solid rubber ball, bouncing when thrown to the floor and partially retracting when pulled and then released [4].

Soft materials exhibit complicated flow properties which distinguish them from other materials [1]. Here, we use "flow" to refer to a smooth, irreversible deformation on an accessible time scale. Solids will not flow, but rather deform elastically under modest stresses and deform irreversibly or fracture under larger stress. Liquids will always flow viscously no matter how small the applied stress. The flow behavior of a complex fluid is not this simple. For example, honey is a fluid that has high viscosity, but is nonetheless Newtonian. If one disturbs the surface of honey in a jar, it will slowly return to its original, level shape under the force of gravity. In contrast, mayonnaise behaves quite differently. A perturbed mayonnaise surface remains perturbed minutes or even a year after it has been disturbed. Materials like mayonnaise are solid-like under moderate stress and will flow only when the applied stress exceeds a threshold value called the yield stress. The existence of a yield stress means that a non-zero stress is required to cause flow, and the stress must remain above the yield stress for sustained flow.

Examples of complex fluids also include biomaterials such as blood and personal care products such as shampoo and toothpaste [1]. The flow behavior of blood is shear-rate-dependent due to the presence of the red blood cells. At modest shear rates, the flow and orientation of the red blood cells are similar to those of rigid disks, while at higher shear rates they deform to resemble fluid droplets. The viscoelastic properties of blood are important to the human body as they determine the pumping load on the heart. The behavior of personal care products can be controlled by varying their compositions. Shampoos are designed to flow readily, but not too quickly, from the tube or bottle into one's hand. Toothpaste must flow out of the tube only when squeezed, and stop flowing and hold its shape immediately after it has been applied to the brush.

Polymers are also soft materials with viscoelastic character. Solid plastic products, parts, and packaging, whether injection-molded polycarbonate compact laser disks, high-strength fibers spun from liquid crystalline polymer, or soda bottles containing polyethylene terephthalate, are all processed in the fluid state, either molten or in solution. The polymer molecules are one component of a complex fluid whose viscoelastic properties determine the ease and

expense of processing, and to some extent, the properties of the final products [1].

Overall, soft materials have mechanical behavior intermediate between simple liquids and solids. Most are solids at short times and liquids at long times. The characteristic time required for them to change from "solid" to "liquid" varies from fractions of a second to days, or even years, depending on the fluid. Some complex fluids change from solid-like to liquid-like when subjected to a modest deformation, such as particulate and polymeric gels [1]. Others, such as electrorheological and magnetorheological suspensions, will change from liquid-like to solid-like when an electric or magnetic field is applied [1].

1.2 Rheology

Rheology is the study of the viscoelasticity of materials. It can be defined as the measurement and study of the relationship between the deformation (strain) of a material and the stress [1, 4]. This field involves inquiry into the flow behavior of complex fluids such as polymers, foods, biological systems, and other compounds. The relation between stress and deformation for these materials differs from Newton's law of viscosity, which describes the shear behavior of simple liquids:

$$\sigma = \eta\dot{\gamma}, \tag{1.1}$$

where σ is the stress, η is a constant of proportionality called the Newtonian viscosity, γ is the strain, or relative change in length, and $\dot{\gamma} = d\gamma/dt$ is the rate of strain. Newton's law thus states that the stress is proportional to $\dot{\gamma}$.

The relationship between stress and deformation of complex materials also differs from Hooke's law of elasticity, the relationship that holds for metals and other elastic materials,

$$\sigma = G\gamma, \tag{1.2}$$

where G is a constant of proportionality called the elastic modulus. G is an intrinsic property

of the solid material [1].

Instead, the relationship between the stress and strain of a complex fluid is intermediate between these two limiting cases. A major goal of rheology is to determine the equations, referred to as constitutive equations, that correctly describe the behavior of particular materials. These are often based on combinations and generalizations of the above equations.

Satisfactory constitutive equations can be determined through experiments. For example, one can apply a shear deformation and measure the resultant stress as a function of the shear rate. The functions of the kinematic parameters that characterize the rheological behavior of fluids are called rheological material functions. One commonly used material function relates the constant strain rate $\dot{\gamma}$ in a steady flow experiment to the shear stress σ. For a Newtonian fluid, the stress σ is constant and the material function is

$$\eta = \frac{\sigma}{\dot{\gamma}}. \tag{1.3}$$

η is therefore also constant and independent of $\dot{\gamma}$. For non-Newtonian fluids, on the other hand, viscosity will be a function of shear rate, i.e., $\eta = \eta(\dot{\gamma})$. If η decreases with $\dot{\gamma}$, the material is called shear thinning. If η increases with $\dot{\gamma}$, in contrast, it is called shear thickening.

Two other material functions widely used to characterize the viscoelastic properties of soft materials describe their response to small amplitude oscillatory shear (SAOS). They are defined based on an imposed sinusoidal shear strain

$$\gamma = \gamma_0 \sin(\omega t), \tag{1.4}$$

and the resulting shear stress

$$\begin{aligned} \sigma &= \sigma_0 \sin(\omega t + \delta) \\ &= (\sigma_0 \cos\delta) \sin\omega t + (\sigma_0 \sin\delta) \cos\omega t, \end{aligned} \tag{1.5}$$

where δ is the phase difference between the applied strain and the stress response. From Eqs. (1.4) and (1.5) one can derive expressions for the storage modulus $G'(\omega)$ and the loss modulus $G''(\omega)$:

$$G'(\omega) = \frac{\sigma_0}{\gamma_0} \cos \delta, \tag{1.6}$$

and

$$G''(\omega) = \frac{\sigma_0}{\gamma_0} \sin \delta. \tag{1.7}$$

G' is thus the amplitude of the component of the oscillatory stress that is in phase with the applied strain divided by the amplitude of the strain oscillation. G'' is defined analogously as the amplitude of the stress component that is out of phase with the strain, divided by the amplitude of the strain. For a Newtonian fluid in SAOS, the response is completely out of phase with the strain, so $G' = 0$ and $\eta = \sigma/\dot{\gamma} = G''/\omega$. For an elastic solid that follows Hooke's law, the shear-stress response in SAOS is completely in phase with the strain: $G' = G$ and $G'' = 0$.

Transient rheological measurements are also common. They include stress relaxation measurements, in which a constant strain γ is applied for a certain time, then released, allowing a time-dependent relaxation modulus $G(t)$ to be measured as $G(t) = \sigma(t)/\gamma$, where $\sigma(t)$ is the time-dependent stress. In a creep test, a constant stress is applied to the material and the resultant time-dependent strain is measured.

1.3 Rheological Behavior of Polymer Materials

As discussed above, the rheological properties of soft materials can be characterized by experimentally–determined material functions. Most polymeric fluids are non-Newtonian, and their viscosity is not constant. Instead, they show strong viscoelastic effects, typically including shear thinning and rate-dependent rheology. This behavior arises because the molecules are long and can rearrange during flow. Fig. 1.1 shows the viscosity η as a function

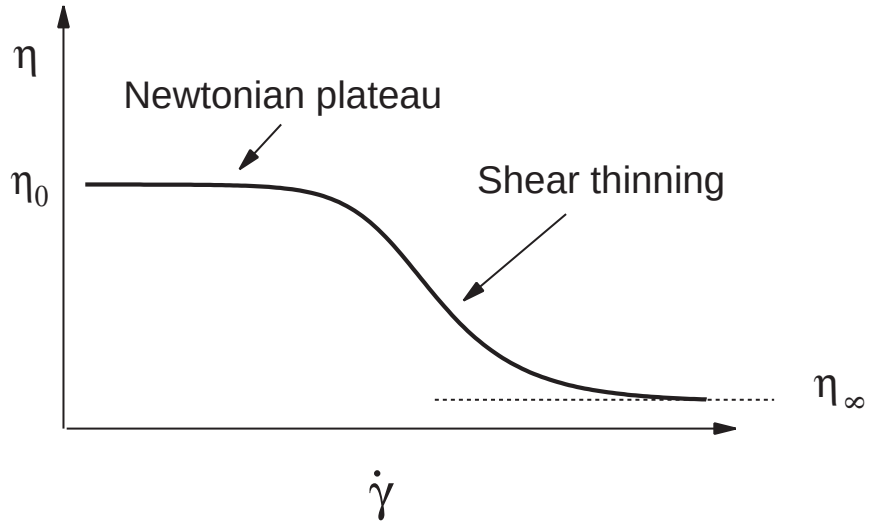

Figure 1.1: Schematic plot of viscosity as a function of shear rate for a polymer solution.

of strain rate $\dot{\gamma}$ for a typical polymer solution. The viscosity falls from the zero-shear value η_0 at low $\dot{\gamma}$ to a lower value η_∞ in the limit of infinite shear rate. Depending on the material, the difference between η_0 and η_∞ can be several orders of magnitude. The decrease of η is due to disentanglement and alignment of the polymer molecules under shear. The inverse of the shear rate at which the viscosity starts to decrease is determined by the time needed for the entangled polymers to relax.

The viscoelastic properties of polymeric materials are dependent on temperature and time. Fig. 1.2 shows an idealized plot of the relaxation modulus G as a function of temperature for a typical linear polymer. Four regions of viscoelastic behavior can be identified. At low temperatures, the polymer is hard and brittle, and the modulus is large. This is the glassy region, in which polymer segments are "frozen" and simply vibrate around fixed positions. In this state, the thermal energy is insufficient to overcome the potential barriers between different configurations of the polymer chain and so the segments can not move. As the temperature increases, the thermal energy becomes roughly comparable to the potential barriers. This is the glass transition temperature. Above this temperature, short-range

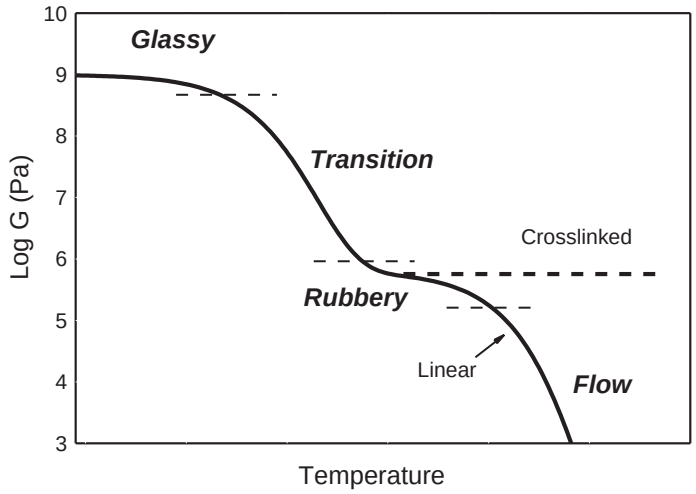

Figure 1.2: Schematic plot of the stress relaxation modulus of a polymer material as a function of temperature.

diffusion of the polymer segments becomes possible, and segments are free to "jump" from one configuration to another. At even higher temperatures, the modulus reaches a second plateau. This rubbery plateau is due to the presence of strong local interactions between neighboring chains, which restrict the long-range cooperative diffusion of complete molecules. In a linear polymer, these interactions are known as entanglements. In the case of a cross-linked material, they consist of chemical or physical bonds. In a linear polymer, as the temperature is further increased, the entanglements relax and the molecules become able to flow so the modulus again decreases [6]. In a chemically cross-linked system, however, the crosslinks will remain intact, and the modulus remains constant until the temperature is high enough for chemical degradation.

Some polymers may undergo a transition from a liquid-like material to a solid-like material under some conditions, such as when the temperature decreases from high to low. This is referred to as a sol-gel transition or gelation. It is different from the glass transition discussed above, which is the transition between a hard and relatively brittle state and a molten or rubber-like state. In the gelation process, polymers initially in the fluid or sol state become

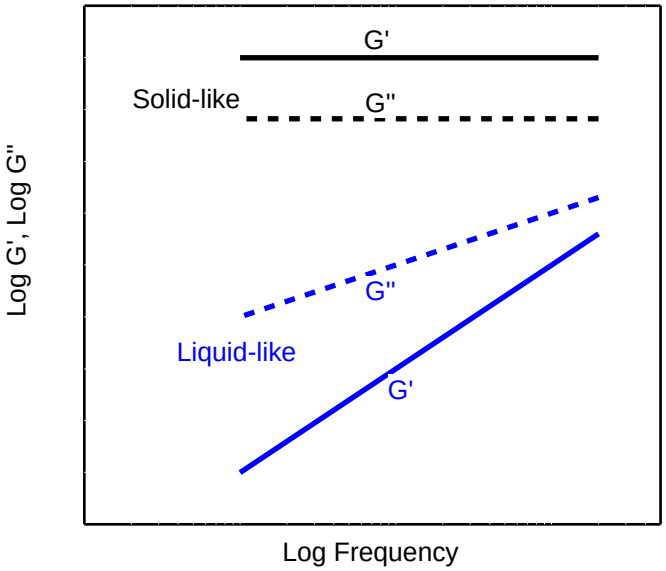

Figure 1.3: Schematic plot of the shear modulus of materials as a function of frequency.

connected to form a gel network. The storage modulus G' and loss modulus G'' of liquid-like and solid-like materials behave very differently as a function of frequency ω, as shown in Fig. 1.3, and therefore they can be used to characterize the gelation of a system. For liquid-like materials, G'' is much higher than G' and, at frequencies smaller than the shortest relaxation rate in the system, and one expects $G'' \propto \omega$ and $G' \propto \omega^2$ [1]. For solid-like materials, in contrast, G' is much higher than G'' and both G' and G'' are nearly frequency-independent, due to the existence of structures that can not relax over the time scales being probed [1]. At the gel transition, G' and G'' both show a power-law dependence on frequency, with $G' \sim G'' \propto \omega^{\nu}$, where ν is a power-law index [5]. This will be discussed in more detail in Chapter 2.

1.4 Microrheology

Soft materials such as polymer solutions and gels are typically structured on the microscopic scale. The techniques of microrheology have been developed to probe viscoelastic properties on such scales [3, 7]. This relatively new set of techniques can be used to investigate how the viscoelasticity of materials changes with length scale. From this, information about the materials' microstructure can be obtained.

Microrheology involves using micron-sized tracer particles suspended in the material to locally measure the rheology of complex materials. This typically involves extracting the local viscous and elastic moduli from measurements of the motion of the tracers. There are two main classes of microrheological methods, distinguished by how the particle motion is driven. One class involves the active manipulation of probes by external fields and is called active microrheology. The other involves measuring the motion of the particles due to thermal fluctuations and is referred to as passive microrheology. In either case, the interpretation of the measurements depends on the size of the probe particle relative to the structural length scales in the material. If the embedded particles are larger than any structural scale, the particle motion measures the macroscopic properties of the material. If they are smaller than the structural size, local rheological properties can be measured.

1.4.1 Active Microrheology

Magnetic tweezers can be used to manipulate magnetic particles suspended in a material for active microrheology [8]. The motion of these particles is measured and related to the local rheology of the material. This method has been used to measure the microrheology of a number of interesting materials, such as networks of filamentous actin [9, 10], living cells [11] and double-helical structured DNA [12].

Another example of active microrheology involves optical tweezers, in which a highly fo-

cused beam of light captures and manipulates small dielectric particles. The two main optical forces exerted on an illuminated particle are the scattering forces, which act along the direction of beam propagation, and the gradient force, which arises from induced dipole interactions with the electric field gradient. The resultant force tends to pull the particle towards the focus. Moving the focused laser beam forces the particle to move, applying a local stress to the surrounding material and allowing the local rheological response to be probed [13]. Probe particles can be driven in either oscillatory or translational motion so both frequency-dependent and steady state properties can be measured [14]. The forces applied by optical tweezers are very local and typically limited to the pN range. Optical tweezers have been used to measure the microrheology of complex materials such as membranes with cytoskeletal proteins [15], solutions of DNA [16] and colloidal suspensions [17, 18].

A third active microrheological technique involves using an atomic force microscope (AFM). In addition to imaging surface structure and topology, AFM techniques are sensitive to the force required to deform a surface and have been used to measure the local elasticity and viscoelasticity of soft materials. An AFM measures forces by monitoring the deflection of a tip connected to a cantilever spring brought into contact with the surface. The force exerted by the cantilever can be calculated using Hooke's law. Mahaffy et al. probed surfaces using an AFM cantilever with a polystyrene bead glued underneath of the tip. By oscillating the cantilever when approaching the surface of a polyacrylamide gel, they successfully measured the viscoelastic response of the sample surface [19]. AFM techniques have been used to study soft materials such as gels [19], blood platelets [20] and cells [21, 22].

1.4.2 Passive Microrheology

Passive microrheology measures the rheological properties of a material by monitoring the thermally-driven motion of a large number of tracer particles suspended within it. Since the particles are driven by thermal energy only, this technique is only suitable for very soft materials in which the linear motion is large enough to be accurately measured. A common

method is to image the positions of fluorescent probe particles using video microscopy. The ensemble-averaged mean squared displacement (MSD) of the particles can be used to calculate the frequency-dependent viscous and elastic moduli of the materials using a generalized Stokes-Einstein relation [23, 24], as will be discussed in detail in the next chapter. Depending on the size of the probe particles relative to the structure in the fluid, the viscoelastic properties determined in this way are a measure of either the local or the bulk properties of the material, as mentioned above. In two-particle microrheology, the cross-correlation function of the particle displacements is calculated as a function of particle separation [25, 26]. This can be used to infer information about the material structure and properties on different length scales. This provides a way to probe the bulk rheology of a heterogeneous sample using microrheology. The drawback of this technique is that a large amount of data is needed to obtain statistically meaningful results. Although particle tracking microrheology is restricted to relatively low frequencies, it is a fairly simple technique to implement. It has been applied to various materials, such as solutions of DNA [27], actin filaments [28, 29], Carbopol gels [30, 31], cross-linked polyacrylamide networks [32], laponite clay suspensions [33] and polymer microgels [36].

Dynamic light scattering can also be used for microrheological measurements. An incoming laser beam illuminates a sample in which probe particles are suspended, and is scattered by the probe particles into a detector at a scattering angle θ. As the particles diffuse in the sample, the intensity of scattered light that reaches the detector fluctuates in time. The autocorrelation function of the time-dependent intensity is calculated. With the assumption that the scattering is a Gaussian process and that the photons are scattered only once by the particles, the field correlation function can be calculated from the intensity correlation function [35], allowing the ensemble-averaged mean squared displacement of the particles to be determined as a function of time. As above, the mean squared displacement can be used to calculate the micron-scale rheological properties of the material [30, 36].

If the density of scatterers is very high, so that the photons scatter many times on the way to the detector, diffusing wave spectroscopy can be used to measure the ensemble-averaged

mean squared displacement of the probe particles [35, 37]. Although the experimental set-up is similar to that of the single-scattering experiment, all angle-dependent information is lost as the photons are scattered through all possible angles. Diffusing wave spectroscopy can be used for rheological measurements at frequencies up to 10^5 Hz. The microrheology of flexible and semi-flexible polymer solutions has been studied using this technique [28, 38, 39].

1.5 Summary of Present Work

1.5.1 Overview

In this thesis, we study the structure and viscoelastic properties of poly(vinyl alcohol) (PVA) solutions and physically-crosslinked gels using different techniques, including atomic force microscopy, bulk rheological measurements, dynamic light scattering and passive microrheology. PVA is a linear polymer which has a large number of hydroxyl groups. It is water-soluble and biocompatible. The PVA gels studied in this research are physically crosslinked, either by freeze/thaw thermal cycling, or by adding a gelling agent, poly(ethylene glycol) (PEG). These physical gels have numerous biomedical and pharmaceutical application, such as contact lenses, drug delivery and artificial tissues, due to their non-toxicity and nonlinear mechanical properties [56, 57, 58, 59, 60]. The theoretical background behind the experimental methods and data analysis is provided in Chapter 2. Details of the experimental techniques are presented in Chapter 3. Our results are presented and discussed in Chapters 4–6. We developed a technique for studying the surface viscoelastic properties of soft materials using atomic force microscopy, and applied it to PVA nanofibers and hydrogels. This work is described in Chapter 4. We then studied the rheology and structure of PVA gels during aging, using bulk rheology, dynamic light scattering, and passive microrheology, as described in Chapters 5 and 6. The main theme of the research is to investigate the structure and viscoelastic properties of PVA physical gels, and relate their local structure and properties to their bulk rheological properties. A summary and conclusion as well as

suggestions for future work are given in Chapter 7.

1.5.2 Frequency-Dependent Viscoelasticity Measurements by Atomic Force Microscopy

The atomic force microscope (AFM) has been widely used to study the structure of soft and biological materials with sub-nanometer resolution. AFM is also used to measure the local elasticity and viscoelasticity of soft samples. The advantage of AFM measurements is that topographic images can be obtained simultaneously with the mechanical response, allowing elasticity to be correlated with local structure. One common technique, referred to as force volume imaging, involves indenting the sample by translating it through a vertical ramp at positions over a grid of sample positions [53]. The discrepancy between the known vertical displacement and resulting cantilever deflection can be used to infer the elastic properties of the sample. The effects of non-vertical motion due to sliding of the inclined cantilever along the sample surface (e.g., shear deformation and frictional effects) as well as surface adhesion can complicate the analysis, however. In addition, force-volume imaging does not provide information about the viscous response. AFM measurements using intermittent contact mode or force modulation mode, both of which image surfaces with a cantilever oscillating at a small amplitude with a fixed frequency, can reveal contrast in the viscoelastic properties of the sample, but their nonlinear behavior complicates the analysis [54, 55].

In the work presented in Chapter 4, we describe a new AFM technique for investigating frequency-dependent viscoelastic properties, which we demonstrate on PVA nanofibers and hydrogels. A small oscillatory voltage was added to the feedback electronic circuit of the AFM during contact mode operation and the resultant motion of the sample was measured during imaging. The frequency-dependent viscoelastic modulus can be determined by analyzing the amplitude and phase of this motion relative to the external oscillation. The validity of this method was verified by comparing the results with those from traditional static methods.

1.5.3 Viscoelastic Properties and Structural Evolution of Physically Cross-Linked Poly(vinyl alcohol)/Poly(ethylene glycol) Blends during Aging

As PVA molecules have a large number of hydroxyl groups, they aggregate easily in concentrated solutions due to hydrogen bonding. The polymer aggregates form a network structure leading to gelation [56, 60, 61]. PVA has an upper critical solution temperature, and phase separates when quenched into the unstable region of the phase diagram. Consequently, gelation can take place in combination with microphase separation [62, 63, 64, 65]. Because of this, the mechanism of gelation in physical PVA gels is still not well understood. We are also interested in studying the dependence of the gel transition on length scale. Although Matsunaga et al. found good agreement between the microscopic and macroscopic gel points of gelatin hydrogels [66], Oppong et al. observed that gelation of Laponite clay suspensions occurred earlier on the macroscopic scale than on the microscopic scale [33]. By studying gelation in PVA blends, we will explore this phenomenon.

We study the aging of physical PVA gels made by the theta-gel method [67, 68], in which PEG is added to the PVA solution as a gelling agent. The blends undergo gelation over a period of up to two months. We measure the rheological behavior using conventional rheometry. We also use dynamic light scattering to investigate the microstructural evolution as a function of PEG concentration and aging time, and determine the microscopic gel points of the PVA gels. We compare the gelation thresholds measured by the two techniques. This work will be presented in Chapter 5.

1.5.4 Microrheology, Microstructure, and Aging of Physically Cross-Linked Poly(vinyl alcohol)/Poly(ethylene glycol) Blends

In Chapter 6, we use microrheological techniques to study the gelation and phase separation of the physically crosslinked PVA/PEG blends. We perform particle-tracking and dynamic light scattering experiments to investigate the microrheology and microstructure of these

materials as a function of PEG concentration and aging time.

Dynamic light scattering from small probe particles suspended in the materials allows us to study the particle motion over a range of time scales and provides information about the microscopic viscosity and elasticity. We also use video–based particle tracking to investigate the microscopic heterogeneity of the system. We study the changes in structure and viscoelastic properties that take place as the material ages and gels. We compare the microrheological results with the bulk rheology.

BIBLIOGRAPHY

[1] R. G. Larson, *The Structure and Rheology of Complex Fluids* (Oxford University Press, New York, 1999).

[2] P. G. de Gennes, Rev. Mod. Phys. **64**, 645 (1992).

[3] T. M. Squires and T. G. Mason, Annu. Rev. Fluid Mech. **42**, 413(2010).

[4] F. A. Morrison, *Understanding Rheology* (Oxford University Press, New York, 2001).

[5] M. Rubinstein and R. H. Colby, *Polymer Physics* (Oxford University Press, New York, 2003).

[6] M. T. Shaw and W. J. MacKnight, *Introduction to Polymer Viscoelasticity* (Wiley, New Jersey, 2005).

[7] T. A. Waigh, Rep. Prog. Phys. **68**, 685 (2005).

[8] B. Chu and J. Wang, Rev. Sci. Instrum. **63**, 2315 (1992).

[9] F. Ziemann, J. Radler, and E. Sackmann, Biophys. J. **66**, 2210 (1994).

[10] F. Amblard, A. C. Maggs, B. Yurke, A. N. Pargellis, and S. Leibler, Phys. Rev. Lett. **77**, 4470 (1996).

[11] B. Fabry, G. N. Maksym, J. P. Butler, M. Glogauer, D. Navajas, and J. J. Fredberg, Phys. Rev. Lett. **87**, 1481021 (2001).

[12] T. R. Strick, M. N. Dessinges, G. Charvin, N. H. Dekker, J. F. Allemand, D. Bensimon, and V. Croquette, Rep. Prog. Phys. **66**, 1 (2003).

[13] A. Ashkin, Biophys. J. **61**, 569 (1992).

[14] L. A. Hough and H. D. Ou–Yang, J. Nanopart. Res. **1**, 495 (1999).

[15] E. Helfer, S. Harlepp, L. Bourdieu, J. Robert, F. C. MacKintosh, and D. Chatenay, Phys. Rev. E **63**, 021904 (2001).

[16] T. T. Perkins, D. E. Smith, R. G. Larson, and S. S. Chu, Science **268**, 83 (1995).

[17] P. Habdas, D. Schaar, C. A. Levitt, and E. R. Weeks, Europhys. Lett. **67**, 477 (2004).

[18] A. Meyer, A. Marshall, B. G. Bush, and E. M. Furst, J. Rheol. **50**, 77 (2006).

[19] R. E. Mahaffy, C. K. Shih, F. C. MacKintosh, and J. Kas, Phys. Rev. Lett. **85**, 880 (2000).

[20] M. Radmacher, M. Fritz, C. M. Kasher, Biophys. J. **70**, 556 (1996).

[21] C. Rotsch, F. Braet, E. Wisse, and M. Radmacher, Cell Biol. Int. **21**, 685 (1997).

[22] C. Rotsch and M. Radmacher, Biophys. J. **78**, 520 (2000).

[23] T. G. Mason and D. A. Weitz, Phys. Rev. Lett. **74**, 1250 (1995).

[24] T. G. Mason, Rheol. Acta **39**, 371 (2000).

[25] T. C. Lubensky and A. J. Levine, Phys. Rev. Lett. **85**, 1774 (2000).

[26] J. C. Crocker, M. T. Valentine, E. R. Weeks, T. Gisler, P. D. Kaplan, A. G. Yodh, and D. A. Weitz, Phys. Rev. Lett. **85**, 888 (2000).

[27] T. G. Mason, A. Dhople, and D. Wirtz. Mater. Res. Soc. Symp. Proc. **463**, 153 (1997).

[28] J. Y. Xu, V. Viasnoff, and D. Wirtz, Rheol. Acta **37**, 387 (1998).

[29] J. Apgar, Y. Tseng, E. Fedorov, M. B. Herwig, S. C. Almo, and D. Wirtz, Biophys. J. **79**, 1095 (2000).

[30] F. K. Oppong, L. Rubatat, B. J. Frisken, A. E. Bailey, and J. R. de Bruyn, Phys. Rev. E **73**, 041405 (2006).

[31] F. K. Oppong and J. R. de Bruyn, J. Non–Newtonian Fluid Mech. **142**, 104 (2007).

[32] B. R. Dasgupta and D. A. Weitz, Phys. Rev. E **71**, 021504 (2005).

[33] F. K. Oppong, P. Coussot, and J. R. de Bruyn, Phys. Rev. E **78**, 021405 (2008).

[34] D. van den Ende, E. H. Purnomo, M. H. G. Duits, W. Richtering, and F. Mugele, Phys. Rev. E **81**, 011404 (2010).

[35] W. Brown, *Dynamic Light Scattering: The Method and Some Applications* (Oxford Univ. Press, New York, 1993).

[36] T. G. Mason, H. Gang, and D. A. Weitz, J. Molec. Struct. **383**, 81 (1996).

[37] T. G. Mason, H. Gang, and D. A. Weitz, J. Opt. Soc. Am. A **14**, 139 (1997).

[38] B. R. Dasgupta, S.-Y. Tee, J. C. Crocker, B. J. Frisken, and D. A. Weitz, Phys. Rev. E **65**, 051505 (2002).

[39] A. Palmer, T. G. Mason, J. Xu, S. C. Kuo, and D. Wirtz, Biophys. J. **76**, 1063 (1999).

[40] S. W. Lovesey and E. W. J. Mitchell, *Polymer and Neutron Scattering* (Oxford University Press, New York, 1994).

[41] M. Shibayama, Polym. J. **43**, 18 (2011).

[42] S. D. Hudson, J. L. Hutter, M.-P. Nieh, J. Pencer, L. E. Millon, and W. Wan, J. Chem. Phys. **130**, 034903 (2009).

[43] O. Urakawa, H. Ikuta, S. Nobukawa, T. Shikata, J. Polym. Sci. B: Polym. Phys. **46**, 2556 (2008).

[44] R. Mehta and M. D. Dadmun, Macromolecules **39**, 8799 (2006).

[45] M. Shibayama, S. Miyazaki, H. Endo, T. Karino, and K. Haraguchi, Macromol. Symp. **256**, 131 (2007).

[46] T. Nishida, H. Endo, N. Osaka, H. J. Li, K. Haraguchi, and M. Shibayama, Phys. Rev. E **80**, 030801 (2009).

[47] T. Matsunaga, T. Sakai, Y. Akagi, U. Chung, and M. Shibayama, Macromolecules **42**, 1344 (2009).

[48] H. Endo, D. Schwahn, and J. Colfen, J. Chem. Phys. **120**, 9410 (2004).

[49] M. V. Avdeev and V. L. Aksenov, Physics-Uspekhi **53**, 971 (2010).

[50] W.T. Heller, Acta. Cryst. **66**, 1213 (2010).

[51] M. Takeda, T. Matsunaga, T. Nishida, H. Endo, T. Takahashi, and M. Shibayama, Macromolecules **43**, 7793 (2010).

[52] T. Matsunaga, H. Endo, M. Takeda, M. Shibayama, Macromolecules **43**, 5075 (2010).

[53] G. Guhados, W. K. Wan, and J. L. Hutter, Langmuir **21**, 6642 (2005).

[54] L. Nony, R. Boisgard, and J. P. Aime, J. Chem. Phys. **111**, 1615 (1999).

[55] S. L. Lee, S. W. Howell, A. Raman, and R. Reifenberger, Phys. Rev. B **66**, 115409 (2002).

[56] C. M. Hassan, and N. A. Peppas, Adv. Polym. Sci. **153**, 37 (2000).

[57] M. Qi, Y. Gu, N. Sakata, D. Kim, Y. Shirouzu, Ch. Yamamoto, A. Hiura, S. Sumi, and K. Inoue, Biomaterials **25**, 5885 (2004).

[58] M. Kobayashi, Y.-S. Chang, and M. Oka, Biomaterials **26**, 3243 (2005).

[59] H. Bodugoz-Senturk, C. E. Macias, J. H. Kung, and O. K. Muratoglu, Biomaterials **30**, 589 (2009).

[60] S. D. Hudson, J. L. Hutter, M.-P. Nieh, J. Pencer, L. E. Millon, and W. Wan, J. Chem. Phys. **130**, 034903 (2009).

[61] T. Narita, A. Knaebel, J. P. Munch, and S. J. Candau, Macromolecules **34**, 8224 (2001).

[62] T. Kanaya, M. Ohkura, H. Takeshita, K. Kaji, M. Furusaka, H. Yamaoka, and G. D. Wignall, Macromolecules **28**, 3168 (1995).

[63] H. Takeshita, T. Kanaya, K. Nishida, and K. Kaji, Macromolecules **32**, 7815 (1999).

[64] H. Takeshita, T. Kanaya, K. Nishida, and K. Kaji, Macromolecules **34**, 7894 (2001).

[65] N. Takahashi, T. Kanaya, K. Nishida, and K. Kaji, Macromolecules **40**, 8750 (2007).

[66] T. Matsunaga and M. Shibayama, Phys. Rev. E **76**, 030401(R) (2007).

[67] E. Oral, H. Bodugoz-Senturk, C. Macias, and O. K. Muratoglu, Nucl. Instrum. Meth. B **265**, 92 (2007).

[68] A. Dashevsky, A. R. Ahmed, J. Mota, M. Irfan, K. Kolter, and R. A. Bodmeier, Biomaterials **29**, 141 (2008).

Chapter 2

Theory

2.1 Introduction

In this Chapter, we review the basic theory behind the experimental techniques used in this thesis. The Chapter is divided into four Sections; a summary of each is given below.

We introduce the theory of the motion of suspended particles in simple and complex fluids in Section 2.2. We discuss Brownian motion and its characteristics, as well as Stokes' law and the Langevin equation. Stokes' law describes the frictional force exerted on spherical objects in a viscous fluid. The Langevin equation is the equation of motion for particles moving in a viscous fluid. We derive an expression for the mean squared displacement of the particles in terms of the diffusion coefficient from both the Langevin equation and the diffusion equation. Then we derive the Stokes-Einstein relation by combining Stokes' law and diffusion theory. We then introduce a generalized Langevin equation which includes a memory function as the equation of motion for particles moving in a viscoelastic fluid. The generalized Stokes-Einstein relation is used to derive expressions for the viscoelastic moduli of the fluid. The material presented in this section follows the work in Refs. [1, 2, 3, 4].

In Section 2.3, we introduce the theory describing the scattering of radiation by particles suspended in a fluid. We first use Maxwell's equations to derive an expression for the

scattered electromagnetic field far from the scattering centers. We then introduce several simplifying assumptions to describe light scattering by a dilute suspension of discrete spherical particles. We introduce the dynamic light scattering technique used to study the diffusion of the scattering particles, and define the intensity and electric field correlation functions. The discussion in this section is primarily based on Refs. [6, 7, 8, 9].

In Section 2.4, we discuss the basic theory of the rheological behavior of polymers. We introduce the concept of linear viscoelasticity for soft materials. We start from the Mawell model and derive the generalized linear viscoelastic model, which is used to calculate the viscous and elastic moduli characterizing the response to a sinusoidally varying deformation [12, 13, 14].

Finally, in Section 2.5, we introduce the theoretical models that describe the dynamics of polymer molecules in both the dilute and concentrated regimes. To model the dilute regime, we discuss the Rouse model, while for the concentrated limit, we review the reptation or tube model. We discuss these models in the context of their predictions for the stress relaxation modulus and the viscous and elastic moduli. We also introduce the concept of gelation and discuss the rheological behavior of fluids near a gel point. The discussion in this section is based on Refs. [12, 15, 16].

2.2 The Motion of Particles in Simple and Complex Fluids

2.2.1 Brownian Motion

Brownian motion is named after Robert Brown, who first observed it in 1827 when he examined pollen grains in water. It is the continuous, random movement of microparticles suspended in a fluid [17]. It is driven by thermal energy and is due to random collisions of the fluid molecules with the particles. In 1905, Albert Einstein provided a mathematical interpretation of this phenomenon and argued that it provided direct evidence for the atomic

nature of matter [18]. Einstein was able to determine the mean squared displacement (MSD) of a Brownian particle in terms of Avogadro's number. In 1926, Jean Perrin won the Nobel Prize for determining Avogadro's number using this method [19].

Formally, Brownian motion is a stochastic process and can be described by a random walk model. Typically, each step in the walk is of constant length but the direction of the walk from one point to the next is completely random. We let l be the step length of a particle undergoing a random walk. Let the origin be at $\mathbf{r}_0 = 0$. After N steps, the particle will be at the point $\mathbf{r}_N$. After N+1 steps, the position of the particle will be

$$\mathbf{r}_{N+1} = \mathbf{r}_N + l\mathbf{n}, \tag{2.1}$$

where $\mathbf{n}$ is the unit vector in the direction of the $(N+1)^{th}$ step, that is, the direction of the step taken by the particle located at the point $\mathbf{r}_N$.

Because the direction of each step is random, we have $\langle \mathbf{n} \rangle = 0$, where the angular brackets denote as average over an ensemble of particles. As a result, if we take the average of both sides of Eq. (2.1), we have

$$\langle \mathbf{r}_{N+1} \rangle = \langle \mathbf{r}_N \rangle. \tag{2.2}$$

Eq. (2.2) indicates that for all N

$$\langle \mathbf{r}_N \rangle = \langle \mathbf{r}_{N-1} \rangle = ... = 0, \tag{2.3}$$

that is,

$$\langle \mathbf{r}_N \rangle = 0 \tag{2.4}$$

for all N.

The average of the squared displacement of a particle undergoing a random walk, $\langle \mathbf{r}^2 \rangle$, is

not zero, however. Einstein was able to show that

$$\langle \mathbf{r}^2 \rangle = 2Dt, \tag{2.5}$$

for one dimensional motion [1, 4], where D is the diffusion coefficient. We will derive Eq. (2.5) through the Langevin equation in Section 2.2.3, and through the diffusion equation in Section 2.2.4.

The central limit theorem expresses the fact that any sum of many statistically independent random variables is normally distributed [1, 2, 4]. Hence such a random variable has a probability distribution function that can be described by the normal or Gaussian distribution. This represents the probability of occurrence of each value of the random variable x and is given by

$$f(x) = \frac{1}{\sigma\sqrt{2\pi}} e^{-(x-\mu)^2/2\sigma^2}, \tag{2.6}$$

where μ is the mean and σ is the standard deviation of the distribution.

The displacement of a particle performing Brownian motion is the result of many random forces and so, by virtue of the central limit theorem, can be described by the Gaussian distribution function.

2.2.2 Stokes' Law

Stokes' law was derived by George Gabriel Stokes in 1851 to describe the friction or drag force exerted on spherical objects moving in a viscous fluid at very low speed [3]. We can derive this law from the equations of fluid dynamics. Consider a stationary sphere with radius a in a viscous flow as shown in Fig. 2.1. The flow field $\mathbf{v}(\mathbf{r}, t)$ can be described by the Navier-Stokes equation

$$(\mathbf{v} \cdot \nabla)\mathbf{v} = -\frac{1}{\rho}\nabla p + \eta \nabla^2 \mathbf{v} + \mathbf{g}, \tag{2.7}$$

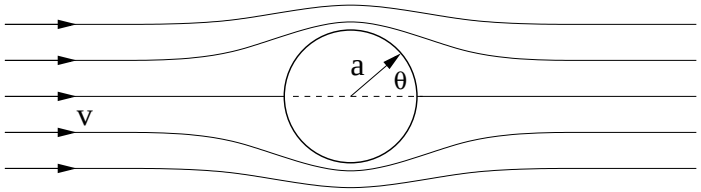

Figure 2.1: Schematic diagram showing a sphere in a viscous flow.

where ρ is the density and η the viscosity of the fluid, p is the pressure, and $\mathbf{g}$ is the acceleration due to gravity. We consider the case that the Reynolds number R, which is defined as

$$R = \frac{Va}{\eta}, \tag{2.8}$$

is very small, i.e., $R \ll 1$. Here, V is the flow speed far from the sphere. The Reynolds number is an indication of the relative magnitudes of the inertial term, $(\mathbf{v} \cdot \nabla)\mathbf{v}$, to the viscous term, $\eta\nabla^2\mathbf{v}$, in Eq. (2.7). For $R \ll 1$, the inertial term is much smaller than the viscous term and Eq. (2.7) simplifies to

$$0 = -\frac{1}{\nabla}p + \mu\nabla^2\mathbf{v}, \tag{2.9}$$

in the absence of body forces. We also have

$$\nabla \cdot \mathbf{v} = 0 \tag{2.10}$$

for an incompressible fluid. To solve Eq. (2.9), we work in spherical polar coordinates and introduce the scalar Stokes stream function $\Psi(r, \theta)$, such that

$$v_r = \frac{1}{r^2 \sin\theta}\frac{\partial\Psi}{\partial\theta}, \tag{2.11}$$

and

$$v_\theta = -\frac{1}{r \sin\theta}\frac{\partial\Psi}{\partial r}. \tag{2.12}$$

The boundary conditions on Ψ are $\frac{\partial \Psi}{\partial r} = \frac{1}{r}\frac{\partial \Psi}{\partial \theta} = 0$ on $r = a$, and $v_r = V\cos\theta$ and $v_\theta = V\sin\theta$ as $r \to \infty$. We try a solution of the form

$$\Psi = f(r)\sin^2\theta. \tag{2.13}$$

Upon substitution into Eqs. (2.9) and (2.10), we find

$$\left(\frac{d^2}{dr^2} - \frac{2}{r^2}\right)^2 f = 0. \tag{2.14}$$

This equation has a solution for f of the form r^α provided that

$$[(\alpha-2)(\alpha-3)-2][\alpha(\alpha-1)-2] = 0, \tag{2.15}$$

from which $\alpha = -1,\ 1,\ 2$ or 4. Thus

$$f(r) = \frac{A}{r} + Br + Cr^2 + Dr^4, \tag{2.16}$$

where A, B, C and D are arbitrary constants. Applying the boundary conditions, we have

$$\Psi = \frac{1}{4}V(2r^2 + \frac{a^3}{r} - 3ar)\sin^2\theta. \tag{2.17}$$

Having found Ψ, we can calculate the pressure using Eq. (2.9)

$$p = p_\infty - \frac{3}{2}\frac{\mu V a}{r^2}\cos\theta. \tag{2.18}$$

The radial and tangential stress components on the surface of the sphere are given by the constitutive equation for incompressible fluid [3] and we have

$$t_r = -p_\infty + \frac{3}{2}\frac{\mu V}{a}\cos\theta, \text{ and } t_\theta = -\frac{3}{2}\frac{\mu V}{a}\sin\theta. \tag{2.19}$$

By symmetry, we expect the net force on the sphere to be in the direction of the flow, and the appropriate component of the stress vector is thus $t = t_r \cos\theta - t_\theta \sin\theta$. The drag force on the sphere is the stress integrated over the surface of the sphere,

$$F_{drag} = \int_0^{2\pi} \int_0^{\pi} ta^2 \sin\theta d\theta d\phi = 6\pi\mu V a. \tag{2.20}$$

Eq. (2.20) is the Stokes relation. It says that a spherical particle moving in a viscous fluid experiences a drag force that is proportional to its speed relative to the fluid.

2.2.3 Langevin Equation and the Fluctuation-Dissipation Theorem

The Langevin equation is an equation of motion for particles moving in a fluid [2, 4]. It can be used in combination with the central limit theorem to quantitatively describe Brownian motion. In this section, we derive the Langevin equation for a Brownian particle moving in a simple fluid and introduce the fluctuation-dissipation theorem.

We consider a suspended microsphere undergoing Brownian motion in a liquid. Since its direction of motion changes, the sphere accelerates. The acceleration is due to the net force exerted on it. The forces on the microsphere include the downward force due to gravity, the upward buoyancy force, a random fluctuating force $\mathbf{F}(t)$, and the drag force f. Gravity is balanced by buoyancy as the sphere is suspended in the fluid. The random fluctuating force is the sum of the forces exerted on the sphere by all the molecules in the liquid that it is in contact with. The molecules move randomly and hence the net force they exert on the sphere is also random. As it moves through the liquid, the miscrosphere experiences a Stokes drag that is proportional to the velocity of the sphere, $f = -\alpha\mathbf{v}$, where $\mathbf{v}$ is the velocity of the particle with respect to the liquid and α is the drag force coefficient. For a particle performing Brownian motion, Newton's second law gives

$$m\frac{d\mathbf{v}(t)}{dt} = -\alpha\mathbf{v}(t) + \mathbf{F}(t), \tag{2.21}$$

where m is its mass and t is time. Consider two time scales in the Brownian motion problem. One is that over which correlations in the motion of the liquid molecules persist and the second is the time scale over which the suspended particle experiences a significant change in its velocity. Since the motion of the liquid molecules is much faster than that of the suspended particle, the second time scale is much longer than the first. If we consider two times t and t' separated by an interval long enough that the motion of the liquid molecules at the two times is uncorrelated, then the forces $\mathbf{F}(t)$ and $\mathbf{F}(t')$, will also be uncorrelated, so

$$\langle \mathbf{F}(t) \cdot \mathbf{F}(t') \rangle = \beta \delta(t - t'), \tag{2.22}$$

where β is a constant and δ is the Dirac delta function. Since $\mathbf{F}(t)$ is independent of the frictional drag $-\alpha \mathbf{v}$, we also have

$$\langle \mathbf{v}(0) \cdot \mathbf{F}(t) \rangle = 0 \tag{2.23}$$

for $t > 0$. Using these results, the general solution of Eq. (2.21) is given by

$$\mathbf{v}(t) = \mathbf{v}(0) \exp\left(-\frac{\alpha}{m} t\right) + \int_0^t dt' \frac{\mathbf{F}(t')}{m} \exp\left(-\frac{\alpha}{m}(t - t')\right). \tag{2.24}$$

Eqs. (2.21) – (2.24) constitute the Langevin model for the motion of a Brownian particle.

From the equipartition theorem, the mean square velocity of a particle in thermal equilibrium is

$$\langle v^2(t) \rangle = \frac{3kT}{m}, \tag{2.25}$$

where k is the Boltzmann constant and T is temperature. Using Eq. (2.24) and taking the ensemble average, we have

$$\begin{aligned} \langle v^2(t) \rangle &= \langle v^2(0) \rangle \exp(-2\frac{\alpha}{m} t) + \frac{2}{m} \int_0^t dt' \langle \mathbf{v}(0) \cdot \mathbf{F}(t) \rangle \exp(-2\frac{\alpha}{m}(t - t')) \\ &+ \int_0^t dt' \int_0^t dt'' \langle \frac{\mathbf{F}(t') \cdot \mathbf{F}(t'')}{m^2} \rangle \exp(-\frac{\alpha}{m}(2t - t' - t'')). \end{aligned} \tag{2.26}$$

All $\langle v^2 \rangle$ terms in Eq. (2.26) can be replaced by $3kT/m$, and the first integral on the right hand side vanishes according to Eq. (2.23). We use Eq. (2.22) to remove the delta function by performing one of the integrals of the third term on the right–hand side of Eq. (2.26). Eq. (2.26) then becomes

$$\frac{3kT}{m}\left(1-\exp(-2\frac{\alpha}{m}t)\right)=\frac{\beta}{m^2}\int_0^t dt' \exp\left(\exp(-2\frac{\alpha}{m}(t-t')\right). \tag{2.27}$$

After integration and simplification of Eq. (2.27), we get

$$\beta = 6\alpha kT, \tag{2.28}$$

so Eq. (2.22) becomes

$$\langle \mathbf{F}(t)\cdot\mathbf{F}(t')\rangle = 6\alpha kT\delta(t-t'). \tag{2.29}$$

Eq. (2.29) is referred to as the fluctuation-dissipation theorem [5]. This theorem relates the fluctuations in a system at thermal equilibrium to the response of the system. The random force $\mathbf{F}$ that causes the erratic motion of a particle has the same origin as the frictional force $-\alpha\mathbf{v}$ which causes the energy dissipation. The theorem shows that the mean-square value of a fluctuating force is related to the corresponding friction factor. If there was no fluctuating force $\mathbf{F}$ acting on the diffusing particles, then the velocity $\mathbf{v}$ and the kinetic energy of the particles would decrease exponentially and eventually vanish. The random force acts to restore the kinetic energy of the diffusing particles so that it remains constant on average [5].

2.2.4 Mean Squared Displacement from the Langevin Equation

In this section, we derive the motion of a Brownian particle moving in a simple fluid using the Langevin equation. In order to calculate the mean squared displacement $\langle \mathbf{r}^2 \rangle$, we rewrite

Eq. (2.21) in terms of the particle displacement $\mathbf{r}$, and multiply both sides by $\mathbf{r}$ to obtain

$$\frac{m}{2}\frac{d^2\mathbf{r}^2}{dt^2} - m\dot{\mathbf{r}}^2 + \frac{\alpha}{2}\frac{d\mathbf{r}^2(t)}{dt} = \mathbf{r}\cdot\mathbf{F}(t). \tag{2.30}$$

Averaging over a large number of the microspheres undergoing Brownian motion according to Eq. (2.30), we have

$$\frac{m}{2}\frac{d^2\langle\mathbf{r}^2\rangle}{d^2t} - m\langle\dot{\mathbf{r}}^2\rangle + \frac{\alpha}{2}\frac{d\langle\mathbf{r}^2\rangle}{dt} = \langle\mathbf{r}\cdot\mathbf{F}(t)\rangle. \tag{2.31}$$

Since $\mathbf{F}(t)$ is a random force, $\langle\mathbf{r}\cdot\mathbf{F}(t)\rangle = 0$. In addition, from the equipartition theorem, we have $m\langle\dot{\mathbf{r}}^2\rangle = kT$ in one dimension. Using these relations, Eq. (2.31) becomes

$$\frac{d^2\langle\mathbf{r}^2\rangle}{d^2t} + \frac{\alpha}{m}\frac{d\langle\mathbf{r}^2\rangle}{dt} = \frac{2kT}{m}. \tag{2.32}$$

The general solution of Eq. (2.32) is given by

$$\langle\mathbf{r}^2\rangle = \frac{2kT}{\alpha}t + C_1e^{-\frac{\alpha}{m}t} + C_2. \tag{2.33}$$

The second term in Eq. (2.33) is very small, since $\alpha/m \approx 10^7\ \mathrm{s}^{-1}$ for a typical colloidal particle in a viscous flow. If we let $\mathbf{r} = 0$ at time $t = 0$, we find the mean squared displacement of Brownian particles to be

$$\langle\mathbf{r}^2\rangle = \frac{2kT}{\alpha}t = 2Dt, \tag{2.34}$$

where $D = kT/\alpha$.

In practice, we observe the motion of the Brownian microspheres experimentally every τ seconds, so in time t, we make $N = \frac{t}{\tau} \gg 1$ measurements. If the displacements between two consecutive measurements are $\Delta\mathbf{r}_1$, $\Delta\mathbf{r}_2$,... $\Delta\mathbf{r}_N$, then the total displacement at time t is

$$\mathbf{r} = \Delta\mathbf{r}_1 + \Delta\mathbf{r}_2 + ... + \Delta\mathbf{r}_N, \tag{2.35}$$

so the mean–square displacement can be written as

$$\langle \mathbf{r}^2 \rangle = \sum_{i=1}^{N} \langle (\Delta \mathbf{r}_i)^2 \rangle + \sum_{j \neq i} \langle \Delta \mathbf{r}_j \Delta \mathbf{r}_i \rangle. \tag{2.36}$$

In Brownian motion, each displacement is independent so that $\sum_{j \neq i} \langle \Delta \mathbf{r}_j \Delta \mathbf{r}_i \rangle = 0$. Defining $\langle (\Delta \mathbf{r}_i)^2 \rangle$ as $\langle (\Delta \mathbf{r})^2 \rangle$ and noting that $\langle (\Delta \mathbf{r}_i)^2 \rangle$ is a constant for all i, we have

$$\langle \mathbf{r}^2 \rangle = \sum_{i=1}^{N} \langle (\Delta \mathbf{r}_i)^2 \rangle = \langle N (\Delta \mathbf{r})^2 \rangle. \tag{2.37}$$

Finally, Eq. (2.34) becomes

$$\langle (\Delta \mathbf{r})^2 \rangle = 2D\tau = \frac{2kT}{\alpha} \tau. \tag{2.38}$$

2.2.5 Mean Squared Displacement from the Diffusion Equation

Let $P(x,t)$ be the number density of the Brownian particles located at x at time t. Then the one–dimensional diffusion equation for $P(x,t)$ is [1, 4]

$$\frac{\partial P(x,t)}{\partial t} = D \frac{\partial^2 P(x,t)}{\partial x^2}. \tag{2.39}$$

In order to solve Eq. (2.39), we use the the Fourier transform of $P(x,t)$,

$$\widetilde{P}(k,t) = \int_{-\infty}^{\infty} P(x,t) e^{ikx} dx, \tag{2.40}$$

whose inverse transform is

$$P(x,t) = \frac{1}{2\pi} \int_{-\infty}^{\infty} \widetilde{P}(k,t) e^{-ikr} dk. \tag{2.41}$$

The derivatives of Eq. (2.41) that are needed in Eq. (2.39) are

$$\frac{\partial P(x,t)}{\partial t} = \frac{1}{2\pi}\int_{-\infty}^{\infty} \frac{\partial \widetilde{P}(k,t)}{\partial t} e^{-ikr} dk \tag{2.42}$$

and

$$\frac{\partial^2 P(x,t)}{\partial x^2} = \frac{-k^2}{2\pi}\int_{-\infty}^{\infty} \widetilde{P}(k,t) e^{-ikr} dk. \tag{2.43}$$

Substitution of Eq. (2.42) and Eq. (2.43) into Eq. (2.39) gives

$$\frac{\partial \widetilde{P}(k,t)}{\partial t} = -Dk^2 \widetilde{P}(k,t), \tag{2.44}$$

The solution of Eq. (2.44) is

$$\widetilde{P}(k,t) = Ae^{-Dk^2 t}, \tag{2.45}$$

where $A = \widetilde{P}(k,0)$. Performing the inverse transform, we have

$$P(x,t) = \frac{A}{2\pi}\int_{-\infty}^{\infty} \widetilde{P}(k,t) e^{-Dk^2 t - ikr} dk. \tag{2.46}$$

Using the integral

$$\int_{-\infty}^{\infty} e^{-ax^2+bx} dx = \sqrt{\frac{\pi}{a}} e^{b^2/4a}, \tag{2.47}$$

and as well as the normalization relation

$$\int_{-\infty}^{\infty} P(x,t) dt = 1, \tag{2.48}$$

we finally have

$$P(x,t) = \frac{1}{\sqrt{4\pi a t}} e^{-x^2/4Dt}. \tag{2.49}$$

This allows us to calculate the mean squared displacement as

$$\langle x^2 \rangle = \int_{-\infty}^{\infty} x^2 P(x,t) dt = \frac{1}{\sqrt{4\pi a t}}\int_{-\infty}^{\infty} x^2 e^{-x^2/4Dt} dx = 2Dt \tag{2.50}$$

Eq. (2.50) is the same as Eq. (2.34).

2.2.6 The Stokes–Einstein Equation

From Stokes' law, Eq. (2.20), the friction drag force coefficient α for a microsphere of radius a moving in a fluid of viscosity η, is

$$\alpha = 6\pi\eta a. \tag{2.51}$$

From Eq. (2.34), the diffusion coefficient D is therefore

$$D = \frac{kT}{6\pi\eta a}. \tag{2.52}$$

Eq. (2.52) is the famous Stokes–Einstein equation. It gives the self-diffusion coefficient of a spherical particle of radius a undergoing Brownian motion in a fluid with viscosity η and temperature T [1, 2, 4].

2.2.7 The Generalized Stokes-Einstein Equation and Microrheology

The Langevin equation discussed above describes the motion of particles in a purely viscous fluid. It therefore cannot be used to describe the motion of particles in complex fluids in which elastic effects are present. A generalized Langevin equation which incorporates a memory function has been proposed to account for viscoelasticity in complex fluids [13, 21, 22, 23]. In this case, the equation describing the forces acting on a neutrally buoyant particle in one dimension is

$$m\dot{v}(t) = -\int_0^t \xi(t-t')v(t')dt' + F(t), \tag{2.53}$$

where m and v are the particle mass and velocity, and $F(t)$ is the random fluctuation force exerted on the particle. $\xi(t)$ is a memory function which describes the local viscoelastic response of an isotropic, incompressible complex fluid. This integral accounts for the history dependence of the stress acting on the particle and allows energy stored in the fluid to be returned to the particle at a later time. The Gaussian random force F drives the particle motion and incorporates both instantaneous and stochastic energy which are stored and later

returned to the medium. As above, the random force is uncorrelated with past velocities, so

$$\langle v(0)F(t)\rangle = 0. \tag{2.54}$$

We also use the equipartition theorem to write

$$m\langle v^2(t)\rangle = kT. \tag{2.55}$$

Because $\xi(t)$ in Eq. (2.53) describes the stress history of the material, $\xi(t-t') = 0$ if $t' > t$ or $t' < 0$, and the limits on the integral of Eq. (2.53) can be changed from $(0, t)$ to $(-\infty, \infty)$. Using the property of the Fourier transform that

$$\mathcal{F}\left\{\frac{df(t)}{dt}\right\} = i\omega f^*(\omega) \tag{2.56}$$

and the convolution integral relation

$$\mathcal{F}\left\{\int_{-\infty}^{\infty} f(t-t')g(t')dt'\right\} = f^*(\omega)g^*(\omega), \tag{2.57}$$

where $f^*(\omega)$ and $g^*(\omega)$ are the Fourier transforms of $f(t)$ and $g(t)$, Eq. (2.53) yields

$$v^*(\omega) = \frac{F^*(\omega) + mv(0)}{\xi^*(\omega) + i\omega m}, \tag{2.58}$$

where the initial condition for the velocity has been used. To calculate the velocity autocorrelation function, we multiply Eq. (2.58) by $v(0)$ and take the ensemble average. Using Eq. (2.54) and Eq. (2.55), we obtain

$$\langle v(0)v^*(\omega)\rangle = \frac{kT}{\xi^*(\omega) + i\omega m}, \tag{2.59}$$

so the local memory function becomes

$$\xi^*(\omega) = \frac{kT}{\langle v(0)v^*(\omega)\rangle}, \tag{2.60}$$

where the inertial term $im\omega$ is ignored. Eq. (2.60) indicates that the frequency dependent memory function is simply inversely proportional to the velocity autocorrelation function.

In an isotropic medium, the velocity autocorrelation function can be obtained from the second time derivative of the mean squared displacement [25]:

$$\langle v(0)v(t)\rangle = \frac{1}{6}\left[\frac{\partial^2\langle \Delta\mathbf{r}^2(t)\rangle}{\partial t^2}\right]. \tag{2.61}$$

Transforming to the frequency domain and using the property of Fourier transform

$$\mathcal{F}\left\{\frac{d^2 f(t)}{dt^2}\right\} = (i\omega)^2 f^*(\omega), \tag{2.62}$$

we have

$$\xi^*(\omega) = \frac{6kT}{(i\omega)^2\mathcal{F}\{\langle \Delta\mathbf{r}^2(t)\rangle\}}. \tag{2.63}$$

In order to obtain the complex modulus of the viscoelastic fluid, from which the viscous and elastic moduli can be extracted, we generalize Stokes' law to the case of a complex fluid, assuming that the complex fluid can be treated as a continuum around the sphere. This is strictly valid when the length scales of the structures giving rise to the elasticity are much smaller than the sphere's radius a [23]. Generalizing Eq. (2.51), we assume that the Stokes relation for the drag of a purely viscous fluid can be used to determine the complex viscosity $\eta^*(\omega)$ over all frequencies:

$$\eta^*(\omega) = \frac{\xi^*(\omega)}{6\pi a}. \tag{2.64}$$

The complex shear modulus $G^*(\omega)$, which is equal to $i\omega\eta^*(\omega)$, is given by

$$G^*(\omega) = \frac{kT}{\pi a(i\omega)\mathcal{F}\{\langle \Delta\mathbf{r}^2(t)\rangle\}} \tag{2.65}$$

for $\omega > 0$. Eq. (2.65) is the generalized Stokes-Einstein equation in the frequency domain. If $\langle \Delta\mathbf{r}^2(t)\rangle$ is known and its complex Fourier transform can be computed accurately, the viscous and elastic moduli can be calculated from the imaginary and real parts of Eq. (2.65).

$\langle \Delta \mathbf{r}^2(t) \rangle$ can usually only be obtained over a limited temporal range at discrete times, and performing the Fourier transform on such data introduces errors at the frequency extremes due to truncation of the data. To overcome this limitation, an algebraic method for estimation of the transform has been suggested [23]. In this method, $\langle \Delta \mathbf{r}^2(t) \rangle$ is approximated locally about the frequency of interest ω by

$$\langle \Delta \mathbf{r}^2(t) \rangle \approx \langle \Delta \mathbf{r}^2(1/\omega) \rangle (\omega t)^{\alpha(\omega)}, \tag{2.66}$$

where $\langle \Delta \mathbf{r}^2(1/\omega) \rangle$ is the magnitude of $\langle \Delta \mathbf{r}^2(t) \rangle$ at $t = 1/\omega$ and

$$\alpha(\omega) \equiv \frac{d \ln \langle \Delta \mathbf{r}^2(t) \rangle}{d \ln t}|_{t=1/\omega} \tag{2.67}$$

is the power-law exponent describing the logarithmic slope of $\langle \Delta \mathbf{r}^2(t) \rangle$ at $t = 1/\omega$. Evaluation of the Fourier transform of $\langle \Delta \mathbf{r}^2(t) \rangle$ leads to the relation [23]:

$$(i\omega)\mathcal{F}\{\langle \Delta \mathbf{r}^2(t) \rangle\} \approx \langle \Delta \mathbf{r}^2(1/\omega) \rangle \Gamma[1 + \alpha(\omega)] i^{-\alpha(\omega)} \tag{2.68}$$

where Γ is the gamma function. Substituting Eq. (2.68) into Eq. (2.65) and using Euler's equation results in

$$|G'(\omega)| = |G^*(\omega)| \cos(\pi \alpha(\omega)/2) \tag{2.69}$$

and

$$|G''(\omega)| = |G^*(\omega)| \sin(\pi \alpha(\omega)/2), \tag{2.70}$$

where

$$|G^*(\omega)| = \frac{kT}{\pi a \langle \Delta \mathbf{r}^2(1/\omega) \rangle \Gamma[1 + \alpha(\omega)]}. \tag{2.71}$$

Eqs. (2.69) to (2.71) provide a useful physical interpretation of the moduli in terms of $\langle \Delta \mathbf{r}^2(t) \rangle$. When the spheres move diffusively, α approaches unity and G'' dominates, whereas when the spheres are confined by the elasticity of a complex fluid, α approaches zero and G' dominates. Recently, a modified algebraic form of the generalized Stokes-Einstein equations

using second order logarithmic derivative corrections has been introduced [27, 26, 28]:

$$|G^*(\omega)| = \frac{kT}{\pi a \langle \Delta \mathbf{r}^2(1/\omega) \rangle \Gamma[1+\alpha(\omega)][1+\beta(\omega)/2]}, \tag{2.72}$$

where

$$\alpha(\omega) \equiv \frac{d \ln \langle \Delta \mathbf{r}^2(t) \rangle}{d \ln t}|_{t=1/\omega} \tag{2.73}$$

and

$$\beta(\omega) \equiv \frac{d^2 \ln \langle \Delta \mathbf{r}^2(t) \rangle}{d(\ln t)^2}|_{t=1/\omega} \tag{2.74}$$

are the first- and second-order logarithmic derivatives of $\langle \Delta \mathbf{r}^2(t) \rangle$, both evaluated at $t = 1/\omega$. The viscous modulus $G''(\omega)$ and elastic modulus $G'(\omega)$ are given by

$$G''(\omega) = |G^*(\omega)| \left\{1/\left[1+\beta'(\omega)\right]\right\} \sin\left[\frac{\pi\alpha'(\omega)}{2} - \beta'(\omega)\left[1-\alpha'(\omega)\right]\left(\frac{\pi}{2}-1\right)\right] \tag{2.75}$$

and

$$G'(\omega) = |G^*(\omega)| \left\{1/\left[1+\beta'(\omega)\right]\right\} \cos\left[\frac{\pi\alpha'(\omega)}{2} - \beta'(\omega)\alpha'(\omega)\left(\frac{\pi}{2}-1\right)\right], \tag{2.76}$$

respectively, where $\alpha'(\omega)$ and $\beta'(\omega)$ are the local first- and second-order logarithmic derivatives of $|G^*(\omega)|$. This method gives a better estimate of the moduli than Mason's original method [23] when the mean squared displacement is nonlinear with time.

2.3 Light Scattering Theory

The theory and experimental methods for the scattering of different types of radiation are similar [7]. Radiation is incident on a scattering medium, with some of it passing through the sample unaffected, and some being scattered. A detector at an angle θ relative to the incident beam measures the intensity $I(\theta, t)$ of the scattered radiation. In general, $I(\theta, t)$ fluctuates in time. On the other hand, different types of radiation interact with materials through different processes. For example, visible light is scattered by fluctuations in the dielectric

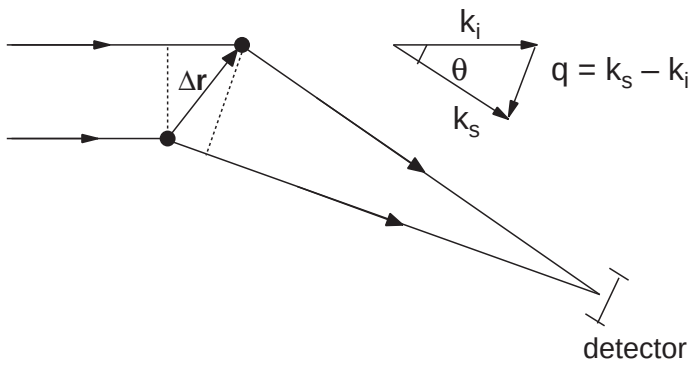

Figure 2.2: Schematic diagram showing scattering by two particles. The detector is far from the scattering particles. After [12].

constant of a material, while neutrons interact with atomic nuclei, and X-ray scattering is due to differences in electron density. The length scales probed also depend on the wavelength of the radiation. For light scattering, the length scale is up to several microns, while for neutron scattering or X-ray scattering it can be 100 nm at small scattering angles. In this section, we will introduce the theory of light scattering, which is one of the primary experimental techniques used in this thesis.

2.3.1 The Scattering Vector

Consider two nearby particles in a sample as shown in Fig 2.2. Coherent light from a laser is incident from the left onto the two particles. Light is scattered at an angle θ and collected by a detector. Note that the distance between the detector and the scattering particles is much larger than the distance between the two particles. The path lengths from the laser to the detector are different for light scattered from the two particles, and the light will therefore arrive at the detector with a difference in phase. It is convenient to define the scattering vector by $\mathbf{q} = \mathbf{k}_s - \mathbf{k}_i$, where $\mathbf{k}_i$ and $\mathbf{k}_s$ are the wave vectors of the incident light and scattered light, respectively. Therefore

$$q^2 = |\mathbf{k}_s - \mathbf{k}_i|^2 = k_s^2 + k_i^2 - 2\mathbf{k}_s \cdot \mathbf{k}_i. \tag{2.77}$$

In elastic light scattering, energy is conserved, so $|\mathbf{k}_i| = |\mathbf{k}_s|$ [6, 7, 12]. Using the law of cosines, $\mathbf{k}_s \cdot \mathbf{k}_i = k_s k_i \cos\theta = k_i^2 \cos\theta$, the magnitude of $\mathbf{q}$ is

$$q = 2k \sin\frac{\theta}{2} = \frac{4\pi}{\lambda} \sin\frac{\theta}{2}, \tag{2.78}$$

where $k = |\mathbf{k}_i| = |\mathbf{k}_s|$ and $\lambda = 2\pi/k$ is the wavelength of the incident light.

2.3.2 Scattering Electric Field

In this section, we will outline the derivation of an expression for the amplitude of the electric field of the scattered light at the detector in terms of scattering vector $\mathbf{q}$. More details can be found in Ref. [6].

We make several assumptions. First, we assume that the scattering process is "quasielastic" and the energy change is very small. We also assume that most photons pass through the sample unaffected, a few are scattered once, and multiple scattering is negligible. Finally, we assume that the incident beam is not distorted significantly by the medium. This is the first Born approximation, called the Rayleigh-Gans-Debye approximation in light scattering. It assumes that the phase of the wave traversing the scattering particle is the same as it would be if the particle were not present, and implies that

$$\frac{2\pi d}{\lambda} \left| \frac{n_p}{n_s} - 1 \right| \ll 1, \tag{2.79}$$

where n_p and n_s are the refractive indices of the particle and the solvent respectively, and d is the size of the particle [6]. Only polarized light is considered and the dielectric behavior of the medium is taken to be isotropic [7].

With these assumptions, Maxwell's equations for electromagnetic wave propagation [6] are

applied to incident plane-wave monochromatic light described by

$$\mathbf{E}(\mathbf{r},t) = E_0\mathbf{n}_i \exp[i(\mathbf{k}_i \cdot \mathbf{r} - \omega t)], \tag{2.80}$$

where E_0 is the magnitude of $\mathbf{E}(\mathbf{r},t)$, $\mathbf{n}_i$ is the polarization direction, $\mathbf{r}$ is the position vector, and ω is the angular frequency. Maxwell's equations are

$$\nabla \times \mathbf{E} = -\frac{1}{c}\frac{\partial \mathbf{B}}{\partial t}, \tag{2.81}$$

$$\nabla \times \mathbf{H} = -\frac{1}{c}\frac{\partial \mathbf{D}}{\partial t}, \tag{2.82}$$

$$\nabla \cdot \mathbf{B} = 0, \tag{2.83}$$

and

$$\nabla \cdot \mathbf{D} = 0, \tag{2.84}$$

where $\mathbf{E}$, $\mathbf{B}$ and $\mathbf{D}$ are the electric field, magnetic field and electric displacement field, respectively. $\mathbf{H}$ is the magnetizing field, and c is the speed of light in the medium.

Assuming a time dependence proportional to $e^{-i\omega t}$ for $\mathbf{D}$, Maxwell's equations can be simplified and solved. The solution is of the form

$$\mathbf{D} = \mathbf{D}_i + \mathbf{D}_s, \tag{2.85}$$

where $\mathbf{D}_i$ solves the homogenous equation which describes the unperturbed incoming wave and $\mathbf{D}_s$ is the scattered part. The total electric field is the sum of the incoming and scattered fields

$$\mathbf{E} = \mathbf{E}_0 + \mathbf{E}_s. \tag{2.86}$$

Since the scattered light is detected far from the scattering particle, we consider the far-field limit of E_s. After some calculation, the scattered light at the detector at position $\mathbf{R}$ is given

by

$$\mathbf{E}_s(\mathbf{r},t) = E_0 \frac{k^2 e^{i(kR-wt)}}{4\pi R} \int_V \frac{(\varepsilon(\mathbf{r},t)-\varepsilon_0)}{\varepsilon_0} e^{-i\mathbf{q}\cdot\mathbf{r}} d^3r, \tag{2.87}$$

where $\varepsilon(\mathbf{r})$ is the dielectric constant of the particles and ε_0 is the dielectric constant of surrounding medium [6].

Eq. (2.87) can be recognized as the integral of the radiation due to oscillating point dipoles over the whole sample volume [7]. The incident electric field induces a dipole moment of strength proportional to $E_0[\varepsilon(\mathbf{r},t)-\varepsilon_0]d^3r$ in the the volume element d^3r at a position $\mathbf{r}$. The dipole moment oscillates at angular frequency ω, scattering light in all directions. The exponential term $e^{-i\mathbf{q}\cdot\mathbf{r}}$ describes the radiation of the scattered light in a spherical wave with phase shift $-\mathbf{q}\cdot\mathbf{r}$ relative to the origin. If the medium is homogenous, $\varepsilon(\mathbf{r},t)=\varepsilon_0$, then there is no scattering. In other words, scattering of radiation at $\mathbf{q}\neq 0$ is caused by fluctuations in the dielectric properties of the medium.

2.3.3 Scattering by Discrete Scatterers

We now consider N scattering particles in the scattering volume V. The center of mass of the j^{th} particle is located at position $\mathbf{R}_j$ at time t. $\mathbf{r}_j$ is the position of the volume element d^3r_j relative to its center of mass. Using Eq. (2.87), the electric field scattered by the N particles becomes [7]

$$\mathbf{E}_s(\mathbf{r},t) = E_0 \frac{e^{i(kR-wt)}}{R} \sum_j^N \int_{V_j} \Delta\rho(\mathbf{r}_j,t) e^{-i\mathbf{q}\cdot\mathbf{r}_j} e^{-i\mathbf{q}\cdot\mathbf{R}_j} d^3r_j, \tag{2.88}$$

where V_j is the volume of particle j and $\Delta\rho(\mathbf{r}_j,t)$ is defined by

$$\Delta\rho(\mathbf{r}_j,t) = \frac{k^2}{4\pi} \frac{\varepsilon_P(\mathbf{r}_j,t)-\varepsilon_L}{\varepsilon_0}, \tag{2.89}$$

where $\varepsilon_P(\mathbf{r}_j, t)$ is the local dielectric constant at position $\mathbf{r}_j$ in the particle j, and ε_L is the average dielectric constant of the particle. Eq. (2.88) can be further simplified, giving

$$\mathbf{E}_s(\mathbf{r}, t) = E_0 \frac{e^{i(kR-wt)}}{R} \sum_j^N b_j(\mathbf{q}, t) e^{-i\mathbf{q}\cdot\mathbf{R}_j}, \tag{2.90}$$

where the scattering length $b_j(\mathbf{q}, t)$ is given by

$$b_j(\mathbf{q}, t) = \int_{V_j} \Delta\rho(\mathbf{r}_j, t) e^{-i\mathbf{q}\cdot\mathbf{r}_j} d^3 r_j. \tag{2.91}$$

From Eq. (2.90), we see that the scattered electric field is the sum of the field scattered by the individual particles. Each term is the product of a scattering length, determined by the instantaneous distribution of material within the particle, and a phase factor determined by the instantaneous position of the particle in the sample.

2.3.4 Scattering Intensity

Usually the scattered intensity is measured, rather than the electric field. Intensity and electric field are related by $I(\mathbf{q}, t) = |\mathbf{E}(\mathbf{q}, t)|^2$. Thus the scattered intensity can be expressed as

$$I(\mathbf{q}, t) = \frac{E_0^2}{R^2} \sum_j^N \sum_k^N b_j(\mathbf{q}, t) b_k^*(\mathbf{q}, t) e^{-i\mathbf{q}\cdot[\mathbf{R}_j - \mathbf{R}_k]}. \tag{2.92}$$

In static light scattering, the time average of the intensity is measured. This is equivalent to an ensemble average if the scattering medium is ergodic [7], and can be written as

$$\langle I(\mathbf{q}) \rangle = \left\langle \frac{E_0^2}{R^2} \sum_j^N \sum_k^N b_j(\mathbf{q}) b_k^*(\mathbf{q}) e^{-i\mathbf{q}\cdot[\mathbf{R}_j - \mathbf{R}_k]} \right\rangle. \tag{2.93}$$

Eq. (2.93) is the general result for the average intensity as a function of the modulus q of the scattering vector.

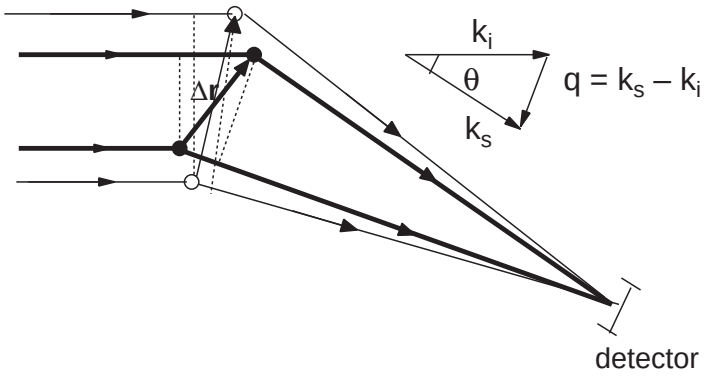

Figure 2.3: Schematic for dynamic light scattering from two particles. The filled and open circles indicate the positions of the two particles at times t and $t+\tau$ respectively. After [12].

2.3.5 Dynamic Light Scattering

Dynamic light scattering probes the temporal evolution of the concentration fluctuations that scatter light. As in the case of static light scattering, the relative phase of the light at the detector leads to constructive or destructive interference. As the particles move, the lengths of the paths followed by the scattered light change, as illustrated in Fig. 2.3, causing the relative phases at the detector to change. Thus, the intensity of the light at the detector fluctuates in time. The temporal evolution of the intensity fluctuations of the scattering light reflects the stochastic motion of the scatterers. For example, if we heat the sample so that the scatterers move more rapidly, the intensity of the scattered light will fluctuate more rapidly [7, 8]. The intensity autocorrelation function is defined as

$$\langle I(\mathbf{q},0)I(\mathbf{q},\tau)\rangle = lim_{t\to\infty}\frac{1}{t}\int_0^t dt' I(\mathbf{q},t')I(\mathbf{q},t'+\tau). \tag{2.94}$$

The autocorrelation function compares the intensity $I(\mathbf{q},t)$ at a time t to a delayed version $I(\mathbf{q},t+\tau)$ of itself, for all starting times t and a range of delay times τ. At zero delay time, Eq. (2.94) becomes

$$lim_{\tau\to 0}\left\langle I(\mathbf{q},0)I(\mathbf{q},\tau)\right\rangle = \left\langle I^2(\mathbf{q})\right\rangle. \tag{2.95}$$

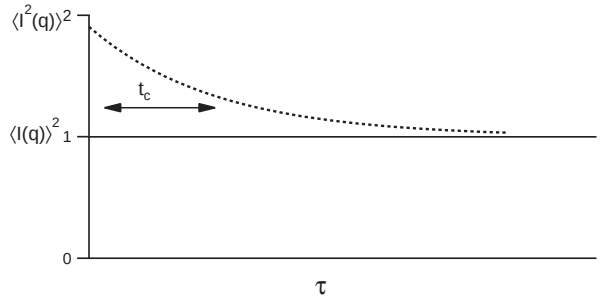

Figure 2.4: Schematic for typical behavior of the intensity autocorrelation function.

At the other limit, for τ much greater than the typical fluctuation time t_c of the intensity, the fluctuations in $I(\mathbf{q},t)$ and in $I(\mathbf{q},t+\tau)$ are uncorrelated so the the average in Eq. (2.94) can be separated, leading to

$$lim_{\tau\to\infty}\left\langle I(\mathbf{q},0)I(\mathbf{q},\tau)\right\rangle = \left\langle I(\mathbf{q},0)\right\rangle\left\langle I(\mathbf{q},\tau)\right\rangle = \left\langle I(\mathbf{q})\right\rangle^2. \tag{2.96}$$

The typical behavior of the intensity correlation function is sketched in Fig. 2.4. As is shown, the intensity correlation function decays from the mean squared intensity at small delay times to the square of the mean at long times.

To investigate the properties of the fluctuating scattered light we consider a simple situation of a dilute suspension of identical spherical particles. Eq. (2.90) gives the general expression for the instantaneous amplitude of the field $E(\mathbf{q},t)$ due to N particles at a point in the far field. Since we will be dealing with normalized quantities, we can omit the pre-factors in Eq. (2.90) and write

$$\mathbf{E}_s(\mathbf{r},t) = \sum_j^N e^{-i\mathbf{q}\cdot\mathbf{R}_j}. \tag{2.97}$$

Since the particles are randomly distributed in the sample, the phase angles in the factor $e^{-i\mathbf{q}\cdot\mathbf{R}_j}$ in Eq. (2.97) are randomly distributed between 0 and 2π. Therefore,

$$\left\langle \mathbf{E}_s(\mathbf{r},t)\right\rangle = 0. \tag{2.98}$$

The average of the scattered intensity is

$$\langle I(\mathbf{q},t)\rangle = \left\langle |\mathbf{E}(\mathbf{q},t)|^2 \right\rangle = \sum_{j=1}^{N}\sum_{k=1}^{N}\left\langle e^{-i\mathbf{q}\cdot(\mathbf{R}_j-\mathbf{R}_k)}\right\rangle = \sum_j 1 + \sum_{j\neq k}^{N}\sum^{N}\left\langle e^{-i\mathbf{q}\cdot\mathbf{R}_j}\right\rangle\left\langle e^{i\mathbf{q}\cdot\mathbf{R}_k}\right\rangle = N, \tag{2.99}$$

where, in averaging the cross-terms separately, we have exploited the assumption that the suspension is dilute so that the particle positions are uncorrelated. Eqs. (2.98) and (2.99) are well known results for random walk motion: the mean is zero since the walk is symmetrical about the origin on average, while the mean squared displacement is proportional to the number of steps, as discussed in Section 2.2. The normalized time autocorrelation function of the scattered field is defined by

$$g^{(1)}(q,\tau) = \frac{\langle E(\mathbf{q},0)E^*(\mathbf{q},\tau)\rangle}{\langle I(\mathbf{q})\rangle}. \tag{2.100}$$

Substitution of Eq. (2.97) into Eq. (2.100) gives

$$g^{(1)}(q,\tau) = N^{-1}\sum_j \left\langle e^{-i\mathbf{q}\cdot[\mathbf{R}_j(0)-\mathbf{R}_j(\tau)]}\right\rangle = \left\langle e^{-i\mathbf{q}\cdot[\mathbf{R}(0)-\mathbf{R}(\tau)]}\right\rangle, \tag{2.101}$$

the last step of which follows from the fact that the average motions of identical particles are themselves the same. Dynamic light scattering measures the time variation of the scattered intensity. The normalized correlation function of the scattered intensity is defined as [7, 8]

$$g^{(2)}(q,\tau) = \frac{\langle I(\mathbf{q},0)I(\mathbf{q},\tau)\rangle}{\langle I(\mathbf{q})\rangle^2}. \tag{2.102}$$

Using Eq. (2.97), we have

$$\begin{aligned}\langle I(\mathbf{q},0)I(\mathbf{q},\tau)\rangle &= \left\langle \sum_j\sum_k e^{-i\mathbf{q}\cdot[\mathbf{R}_j(0)-\mathbf{R}_k(0)]}\sum_l\sum_m e^{-i\mathbf{q}\cdot[\mathbf{R}_l(\tau)-\mathbf{R}_m(\tau)]}\right\rangle \\ &= \sum_j\sum_k\sum_l\sum_m \left\langle e^{-i\mathbf{q}\cdot[\mathbf{R}_j(0)-\mathbf{R}_k(0)+\mathbf{R}_l(\tau)-\mathbf{R}_m(\tau)]}\right\rangle. \end{aligned} \tag{2.103}$$

Eq. (2.103) can be simplified by exploiting the independence of particle position in dilute

suspensions. If one of the subscripts is different from all the others, the average of the exponential term with this subscript will cause Eq. (2.103) to be equal to zero because of Eq. (2.98). If all the subscripts are the same, the exponential term is equal to 1. There are N such cases. In the large N limit, these can be neglected since Eq. (2.103) is dominated by terms of order N^2, as we will see below. The only remaining contributions are those for which pairs of subscripts are equal. Terms with $j = l$ and $k = m$ are also zero since $\left\langle e^{-i\mathbf{q}\cdot[\mathbf{R}_j(0)+\mathbf{R}_j(\tau)]}\right\rangle = 0$. Thus the only non-zero contributions to Eq. (2.103) arise when $j = k$, $l = m$ or $j = m$, $k = l$, giving, for $N \to \infty$,

$$\begin{aligned}\langle I(\mathbf{q},0)I(\mathbf{q},\tau)\rangle &= \sum_j 1 \sum_l 1 + \sum_j \left\langle e^{-i\mathbf{q}\cdot[\mathbf{R}_j(0)-\mathbf{R}_j(\tau)]}\right\rangle \sum_k \left\langle e^{-i\mathbf{q}\cdot[\mathbf{R}_k(0)-\mathbf{R}_k(\tau)]}\right\rangle \\ &= N^2 + N^2 \left|\left\langle e^{-i\mathbf{q}\cdot[\mathbf{R}(0)-\mathbf{R}(\tau)]}\right\rangle\right|^2 . \qquad (2.104)\end{aligned}$$

Use of Eqs. (2.99) – (2.102) and Eq. (2.104) then gives

$$g^{(2)}(q,\tau) = 1 + [g_1(q,\tau)]^2. \qquad (2.105)$$

Eq. (2.105), which is sometimes called the Siegert relation, relates the intensity correlation function $g^{(2)}(q,\tau)$ to the electric field correlation function $g^{(1)}(q,\tau)$. By experimentally measuring $g^{(2)}(q,\tau)$ and using the Siegert relation, we can obtain $g^{(1)}(q,\tau)$, thus obtaining the desired information about the scattering system.

In reality, a detector has a non-zero active area and therefore sees different scattered fields (or intensities) at different points on its surface. To account for this, Eq. (2.105) is modified to

$$g^{(2)}(q,\tau) = 1 + \beta[g_1(q,\tau)]^2, \qquad (2.106)$$

where β is a factor which represents the degree of spatial coherence of the scattered light over the detector and is equal to the ratio of the detector area to the area of one speckle produced by the interference of the scattered light at the detector.

Mean Squared Displacement

If we define the change in phase due to the diffusion of a spherical particle as $\triangle\phi(\tau) = \mathbf{q}\cdot[\mathbf{R}(0)-\mathbf{R}(\tau)]$, Eq. (2.101) becomes

$$g^{(1)}(q,\tau) = \left\langle e^{-i\triangle\phi(\tau)}\right\rangle = e^{-\frac{1}{2}\left\langle\triangle\phi^2(\tau)\right\rangle}, \tag{2.107}$$

where we have assumed that since the motion of particles is random, $\triangle\phi(\tau)$ has Gaussian distribution [12]. Since $\triangle\phi(\tau) = \mathbf{q}\cdot[\mathbf{R}(0)-\mathbf{R}(\tau)] = \mathbf{q}\cdot\triangle\mathbf{R}$, we have

$$\left\langle\triangle\phi^2(\tau)\right\rangle = \frac{1}{3}\left\langle\triangle R^2(\tau)\right\rangle, \tag{2.108}$$

where the factor of $1/3$ comes from performing a three-dimensional angular average over the unit sphere. Therefore the field autocorrelation function $g_1(q,\tau)$ is

$$g^{(1)}(q,\tau) = e^{-\frac{1}{6}q^2\left\langle\triangle R^2(\tau)\right\rangle}. \tag{2.109}$$

For simple particle diffusion, $\langle\triangle R^2(\tau)\rangle = 6D\tau$ as shown in Section 2.2, so we have

$$g^{(1)}(q,\tau) = e^{-Dq^2\tau}. \tag{2.110}$$

Eqs. (2.109) and (2.110) show that we can extract the mean-squared displacement of spherical scatters from the field autocorrelation function [12].

Non-Ergodic Scattering

In an ergodic system, a representative subset of all of the possible system configurations is sampled in the dynamic light scattering measurement time. This means that a time-averaged measurement of a property gives a good estimate of its ensemble average. This is true in particular for the autocorrelation function. In some cases, however, such as gels or colloidal

glasses, the scatterers are able to execute only limited motion around fixed average positions and so do not sample all possible configurations [9]. In such cases, the system is nonergodic and a time average is not equivalent to an ensemble average. It has been shown that in such a case the intensity autocorrelation function has the form

$$g^{(2)}(\tau) = 1 + Y^2\{[g^{(1)}(\tau)]^2 - [g^{(1)}(\infty)]^2\} + 2Y(1-Y)\{g^{(1)}(\tau) - g^{(1)}(\infty)\}, \tag{2.111}$$

where $Y \equiv \langle I\rangle_E/\langle I\rangle_T$ is the ratio of the ensemble and time averages of the scattered intensity, and $g^{(1)}(\infty)$ is the value of field autocorrelation function at $\tau = \infty$ [10]. For ergodic systems, $Y = 1$, and Eq. (2.111) simplifies to the Siegert relation, Eq. (2.105). For non-ergodic systems, generally $Y < 1$. For the limiting case of a solid, the scattering particles do not move at all, $Y \approx 0 \ll 1$, and $g^{(2)}(\tau) \approx 1$ [9, 11].

2.4 Rheology Theory

Flows of complex fluids are time-dependent due to viscoelastic effects [13]. When polymeric fluids are sheared, the stress does not jump instantaneously when the flow starts, but rather takes some time to accumulate; on the other hand, when we stop shearing a polymer fluid, the stress does not instantaneously decrease to zero. Consequently polymer solutions behave like solids at short time scales or high frequencies and like liquids at long times or low frequencies, and elasticity or memory effects must be considered in describing their rheological behavior.

2.4.1 Maxwell Model

Newton's law of viscosity and Hooke's law for an elastic material were introduced in Section 1.2. We can write Hooke's law as

$$\sigma = \int d\sigma = -\int_{t_{ref}}^{t} G\frac{d\gamma}{dt'}dt', \tag{2.112}$$

by assuming that the stress due to a large deformation is the sum of contributions due to a series of small deformations, and that G only depends on time and not on the strain γ. Differentiating Eq. (2.112), we have

$$\frac{d\sigma}{dt} = -G\dot{\gamma}. \tag{2.113}$$

We can combine Eq. (1.1) and Eq. (2.113) for a complex fluid having both viscous and elastic characteristics as follows:

$$\sigma + \lambda\frac{\partial\sigma}{\partial t} = -\eta\dot{\gamma}. \tag{2.114}$$

This is the Maxwell model. Here λ has units of time and characterizes the relaxation of the material in response to an external deformation. In steady state, Eq. (2.114) becomes the Newtonian equation $\sigma = -\eta\dot{\gamma}$, while for rapidly varying stress it becomes Hooke's law with $G = \eta/\lambda$.

To solve Eq. (2.114), we multiply both sides by $(1/\lambda)e^{\frac{t}{\lambda}}$ and factor the left-hand side to obtain

$$\frac{d}{dt}(e^{\frac{t}{\lambda}}\sigma) = -\frac{\eta}{\lambda}e^{\frac{t}{\lambda}}\dot{\gamma}. \tag{2.115}$$

Integration over all past times up to the time of interest t yields

$$\begin{aligned} \int_{-\infty}^{t} d\left[e^{\frac{t'}{\lambda}}\sigma(t')\right] &= -\int_{-\infty}^{t}\frac{\eta}{\lambda}e^{\frac{t'}{\lambda}}\dot{\gamma}dt' \\ e^{\frac{t'}{\lambda}}\sigma(t')|_{-\infty}^{t} &= -\int_{-\infty}^{t}\frac{\eta}{\lambda}e^{\frac{t'}{\lambda}}\dot{\gamma}dt'. \end{aligned} \tag{2.116}$$

If we require that the stress be finite at $t = -\infty$, we can simplify the left–hand side to obtain

$$\begin{aligned} \sigma &= -e^{\frac{-t}{\lambda}}\int_{-\infty}^{t}\frac{\eta}{\lambda}e^{\frac{t'}{\lambda}}\dot{\gamma}dt' \\ &= -\int_{-\infty}^{t}\frac{\eta}{\lambda}e^{\frac{-(t-t')}{\lambda}}\dot{\gamma}dt' \end{aligned} \tag{2.117}$$

Eq. (2.117) is the integral form of the Maxwell model. The stress in this model depends on

the shear rate at all past times, weighted by an exponentially decaying "memory factor". The stress is therefore not only a function of the instantaneous shear rate, but also the shear rate history [13].

2.4.2 Generalized Maxwell Model

Most fluids are not characterized by a single relaxation time λ, but rather have multiple relaxation times. We can modify the Maxwell model to describe materials with more than one relaxation time if we assume additivity of the stresses – that is, we assume that the total stress is the sum of individual stresses, each of which has its own relaxation time. For each relaxation time λ_k and viscosity η_k, we have

$$\sigma_k + \lambda_k \frac{\partial \sigma}{\partial t} = -\eta_k \dot{\gamma}. \tag{2.118}$$

These individual stresses are combined to give a total stress σ of

$$\begin{aligned} \sigma &= \sum_{k=1}^{N} \sigma_k = \sum_{k=1}^{N} \left[-\int_{-\infty}^{t} \frac{\eta_k}{\lambda_k} e^{\frac{-(t-t')}{\lambda_k}} \dot{\gamma} dt' \right] \\ &= -\int_{-\infty}^{t} \left[\sum_{k=1}^{N} \frac{\eta_k}{\lambda_k} e^{\frac{-(t-t')}{\lambda_k}} \right] \dot{\gamma} dt'. \end{aligned} \tag{2.119}$$

Eq. (2.119) is the generalized Maxwell Model with N relaxation times [13].

2.4.3 Generalized Linear Viscoelastic Model

We can define a generalized linear viscoelastic model by writing the shear stress as follows:

$$\sigma = -\int_{-\infty}^{t} G(t-t') \dot{\gamma}(t') dt'. \tag{2.120}$$

The memory function $G(t-t')$ is equal to $\frac{\eta}{\lambda}e^{\frac{-(t-t')}{\lambda_k}}$ for the Maxwell model and $\sum_{k=1}^{N}\frac{\eta_k}{\lambda_k}e^{\frac{-(t-t')}{\lambda_k}}$ for the generalized Maxwell model. Eq. (2.120) has two factors in the integral: $\dot{\gamma}(t')$, which is related to the kinetics, and $G(t-t')$, which describes material's response to flow. The separability of the two contributions to the stress is a general characteristic of linear viscoelasticity.

2.4.4 Small-Amplitude Oscillatory Shear

The above models can be used to calculate the response of a material to small-amplitude oscillatory shear. In this section, we derive the expressions describing the response of a material to a sinusoidal deformation in the linear viscoelastic regime. Consider a material subjected to a small-amplitude oscillatory deformation given by

$$\gamma(t) = \gamma_0 \sin \omega t. \tag{2.121}$$

The strain rate is

$$\dot{\gamma}(t) = \dot{\gamma}_0 \cos \omega t, \tag{2.122}$$

where $\dot{\gamma}_0 = \gamma_0\omega$. The resulting stress in the material will oscillate at the same frequency, but with a phase shift δ with respect to the strain:

$$\sigma(t) = \sigma_0 \sin(\omega t + \delta) = \sigma_0 \cos\delta \sin \omega t + \sigma_0 \sin\delta \cos \omega t. \tag{2.123}$$

The stress thus has two components, one in phase with the strain and the other 90° out of phase. We define

$$G'(\omega) = \frac{\sigma_0}{\gamma_0}\cos\delta \tag{2.124}$$

and

$$G''(\omega) = \frac{\sigma_0}{\gamma_0}\sin\delta, \tag{2.125}$$

where G' is the elastic modulus and G'' is the viscous modulus, so that

$$\sigma(t) = G'\gamma_0 \sin\omega t + G''\gamma_0 \cos\omega t. \tag{2.126}$$

We also define the complex shear modulus

$$G^* = G' + iG'', \tag{2.127}$$

where $|G^*| = \sigma_0/\gamma_0$.

From the generalized linear viscoelastic model of Eq. (2.120), we can calculate the stress as

$$\begin{aligned} \sigma(t) &= -\int_{-\infty}^{t} G(t-t')\ \dot{\gamma}(t')\ dt' \\ &= -\int_{-\infty}^{t} G(t-t')\ \dot{\gamma}_0 \cos\omega t'\ dt'. \end{aligned} \tag{2.128}$$

We substitute $s = t - t'$ and expand the the cosine term to get

$$\begin{aligned} -\sigma &= \int_0^\infty G(s)\ \dot{\gamma}_0\ \cos\omega t\ \cos\omega s\ ds + \int_0^\infty G(s)\ \dot{\gamma}_0\ \sin\omega t\ \sin\omega s\ ds \\ &= \left[\int_0^\infty G(s)\ \cos\omega s\ ds\right]\gamma_0\ \omega\ \cos\omega t + \left[\int_0^\infty G(s)\ \sin\omega s\ ds\right]\gamma_0\ \omega \sin\ \omega t \end{aligned} \tag{2.129}$$

Comparing this expression with the definitions of G' and G'' in Eq. (2.124) and Eq. (2.125), we find

$$G''(\omega) = \omega\int_0^\infty G(s)\ \cos\omega s\ ds, \tag{2.130}$$

and

$$G'(\omega) \;=\; \omega \int_0^\infty G(s)\ \sin \omega s\ ds. \tag{2.131}$$

Using the expression for $G(s)$ in the generalized Maxwell Model given in Section 2.4.3, these integrals can be carried out to yield

$$G''(\omega) \;=\; \sum_{k=1}^{N} \frac{\eta_k \omega}{1+\lambda_k^2\omega^2} \tag{2.132}$$

and

$$G'(\omega) \;=\; \sum_{k=1}^{N} \frac{\eta_k \lambda_k \omega^2}{1+\lambda_k^2\omega^2} \tag{2.133}$$

The expressions for $G'(\omega)$ and $G''(\omega)$ for the generalized Maxwell model capture important features of material behavior. In particular, for $\omega \ll 1/\lambda_1$ where λ_1, is the longest relaxation time in the system, Eq. (2.132) and Eq. (2.133) predict

$$lim_{\omega\to 0}\ G'(\omega) \propto \omega^2 \tag{2.134}$$

and

$$lim_{\omega\to 0}\ G''(\omega) \propto \omega. \tag{2.135}$$

2.5 Polymer Dynamics

The rheological properties of polymeric fluids are dependent on the dynamics and interactions of the polymer molecules. Polymer molecules are long and easily distorted [14, 15]. In a dilute polymer solution, the probability of chain interactions is very low. In concentrated solutions, the chains overlap and entangle with each other, and the motion of the polymer molecules

is substantially constrained by the neighboring molecules. In this section, we will describe the models used to describe the viscoelastic properties of polymeric fluids in the dilute and concentrated regimes.

2.5.1 Unentangled Polymer Dynamics

In a dilute polymer solution, a polymer molecule can be considered as a random walk [15]. Suppose the polymer chain has N segments and the end to end vector is $\mathbf{R}(N)$. This vector changes rapidly because of the thermal motion of the monomers. The direction of each segment is oriented in an arbitrary direction with respect to the previous one. From the theory of random walks discussed in Section 2.2,

$$\left\langle R(N)^2 \right\rangle = Nl^2, \tag{2.136}$$

where $R = |\mathbf{R}(N)|$. l is called the Kuhn length and is the shortest independently orientable segment length. Since $\mathbf{R}(N)$ is the sum of many independent random vectors, the probability distribution $P(\mathbf{R}(N))$ must have a Gaussian form [12, 15],

$$P(\mathbf{R}(N))d^3\mathbf{R} = \left(\frac{3}{2\pi Nl^2}\right)^{3/2} e^{-\frac{3R^2}{2Nl^2}} d^3\mathbf{R}. \tag{2.137}$$

The entropy S is the product of the Boltzmann constant k and the logarithm of the number of possible states Ω:

$$S = k \ln \Omega. \tag{2.138}$$

Here Ω is the number of the conformations of a freely jointed chain of N monomers with end-to-end vector $\mathbf{R}$, so S is a function of N and $\mathbf{R}$. The probability distribution function is the fraction of all the conformations that actually have an end-to-end vector between $\mathbf{R}$ and

$\mathbf{R} + d\mathbf{R}$:

$$P(\mathbf{R}(N)) = \frac{\Omega(\mathbf{R}, N)}{\int \Omega(\mathbf{R}, N) d\mathbf{R}}. \tag{2.139}$$

The entropy is then

$$S = k \ln P(\mathbf{R}(N)) + k \ln \left[\int \Omega(\mathbf{R}, N) d\mathbf{R} \right]. \tag{2.140}$$

Substitution of Eq. (2.137) into Eq. (2.140) gives

$$S = -\frac{3}{2} k \frac{\mathbf{R}^2}{Nl^2} + \frac{3}{2} k \ln(\frac{3}{2\pi N l^2}) + k \ln \left[\int \Omega(\mathbf{R}, N) d\mathbf{R} \right]. \tag{2.141}$$

The last two terms of Eq. (2.141) depend only on N, not on $\mathbf{R}$, and thus can be denoted as $S(N, 0)$. The entropy can therefore be written as

$$S = -\frac{3}{2} k \frac{\mathbf{R}^2}{Nl^2} + S(N, 0). \tag{2.142}$$

The free energy of the chain is $F = U - TS$, where U is the internal energy and T is the absolute temperature. It can be written as

$$F = \frac{3kT\mathbf{R}^2}{2Nl^2} + F(N, 0). \tag{2.143}$$

The number of conformations of the polymer decreases as the length of the end-to-end vector increases, as indicated by Eq. (2.137), leading to a decrease in polymer entropy and an increase in free energy. From Eq. (2.143), the free energy increases quadratically with the magnitude of $\mathbf{R}$. This implies that the entropic elasticity of an ideal chain satisfies Hooke's law. The force required to hold the chain ends apart by distance R is

$$f = -\frac{\partial F}{\partial R} = -\frac{3kTR}{Nl^2} = -\kappa R, \tag{2.144}$$

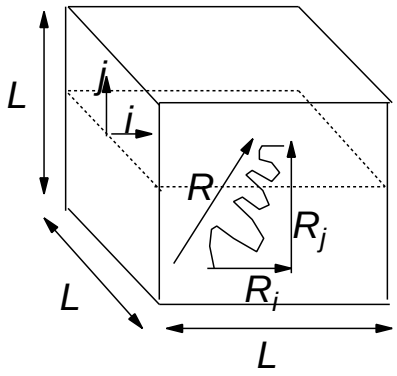

Figure 2.5: Contribution of a single subchain to the stress tensor. After [12].

where $\kappa = 3kT/Nl^2$ is the entropic spring constant of the polymer chain. κ is proportional to T/N. The entropic nature of the elasticity in polymers distinguishes them from other elastic materials.

Now we consider a small cubic volume of side L in a polymeric fluid, as shown in Fig. 2.5. It contains c/N subchains of length N per unit volume, where c is the monomer concentration. The force applied by the i^{th} segment transmitted across the j^{th} plane is, using Eq. (2.144), κR_i. The probability that one segment cuts a given plane is R_i/L. The area of the j^{th} plane is L^2. Consequently, the contribution of this force to the mean local stress σ_{ij} is $\kappa R_i R_j/L^3$. The sum over all segments can be replaced by an average over the ensemble multiplied by the number of segments, which is cL^3/N, giving [12]

$$\sigma_{ij} = \frac{3kTc}{N^2 l^2} \langle R_i R_j \rangle . \tag{2.145}$$

Rouse Model

The simplest model for polymer dynamics in dilute solution is the Rouse Model [12, 14, 15], in which a polymer molecule is considered to be a Gaussian chain. Each monomer experiences a random thermal force, a net entropic force from neighboring monomers, and a local frictional drag force due to its surroundings. The balance of the three forces on a chain of N segments

is the Rouse equation,

$$\varsigma_0 \frac{\partial \mathbf{R}}{\partial t} = \kappa \frac{\partial^2 \mathbf{R}}{\partial n^2} + f(n,t), \tag{2.146}$$

where n is the segment number and ς_0 is the drag-force coefficient. The first term on the right hand side of Eq. (2.146) is the thermodynamic force at each point on the chain. Since the polymer chains are self-similar objects, they exhibit dynamic self-similarity, that is, smaller sections of a polymer chain with g monomers relax just like a whole polymer chain that has g monomers. Therefore the relaxations of a polymer can be described in terms of many different relaxation modes [14, 15]. We write $\mathbf{R}(n,t)$ as a sum over these modes

$$\mathbf{R}(n,t) = \mathbf{X}_0 + 2\sum_{p=1}^{\int} \mathbf{X}_p(t) \cos\frac{p\pi n}{N}, \tag{2.147}$$

where $\mathbf{X}_p$ are the time-dependent amplitudes of the Rouse modes of the polymer chain:

$$\mathbf{X}_p = \frac{1}{N}\int_0^N \mathbf{R}(n,t) \cos\frac{p\pi n}{N} dn. \tag{2.148}$$

Eq. (2.146) can be written in terms of the $\mathbf{X}_p$. The modes decouple, and the amplitude of each mode is found to obey a Langevin equation,

$$\varsigma_p \frac{\partial \mathbf{X}_p}{\partial t} = -\kappa_p \mathbf{X}_p + f_p(n,t), \tag{2.149}$$

where $\kappa_p = 6kTp^2\pi^2/Nl^2$ and $\varsigma_p = 2N\varsigma_0$.

To investigate the rheological behavior in the Rouse model, we need to derive an expression for the modulus $G(t)$ discussed in Section 2.4. Eq. (2.145) for the stress has a very simple representation in terms of Rouse mode amplitudes:

$$\sigma_{ij} = \frac{c}{N}\sum_p \kappa_p \left\langle X_{pi}(t) X_{pj}(t) \right\rangle. \tag{2.150}$$

where i and j have the same meanings as in Eq. (2.145). We consider the relaxation modulus $G(t)$ in a step-strain test. After a strain with a size of γ is applied to a polymer chain, the $X_p(t)$ deform affinely–that is, all modes deform by the same relative amount. The deformation of $X_{pi}(t)$ is proportional to γ, with $X_{pi}(0^+) = X_{pi}(0^-) + \gamma X_{pj}(0^-)$. Thus the stress is

$$\sigma_{ij}(0^+) = \gamma \frac{c}{N} \sum_p \kappa_p \left\langle X_{pj}(0^-) X_{pj}(0^-) \right\rangle = \gamma \frac{c}{N} \sum_p k_B T, \tag{2.151}$$

where we use the time-correlation function of the mode amplitudes $\langle X_p(t) X_q(t') \rangle = \frac{k_B T}{\kappa_p} \delta_{pq} e^{-|t-t'|/\tau_p}$ predicted by the fluctuation-dissipation theorem [14]. Here τ_p is the relaxation time of mode p, which is related to the longest relaxation time τ_1 by $\tau_p = \tau_1/p^2$. τ_1 is the Rouse time of a polymer, that is, the time for a molecule to diffuse a distance of the order of its own size [14]. The details of proof are shown in Ref. [33]. The time-dependent modulus is then given as

$$G(t) = \frac{\sigma_{ij}}{\gamma} = \frac{k_B T c}{N} \sum_p e^{-2t/\tau_p} = \frac{k_B T c}{N} \sum_p e^{-2p^2 t/\tau_1}. \tag{2.152}$$

If $t \ll \tau_1$, the sum in Eq. (2.152) can be written in the form of an integral:

$$G(t) = \frac{\sigma_{ij}}{\gamma} = \frac{k_B T c}{N} \int dp e^{-2p^2 t/\tau_1} = \frac{k_B T c}{N} (t/\tau_1)^{-1/2}. \tag{2.153}$$

Recalling the relation between $G^*(\omega)$ and $G(t)$ given by Eqs. (2.128)—Eq. (2.131), we can calculate the storage and the loss moduli of a linear Rouse chain [15]. The results are

$$G'(\omega) \approx \frac{k_B T c}{N} \frac{(\omega\tau_1)^2}{\sqrt{[1 + (\omega\tau_1)^2][\sqrt{1 + (\omega\tau_1)^2} + 1]}}. \tag{2.154}$$

and

$$G''(\omega) \approx \frac{k_B T c}{N} \omega\tau_1^2 \sqrt{\frac{(\sqrt{1 + (\omega\tau_1)^2} + 1}{1 + (\omega\tau_1)^2}}. \tag{2.155}$$

When $\omega \gg 1/\tau_1$, the Rouse model predicts $G'(\omega) \approx G''(\omega) \propto \omega^{1/2}$.

2.5.2 Entangled Polymers

The Reptation Model

In concentrated solutions of long polymers, the polymer chains are entangled. This imposes constrains on their motion since they can not pass through each other. In this case, the collective effects of all surrounding chains can be represented using a tube model, as introduced by Edwards [14]. de Gennes then introduced the reptation model based on the tube model [14, 15]. In the reptation model, an entangled chain diffuses along its confining tube. The motion of the chain along the contour of the tube is unhindered while displacement of the monomers perpendicular to the contour of the tube is restricted by the surrounding chains.

We consider N_e monomers in a strand of entanglement segments. The tube diameter a is $a \approx \sqrt{N_e}b$, where b is the segment size. The tube has an average length of $L = aN/N_e = b^2N/a$ [12]. The diffusion of small loops along the contour of the tube is characterized by the Rouse friction coefficient $N\varsigma_0$ and a corresponding diffusion coefficient D_c given by

$$D_c = \frac{k_B T}{N\varsigma_0}, \tag{2.156}$$

where N is the number of monomers in the chain. The time τ_{rep} for the molecule to diffuse out of the tube is then

$$\tau_{rep} \approx L^2/D_c = \frac{b^2\varsigma_0 N_e^2}{k_B T}\left(\frac{N}{N_e}\right)^3. \tag{2.157}$$

The first factor on the right–hand side of Eq. (2.157) is the Rouse time τ_e of a strand containing N_e monomers:

$$\tau_e = \frac{b^2\varsigma_0 N_e^2}{k_B T} = \tau_0 N_e^2. \tag{2.158}$$

τ_0 is the Rouse time of a single monomer, over which a free monomer would diffuse a distance of order of its length b.

When $t < \tau_e$, the chain can move a small distance without feeling the constrains of the surrounding entanglements and hence the moduli $G(t)$ and $G^*(\omega)$ have the same behavior as predicted by Eq. (2.153) of the Rouse model discussed above. Around $t = \tau_e$, using $\tau_e = \tau_0 N_e^2$ and $\tau_1 = \tau_0 N^2$, Eq. (2.153) predicts a plateau value of $G(t)$, and therefore a plateau of $G'(\omega)$. The value of the plateau is approximately $G_e(t) = \frac{k_B T c}{N_e}$. When $t > \tau_e$, the polymer feels the restricting effects of the tube and moves by reptation. The details for the calculation of $G(t)$ are shown in Ref. [14], which gives

$$G(t) = G_e \frac{8}{\pi^2} \sum_{odd\ p} \frac{1}{p^2} e^{-t/\tau_p}, \tag{2.159}$$

where $\tau_p = \tau_{rep}/p^2$. Eq. (2.159) shows that reptation model predicts a nearly exponential decay of $G(t)$ for a nearly monodisperse polymer solution. The viscous and elastic moduli obtained from $G(t)$ in Eq. (2.159) have the same form and power law dependence as shown earlier in Eqs. (2.134) and (2.135).

2.5.3 Gelation

Concepts and Definition

Gelation is the conversion of a liquid to a disordered solid by formation of a network of chemical or physical bonds between molecules or particles in the liquid [14]. The liquid precursor is called the "sol," and the solid formed from it is the "gel".

Polymeric gels can be categorized as chemical or physical gels depending on the way the molecules bond together. In chemical gels, chemical reactions, such as addition polymerization or cross-linking, are involved. In physical gels, gelation occurs as a result of intermolecu-

lar association leading to network formation. While chemical bonds are covalent attachments between atoms and are typically permanent at the temperatures of interest, intermolecular associations involve weak, reversible bonds or clusters produced by van der Waals forces, electrostatic attractions, or hydrogen bonding.

Stauffer and de Gennes have pointed out that gelation is a connectivity transition which can be described by a bond percolation model [32, 33]. Imagine a container of monomers which occupy the sites of a lattice. We allow bonds connecting monomers to randomly form between neighboring sites. The fraction of all possible bonds that are formed at any point in the reaction is called the extent of percolation p. p is zero at the beginning of the reaction. As p increases, more and more monomers link together. Eventually, at a particular value, $p = p_c$, a lattice-spanning cluster appears. This corresponds to the percolation transition or a gel point. If all the possible bonds are formed, $p = 1$.

A polymer system slightly below the gel point is a polydisperse mixture of branched aggregates of polymer molecules. Slightly beyond the gel point, it is similar, but one large cluster percolates through the entire system. The clusters formed near the gel point show fractal or self-similar character, which implies that large clusters near the gel point look the same at any magnification. The quantity $\varepsilon = |(p - p_c)|/p_c$ is the distance from the gel point. The cluster size distribution at $\varepsilon = \varepsilon_1$ is the same as at a smaller value, $\varepsilon = \varepsilon_2$, if one uniformly magnifies the size of all clusters formed at ε_1. Thus most of the cluster properties near the gel point show a power-law scaling with ε. For example, the mass of the largest cluster scales as $M^* \propto \varepsilon^{-1/\sigma}$, where $\sigma \approx 1/2$ in the classical theory [32] and $\sigma \approx 0.45$ in the percolation theory [14]. The mass M^* is also related to the correlation length ξ of the clusters through the fractal dimension D by $M^* \propto \xi^D$, where a 3D percolation prediction gives $D \approx 2.52$ [16].

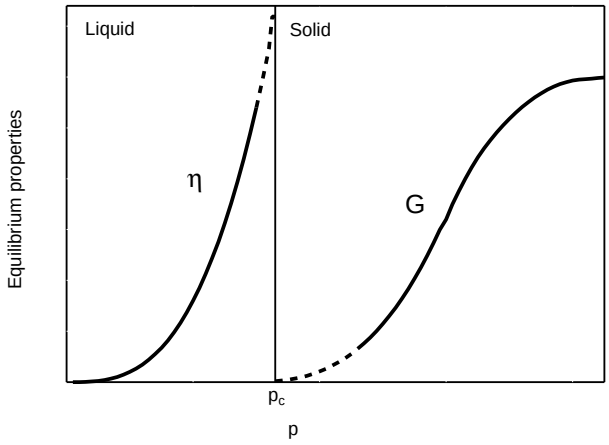

Figure 2.6: Illustration of the dependence of zero-shear viscosity η and equilibrium modulus G on extent of percolation p for a cross-linking system. p_c is the gel point.

Scaling of Rheological Properties near the Gel Point

The viscoelastic properties of materials change greatly during the sol-gel transition as the mobility of the molecules changes due to aggregation of the chains [16]. The zero-frequency viscosity diverges as the system approaches the gel point p_c, while the zero-frequency elastic modulus grow continually from zero after the gel point, as shown in Fig. 2.6 [14]. As the polymer clusters increase in size and an infinite cluster appears, the system passes from being a viscous liquid to being a viscoelastic solid.

In the sol state, where the system is liquid-like, the frequency dependence of the storage modulus $G'(\omega)$ and loss modulus $G''(\omega)$ at low frequency are those of an ordinary polymeric liquid: $G' \propto \omega^2$ and $G'' \propto \omega^1$, as discussed in Section 2.4.1. In the gel state, when the polymers tend to form a network, the rheological behavior will be that of a solid [16]: $G'' \ll G' \propto \omega^0$.

Near the gel point, the largest mass M^* of the clusters is related to the relative distance to the gel point ε by $M^* \propto \varepsilon^{-1/\sigma}$, as discussed above. If the longest relaxation time $1/\omega^*$ of a polymer is proportional to its mass, $1/\omega^* \propto 1/\omega_0 \varepsilon^{-1/\sigma}$. One also expects that at frequencies

higher than ω^*, the complex elastic modulus will also show power-law behavior [16]:

$$G^* \propto (i\omega/\omega_0)^u = (\omega/\omega_0)^u e^{i\delta}, \tag{2.160}$$

where $\delta = \arctan(G''/G') = u\pi/2$. Eq. (2.160) implies a similar power-law behavior for the real and imaginary parts of the shear modulus at the gel point. The rheological behavior of the system at the gel point is neither liquid-like nor solid-like and has no characteristic relaxation time [16].

BIBLIOGRAPHY

[1] F. Reif, *Fundamentals of Statistical and Thermal Physics* (McGraw-Hill, New York, 1965).

[2] G. D. J. Phillies, *Elementary Lectures in Statistical Mechanics* (Springer, New York, 2000).

[3] D. J. Acheson, *Elementary Fluid Dynamics* (Oxford University Press Inc., New York, 1990).

[4] L. Chen, *Thermal and Statistical Physics* (Jilin University Press, Changchun, 1978).

[5] R. Kubo, Rep. Prog. Phys. **29**, 255 (1966).

[6] W. Brown, ed., *Light Scattering: Principles and Development* (Oxford University Press, London, 1996).

[7] P. Linder and Th. Zemb, *Neutrons, X-rays and Light: Scattering Methods Applied to soft Condensed Matter* (Elseivier B. V., Amsterdam, 2002).

[8] K. S. Schmitz, *Dynamic Light Scattering by Macromolecules* (Academic Press, San Diego, 1993).

[9] W. Brown, ed., *Dynamic Light Scattering: The Method and Some Application* (Oxford University Press, London, 1996).

[10] P. N. Pusey and W. van Megen, Physica A, **157**, 705 (1989).

[11] M. Shibayama and T. Norisuye, Bull. Chem. Soc. Jpn. **75**, 641 (2002).

[12] M. E. Cates and M. R. Evans, *Soft and Fragile Matter* (Institute of Physics Publishing, Bristol, 2001).

[13] F. A. Morrison, *Understanding Rheology* (Oxford University Press, New York, 2001).

[14] R. G. Larson, *The Structure and Rheology of Complex Fluids* (Oxford University Press, New York, 1999).

[15] M. Rubinstein and R. Colby, *Polymer Physics* (Oxford University Press, New York, 2003).

[16] J. P. Cohen Addad, *Physical Properties of Polymertic Gels* (John Wiley and Sons Inc., New York, 1996)

[17] R. Brown, Philos. Mag. **4**, 161 (1828).

[18] A. Einstein, Ann. Phys. **17**, 549 (1905).

[19] J. B. Perrin, Ann. Chem. Phys. **18**, 1 (1909).

[20] J. C. Crocker and D. G. Grier, J. Coll. Interf. Sci. **179**, 298 (1996).

[21] T. G. Mason and D. A. Weitz, Phys. Rev. Lett. **74**, 1250 (1995).

[22] T. G. Mason, H. Gang, and D. A. Weitz, J. Mol. Struct. **383**, 81 (1996).

[23] T. G. Mason, Rheol. Acta. **39**, 371 (2000)

[24] T. G. Mason, A. Dhople, and D. Wirtz. Mater. Res. Soc. Symp. Proc. **463**, 153 (1997).

[25] N. Pottier, Physica A **345**, 472 (2005).

[26] J. C. Crocker, M. T. Valentine, Eric R. Weeks, T. Gisler, P. D. Kaplan, A. G. Yodh, and D. A. Weitz, Phys. Rev. Lett. **85**, 888 (2000).

[27] B. R. Dasgupta, S. Y. Tee, J. C. Crocker, B. J. Frisken, and D. A. Weitz, Phys. Rev. E **65**, 051505 (2002).

[28] B. R. Dasgupta and D. A. Weitz, Phys. Rev. E **71**, 021504 (2005).

[29] M. Doi and S. F. Edwards, *The Theory of Polymer Dynamics* (Oxford University Press, New York, 1986).

[30] P. J. Flory, J. Chem. Phys. **10**, 51 (1942).

[31] W. H. Stochmayer, J. Phys. Chem. **11**, 45 (1943).

[32] D. Stauffer, *Introduction to Percolation Theory* (Taylor and Francis, London, 1985).

[33] P. G. de Gennes, *Scaling Concepts in Polymer Physics* (Cornell University Press, Ithaca, 1979).

Chapter 3

Experiment

3.1 Introduction

In this Chapter, we briefly describe the materials and the experimental techniques used in this work. The details of the sample preparation and specific measurements will not be given here, as they are included in the individual results chapters. As a new atomic force microscopy technique will be discussed in Chapter 4, we describe the components and basic operation of the AFM in Section 3.3. Rheometry was used to characterize the materials studied in Chapters 5 and 6. In Section 3.4 we give a brief description of shear rheometry and explain the working equations, particularly for the parallel-plate geometry. Dynamic light scattering was used to study the dynamics of the samples in Chapter 5 and the motion of tracer particles in the samples in Chapter 6, and the experimental setup will be described Section 3.5. A particle-tracking technique was used to study the local structure and microrheology of the samples in Chapter 6. We describe the experimental setup and give a brief description of the data analysis procedure in Section 3.6. The theoretical basis of these methods has been presented in Chapter 2.

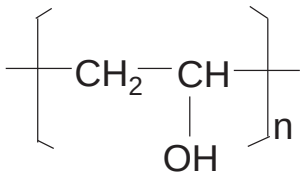

Figure 3.1: Molecular structure of poly(vinyl alcohol).

3.2 Materials

3.2.1 Poly(vinyl alcohol)

Poly(vinyl alcohol) (PVA) is a synthetic water-soluble polymer. It has a relatively simple chemical structure, shown in Fig. 3.1, with a pendant hydroxyl group in each monomer. Because the vinyl alcohol monomer is not stable, but instead rearranges to its tautomer, acetaldehyde [1], PVA is synthesized by hydrolysis of poly(vinyl acetate) (PVAc), which is produced by the polymerization of the vinyl acetate monomer. PVA is available with a variety of degrees of hydrolysis according to manufacturer and application. Commercial PVA grades are available with degree of hydrolysis above 98.5%. A range of molecular weights of PVA is also available and, because of the polymerization and subsequent hydrolysis process, a polydispersity index of 2 to 2.5 is common. The properties of PVA, including solubility, viscoelasticity and mechanical strength of PVA gels are affected by its structure, degree of hydrolysis and molecular weight [2].

PVA has been widely used for biomedical and pharmaceutical applications [3, 4, 5], because it is non-toxic, biocompatible, and easy to process. PVA swells substantially in water and forms gels that are rubbery and elastic in nature, so it is capable of simulating natural tissue and can be readily accepted into the body. PVA gels have potential applications as soft tissue replacements [6], the lining of artificial hearts [3], artificial skin [5], articular cartilage [7], and so on. They have also been used for contact lenses [8] and drug delivery applications [9].

PVA must be crosslinked to make it insoluble in water for these applications. This can be done either by chemical or physical crosslinking. In the chemical crosslinking process, one can use crosslinking agents such as formaldehyde and other monoaldehydes [10, 11]. In the presence of sulfuric acid, acetic acid, or methanol, these crosslinking agents will form acetal bridges between the pendant hydroxyl groups of the PVA chains. One disadvantage of this process is that residual amounts of the toxic crosslinking agent will remain, which is undesirable for biomedical or pharmaceutical applications [1]. An alternate way of chemical crosslinking is to use ionizing radiation such as γ-rays or electron beams [12, 13]. The radiation breaks some of the chemical bonds and creates free radicals, which then recombine to form the crosslinks [13]. This technique has unwanted effects as well, such as solidification in injectable formulations or bubble formation [1, 13].

Physical crosslinking can address the toxicity issues associated with the chemical crosslinking process, because no toxic crosslinking agent is involved. Physical crosslinking can be achieved by cyclic freezing and thawing of a PVA solution [4, 5]. It is believed that freezing of water in the PVA solution forces it to phase-separate, resulting in PVA-rich and PVA-poor domains [13, 14]. During thawing, PVA crystallites are formed due to hydrogen bonding in the PVA-rich domains. The crystals serve to physically crosslink the PVA network. Another method of physical crosslinking is called theta–gel method [15]. In this case, the addition of a gelling agent, such as poly(ethylene glycol) (PEG), to PVA solutions reduces the quality of the solvent, forcing the PVA to phase separate and crystallize, again forming a physically crosslinked hydrogel network.

The PVA hydrogels studied in Chapter 4 are made by the thermal cycling method, while the gels studied in Chapters 5 and 6 are made by the theta-gel method, using PEG as the physical crosslinking agent. The details of the sample preparation will be given in those chapters.

3.3 Techniques

3.3.1 Atomic Force Microscopy

The atomic force microscope (AFM) is a tool for studying surface properties of materials at the submicron level. The components and operation of the AFM are illustrated in Fig. 3.2. The sample is mounted on a piezoelectric scanner. A sharp tip is located at the free end of a microfabricated cantilever. A laser beam is directed onto the back of the cantilever and a quadrant photodetector is used to measure the location of the reflected beam. During a measurement, the tip is brought close to or in contact with the sample surface and the force between the tip and the sample surface causes the cantilever to bend. As the cantilever bends, the position of the reflected beam at the photodetector shifts. The measured cantilever deflection signal is then passed through an electronic feedback system which causes the scanner to move the sample up or down to compensate for the cantilever deflection, and to a computer which generates a map of surface topography.

If the distance between the tip and the sample surface is less than a few Ångstroms, the force between the tip and the sample is repulsive. This is called the contact regime. If the tip is held on the order of tens to hundreds of angstroms from the sample surface, then the force between them is attractive. This is called the non-contact regime. AFM working modes are generally categorized as contact and non-contact imaging modes according to the distance and force regime used. Depending on the situation, the forces exerted on an AFM tip can include mechanical forces, van der Waals forces, capillary forces, and chemical bonding, among others, but the interatomic van der Waals force is the most common.

Contact AFM

Contact AFM, or repulsive mode, typically uses a cantilever with a low spring constant k. As the sample scans beneath the AFM tip, the contact force between the tip and the sample

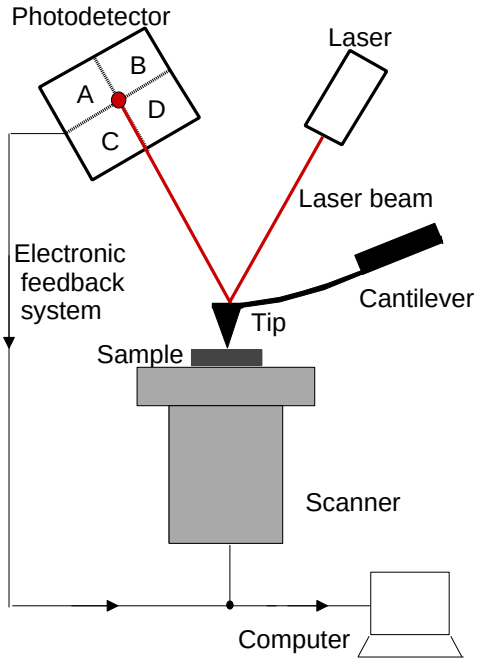

Figure 3.2: Schematic of an AFM.

surface causes the cantilever to bend to accommodate changes in the sample topography. As shown in Fig. 3.2, a laser beam is reflected off the back of the cantilever onto a position-sensitive photodetector, which can measure the displacements of the beam as small as 10 Å. As the cantilever bends, the position of the laser beam on the detector shifts. Using this method, sub-Angstrom vertical movements of the cantilever tip can be detected.

To generate topographic data, the AFM can operate in either constant-height or constant-force mode. In constant-height mode, the height of the scanner is fixed and the spatial variation of the cantilever deflection is related to the topography of the sample surface. In constant-force mode, the deflection of the cantilever is used as the input to a feedback circuit which moves the scanner up and down to keep the cantilever deflection constant. In this case, the image is generated from the scanner's motion. As the cantilever deflection is held constant, the total force applied to the sample is also constant.

The constant-height mode is often used when the force variations and cantilever deflection

are small, for example, when taking atomic-scale images of atomically flat surfaces. It is also used for recording real-time images of changing surfaces when a high scan speed is needed. In contrast, the scan speed in constant-force mode is limited by the response time of the feedback circuit. Because the total force exerted on the sample by the tip is well controlled, however, constant-force mode is generally preferred for most applications. In Chapter 4, we will describe a new method for measuring the surface viscoelastic properties of soft materials by modifying the feedback circuit of an AFM working in constant-force contact mode.

Non-Contact AFM

In non-contact AFM modes, the distance between the tip and the sample is in the non-contact regime and the van der Waals force is attractive. An AFM cantilever is vibrated near the surface of a sample at a frequency slightly above its resonant frequency. The resonant frequency of a cantilever varies with the force gradient experienced by the cantilever. As the tip vibrates, the feedback loop maintains a constant oscillation amplitude by adjusting the average tip-to-sample distance, allowing construction of a topographic image of the sample surface.

In non-contact mode, the magnitude of the force is generally about 10^{-12} N, which is appropriate for studying soft or elastic samples. The spring constant of the AFM cantilever is higher than that used in contact mode, however. This makes the signal small and difficult to measure, so a sensitive AC detection system is needed.

Because of the difficulty in keeping the tip close enough to the sample while preventing it from sticking to the surface in ambient conditions, AFM tapping mode is more commonly used instead of non-contact mode. In tapping mode, the cantilever is driven to oscillate up and down at a fixed frequency near its resonance frequency. The amplitude of the resulting motion is the input to the feedback circuit and is used to construct topographic images of the sample surface.

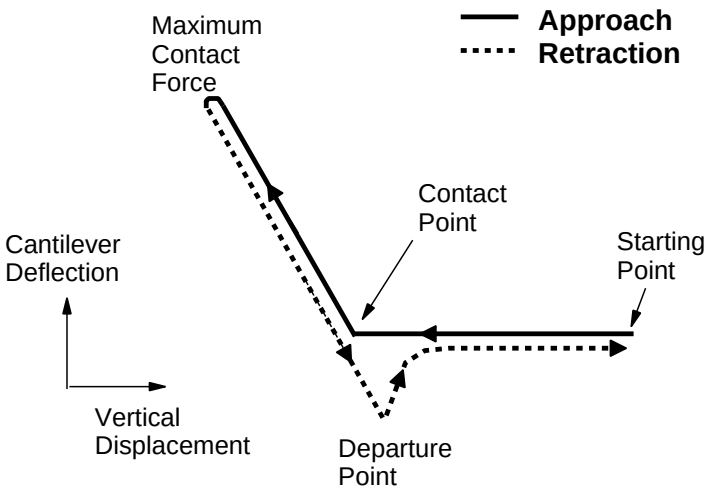

Figure 3.3: Schematic of a force curve measured by the AFM when the tip approaches and retracts from the sample surface.

Force-Volume Imaging

In addition to topographic imaging, the AFM can also measure the net force experienced by the cantilever when the tip approaches a sample surface and is then withdrawn. A sketch of such a force curve is shown in Fig. 3.3. During this process, the sample is moved vertically by the scanner through a known displacement, and the deflection of the cantilever is monitored. When the separation between the tip and the sample surface is large, the cantilever is not deflected, as shown by the flat part of the approach curve in Fig. 3.3. As the separation decreases, the tip eventually makes contact with the sample surface, and the cantilever is deflected upward. The force experienced by the cantilever is strong in this range, which can lead to sample deformation. The upwards motion is then stopped at a predetermined force and the sample motion is reversed. Adhesive forces may lead to negative deflection of the cantilever when the tip is withdrawn, as shown in Fig. 3.3. Finally the tip completely leaves the surface when the adhesive force is exceeded and returns to the original zero-deflection state.

The force curve measurement can be performed at an array of points on the sample surface,

generating what is referred to as a force-volume data set. This force-volume imaging technique has been widely used to study the elastic properties of material surfaces [16, 17]. In Chapter 4, we will compare the viscoelasticity of a material surface measured by our new AFM technique with that measured by this force-volume technique.

3.3.2 Shear Rheometry

Description of a Stress-Controlled Shear Rheometer

In this work, we used an AR 1500ex stress-controlled rheometor, manufactured by TA Instruments (New Castle, DE). A schematic diagram of the main instrument components is shown in Fig. 3.4. The head of the rheometer, which is mounted in the upper part of the column, can move vertically. A motor inside the head rotates a spindle, which is supported by an air bearing in the head. An encoder inside the head can determine the angular position of the spindle. During a measurement, the sample is contained between the lower plate, on the base of the rheometor, and a removable upper plate which is attached to the rotating spindle. A specified deformation or stress is applied to the sample by the motion of the upper plate, and the angular velocity of the spindle is measured and recorded by a computer. The temperature of the lower plate can be accurately controlled between 5 °C and 150 °C.

Parallel-Plate Geometry

In our experiments, we used a parallel-plate rheometer tool, shown in Fig. 3.5. In this geometry, the sample is contained between two circular plates and the upper plate is rotated at a constant angular velocity Ω. In analyzing this system, we use cylindrical coordinates as indicated in Fig. 3.5. The shear flow driven by the rotation of the upper plate is only in the

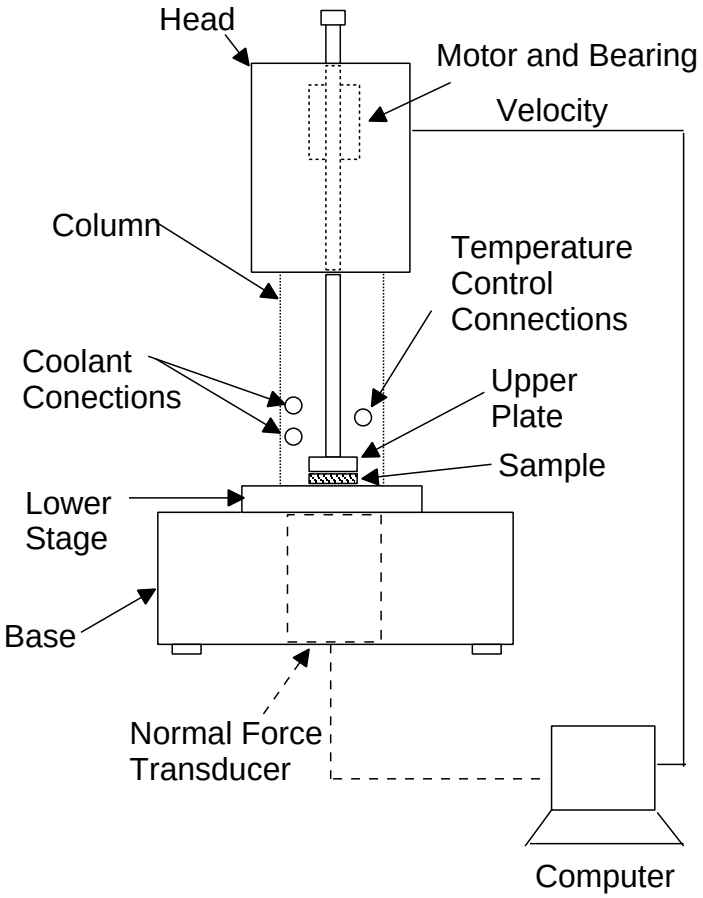

Figure 3.4: Schematic of the AR 1500ex rheometor.

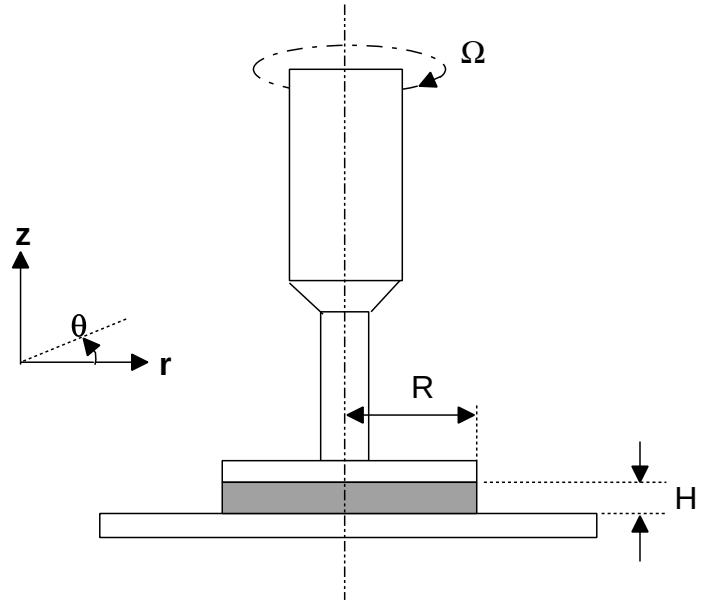

Figure 3.5: Parallel plate geometry.

θ-direction, and the corresponding velocity components are:

$$\mathbf{v} = \begin{pmatrix} 0 \\ v_\theta \\ 0 \end{pmatrix}, \tag{3.1}$$

where v_θ is the component of $\mathbf{v}$ in the θ direction. Ignoring edge effects, the gradient of the shear flow is in the z-direction, and we can write

$$v_\theta = A(r)z + B(r), \tag{3.2}$$

where $A(r)$ and $B(r)$ are functions of r to be determined from the boundary conditions. As the lower plate is kept fixed while the upper plate is rotating, the boundary conditions are $v_\theta = 0$ at $z = 0$ and $v_\theta = r\Omega$ at $z = H$. Applying these boundary conditions to Eq. (3.2) yields

$$v_\theta = \frac{r\Omega z}{H}. \tag{3.3}$$

The shear rate is then given by

$$\dot{\gamma} = \frac{\partial v_\theta}{\partial z} = \frac{r\Omega}{H}. \tag{3.4}$$

The shear strain can be calculated from the shear rate as

$$\gamma = \int_0^t \dot{\gamma} dt' = \int_0^t \frac{r\Omega}{H} dt' = \frac{r\Omega t}{H}. \tag{3.5}$$

The total torque at the upper plate can be calculated as

$$M = \int_A (stress)(lever\ arm) dA = \int_0^R (\tau_{z\theta}|_{z=H})(r)(2\pi r dr). \tag{3.6}$$

The shear stress is a function of r, and is related to viscosity $\eta(r)$ by

$$\eta(r) = -\frac{\tau_{z\theta}}{\dot{\gamma}(r)}. \tag{3.7}$$

Using this, Eq. (3.6) becomes

$$M = 2\pi \int_0^R \eta(r)\dot{\gamma} r^2 dr. \tag{3.8}$$

To find a relation between the torque and the measured shear rate, we further replace the variable r in the integral with $\dot{\gamma}$, using $\dot{\gamma} = \dot{\gamma}_R r/R$, where $\dot{\gamma}_R$ is the shear rate at $r = R$ [18]. Eq. (3.8) becomes

$$M = \frac{2\pi R^3}{\dot{\gamma}_R^3} \int_0^{\dot{\gamma}_R} \eta \dot{\gamma}^3 d\dot{\gamma}. \tag{3.9}$$

To eliminate the integral, we rearrange Eq. (3.9) and differentiate both sides by $\dot{\gamma}_R$ using the Leibnitz rule:

$$\frac{M}{2\pi R^3}\dot{\gamma}_R^3 = \int_0^{\dot{\gamma}_R} \eta \dot{\gamma}^3 d\dot{\gamma} \tag{3.10}$$

$$\frac{d}{d\dot{\gamma}_R}\left[\left(\frac{M}{2\pi R^3}\right)\dot{\gamma}_R^3\right] = \int_0^{\dot{\gamma}_R} \frac{\partial}{\partial \dot{\gamma}_R}(\eta\dot{\gamma}^3) d\dot{\gamma} + \eta(\dot{\gamma}_R)\dot{\gamma}_R^3 \tag{3.11}$$

The first term on the right-hand side is zero, and after rearrangement we obtain the equation for the steady shear viscosity measured in a parallel-plate geometry:

$$\eta(\dot{\gamma}_R) = \frac{M}{2\pi R^3 \dot{\gamma}_R}\left[3 + \frac{d\ln(M/2\pi R^3)}{d\ln\dot{\gamma}_R}\right]. \tag{3.12}$$

Eq. (3.12) shows how the viscosity is determined from the torque and shear rate, which are the experimental quantities.

The parallel-plate geometry is also used in small-amplitude oscillatory shear measurements. Detailed calculations can be found in Ref. [19]. The elastic and viscous moduli can be expressed in terms of the torque as

$$G' = \frac{2HM_0\cos\delta}{\pi R^4\theta_0} \tag{3.13}$$

$$G'' = \frac{2HM_0\sin\delta}{\pi R^4\theta_0} \tag{3.14}$$

where M_0 and θ_0 are the amplitudes of the oscillatory torque and rotation respectively, and δ is the phase difference between the shear rate and the shear stress. In practice, all of the quantities are calculated directly by the software that controls the rheometer.

3.3.3 Dynamic Light Scattering

The experimental setup used for our dynamic light scattering experiments is shown in Fig. 3.6. The instrument is an ALV-CGS3 spectrometer/goniometer produced by ALV-Laser GmbH (Langen, Germany). It consists of a laser, beam steering optics, a goniometer that contains the sample vat and defines the scattering geometry, a photodetector and a digital correlator for calculating the autocorrelation function of the scattered intensity in real time. The source used here is a helium-neon laser with wavelength of 632.8 nm and a power of 22 mW.

As shown in Fig. 3.6, mirrors are used to steer the laser beam to illuminate the sample and an attenuator is used to prevent damage to the detector. A lens is used to focus the incoming beam onto a cylindrical quartz cell containing the sample. The cell is placed in a vat containing toluene, whose reflective index is close to that of glass, to reduce scattering by the sample cell wall. The digital correlator is mounted on an arm which can rotate around the center of the sample cell, allowing collection of scattered light at angles from 15° to 150°, corresponding to scattering vectors from 0.0004 $Å^{-1}$ to 0.003 $Å^{-1}$. Two photodiodes are used to measure the intensity of the incident light and the light transmitted through the sample.

The detector is a photomultiplier tube that collects the scattered photons at a particular angle. A bright speckle will be observed when the scattered light interferes constructively at the detector. The detected signal is amplified and passed through the correlator. A computer connected to the light scattering instrument via a PCI card controls the instrument and stores data for later analysis. The correlator used here has 288 channels with delay times in the range of 125 ns to 2147 s. The number and range of delay times can be set by the control software [20].

3.3.4 Optical Microscopy and Particle Tracking

Fluorescence Microscopy

In the particle tracking measurements, fluorescent microspheres are suspended in the samples to be studied and their motion is monitored and recorded over time using a camera connected to a fluorescence microscope. The microscope used in this work is an Olympus IX2 (Olympus Corporation, Tokyo, Japan) inverted fluorescence microscope and the camera is a Lumenera Infinity2 digital CCD camera (Lumenera Corporation, Lawrenceville, GA). The working principle of the fluorescence microscope is sketched in Fig. 3.7. The illumination is filtered by the excitation filter, which transmits wavelengths near the excitation wavelength of the fluorescent dye contained in the spheres. The filtered light excites the sample after being

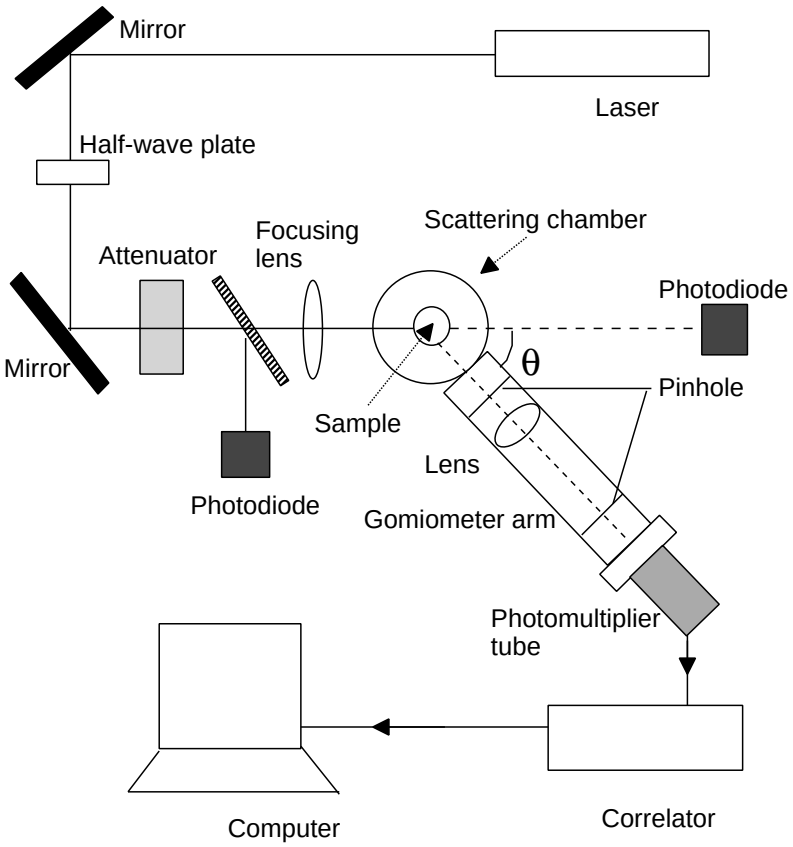

Figure 3.6: Schematic of the light scattering apparatus.

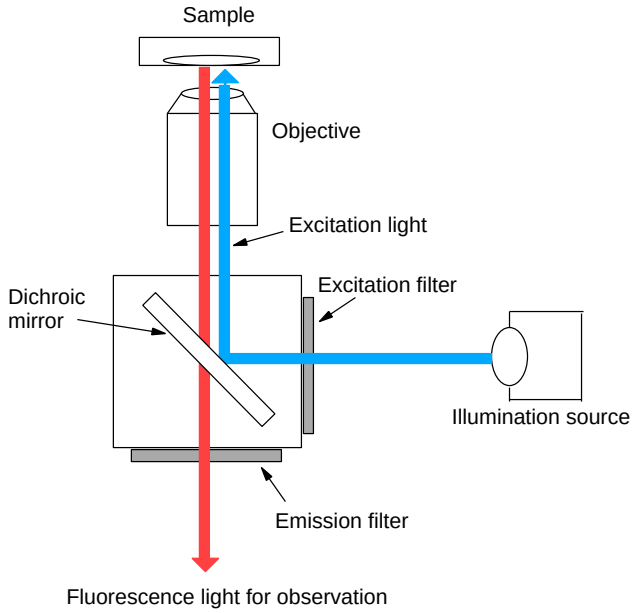

Figure 3.7: A schematic diagram of the light path of an inverted fluorescence microscope.

reflected by a dichroic mirror, which reflects light below a cur-off wavelength and transmits light above the cut-off. The longer-wavelength light emitted by the sample passes through the dichroic mirror and is filtered for observation. It is steered either to the eyepieces for observation or to the camera port for recording. Videos with a frame rate of 12 frames per second and duration up to 10 minutes are recorded, then converted to tiff image-stacks and stored in a computer for further analysis.

Image Processing

The image processing and data analysis were done using a particle tracking program written by Crocker, *et al.* [21, 22] and coded in IDL software [23]. The time evolution of the distribution of particles can be described by

$$\rho(\mathbf{r}, t) = \sum_{i=1}^{N} \delta(\mathbf{r} - \mathbf{r}_i(t)), \tag{3.15}$$

where $\mathbf{r}_i$ is the location if the i^{th} particle in a field of N particles at time t. The particle tracking program enables extraction of the trajectories $\mathbf{r}_i(t)$ of individual microsheres from a set of images. Generally, the main steps involve correcting imperfections in the individual images, locating candidate particles, discriminating false identifications and linking the particle locations into trajectories.

Digital images may contain imperfections such as geometric distortion, nonuniform contrast and noise. These imperfections introduce errors in to $\rho(\mathbf{r}, t)$. To correct them, a background image can be subtracted. Because the digitization noise tends to be purely random with a correlation length $\lambda_n \approx 1$ pixel [21], the software filters an image $A(x, y)$ by convolving it with a Gaussian surface of revolution of half-width λ_n:

$$A_{\lambda_n} = \frac{1}{B} \sum_{i,j=-w}^{w} A(x+i, y+j) \exp\left(-\frac{i^2+j^2}{4\lambda_n^2}\right), \tag{3.16}$$

with normalization $B = \left[\sum_{i=-w}^{w} \exp\left(-\frac{i^2}{4\lambda_n^2}\right)\right]^2$. w is an integer larger than a single sphere's apparent radius in pixels, but smaller than the intersphere separation. This calculation strongly suppresses noise without unduly blurring the image. The difference between the noise-reduced and background images is an estimate of the ideal image.

The positions of the microspheres in each image were located by identifying the local brightness maxima. A pixel (x, y) is considered to be the center of a particle if no other pixel within w pixels is brighter. To discriminate true particles from noise, only the brightest particles are considered. All potential particles below a pre-set brightness cutoff were not accepted. The program allows one to set optional parameters, such as eccentricity and particle size, which may be used to further discriminate true particles from noise or other false identifications.

The final step is to link the particle positions in each image with corresponding particles in the later images to produce trajectories. This was done by seeking the most probable correspondence in two consecutive images. If the particles are indistinguishable, this is only

possible by proximity.

Defining δ as the distance that a Brownian particle moves between frames, the most likely assignment of particle labels from one image to the next is the one which minimizes $\sum_{i=1}^{N} \delta_i$, where N is the number of identified particles in the image. The process of each label assignment can be thought of as drawing a bond between a pair of particles in consecutive frames. To simply the calculation, only those bonds shorter than a length scale L are selected as possible candidates for the assignment of particle labels between two frames. L is chosen to be slightly higher than the maximum absolute displacement of the particles between frames.

This linking process is feasible only if the single particle displacement δ in one time step is sufficiently smaller than the typical interparticle spacing a. Otherwise, particle positions will become confused between snapshots. The optimal cutoff parameter L falls in the range $\delta < L < a/2$ [21].

BIBLIOGRAPHY

[1] C. M. Hassan and N. A. Peppas, Adv. Polym. Sci. **153**, 37 (1999).

[2] R. K. Tubbs, J. Polym. Sci. A **4**, 623 (1966).

[3] L. E. Millon, H. Mohammadi, and W. K. Wan, J. Biomed. Mater. Res. B **79**, 305 (2006).

[4] S. D. Hudson, J. L. Hutter, M.-P. Nieh, J. Pencer, L. E. Millon, and W. K. Wan, J. Chem. Phys. **130**, 034903 (2009).

[5] L. E. Millon, M.-P. Nieh, J. L. Hutter, and W. K. Wan, Macromolecules **40**, 3655 (2007).

[6] T. Noguchi, T. Yamamuro, M. Oka, P. Kumar, Y. Kotoura. S. H. Hyon, and Y. Ikada, Appl. Biomater. **2**, 101 (1991).

[7] M. Oka, T. Naguchi, P. Kumar, K. Ikeuchi, T. Yamamuro, S. H. Hyon and Y. Ikada, Clin. Mater. **6**, 361 (1990).

[8] S. H. Hyon, W. I. Cha, Y. Ikada, M. Kita, Y. Ogura, and Y. Honda, J. Biomater. Sci. Polyer. Edn. **5**, 397 (1994).

[9] K. Tsutsumi, K Takayama, Y. Machida, C. D. Ebert, I. Nakatomi, and T. Nagai, S.T.P. Pharama. Sci. **4**, 230 (1994).

[10] H. Purss, G. Qiao, and D. Solomon, J. Appl. Polym. Sci. **96**, 780 (2005).

[11] H. Qian, L. Luo, J. Gong, S. Yu, T. Li, and L. Fei, Cryst. Growth Des. **6**, 607 (2006).

[12] B. Wang, S. Mukataka, E. Kokufuta, and M. Kodama, Radiat. Phys. Chem. **59**, 91 (2000).

[13] E. Oral, H. Bodugoz-Senturk, C. Macias, and O. K. Muratoglu, Nucl. Instrum. Meth. B **265**, 92 (2007).

[14] C. M. Hassan and N. A. Peppas, Adv. Polym. Sci. **153**, 37 (2000).

[15] H. Bodugoz-Senturk, J. Choi, E. Oral, J. H. Kung, C. E. Maciasa, G. Braithwaitec, and O. K. Muratoglua, Biomaterials **29**, 141 (2008).

[16] G. Guhados, W. K. Wan, and J. L. Hutter, Langmuir **21**, 6642 (2005).

[17] J. L. Hutter, J. Chen, W. K. Wan, S. Uniyal, M. Leabu, and B. M. C. Chan, J. Microsc. **219**, 61 (2005).

[18] F. A. Morrison, *Understanding Rheology* (Oxford University Press, New York, 2001).

[19] R. B. Bird, R. C. Armstrong, and O. Hassager, *Dynamics of Polymer Liquids, vol. 1: Fluid Mechanics* (John Wiley & Sons, New York 1987).

[20] M. L. Gardel, M. T. Valentine, and D. A. Weitz, *Microscale Diagnostic Techniques* (Springer, New York, 2005).

[21] J. C. Crocker and D. G. Grier, J. Coll. Interf. Sci. **179**, 298 (1996).

[22] http://www.physics.emory.edu/∼weeks/idl/index.html.

[23] http://www.rsinc.com/idl.

Chapter 4

Frequency-Dependent Viscoelasticity Measurement by Atomic Force Microscopy

4.1 Introduction

When subjected to small deformations, solids store energy and provide a spring-like elastic response, while liquids dissipate energy through viscous flow. More complex materials display viscoelasticity, a combination of solid and fluid-like responses which generally depends on the time scale over which the sample is probed. One way to determine viscoelastic properties is to measure the shear modulus as a function of frequency by applying a small amplitude oscillatory shear strain and measuring the resultant shear stress. This kind of experiment typically requires milliliter sample volumes and only provides information on the bulk response of the material. This method does not allow local measurement in inhomogeneous systems, and samples with lower dimensionality, such as films, nanofibers and nanoparticles cannot be probed directly.

The atomic force microscope (AFM) has been widely used to study the structure of soft and biological materials with sub-nanometer resolution [1, 2, 3, 4]. In addition to imaging, the AFM is increasingly used to measure the local elasticity and viscoelasticity of soft samples, including bone marrow [5], gelatine [6, 7], polyacrylamide gels [8], platelets and living cells

[8, 9]. The advantage of AFM measurements is that topographic images can be obtained simultaneously with the mechanical response, allowing elasticity to be correlated with local structure.

During an AFM experiment, a probe attached to a weak cantilever spring is brought into contact with the sample and the cantilever deflection is monitored as the sample is scanned laterally. In constant-force mode, the cantilever deflection is kept constant by a feedback circuit that adjusts the height of a piezoelectric scanner, on which the sample is mounted, in response to the local topography. The loading force applied to the surface of the sample can be calculated from the deflection of the cantilever and Hooke's law. A soft material will deform in response to the cantilever force, providing an opportunity to measure its mechanical properties. One common technique involves indenting the sample by translating it through a vertical ramp. The discrepancy between the known vertical displacement and resulting cantilever deflection can be used to infer the elastic properties of the sample. We refer to this as the force-curve technique; when this technique is applied over a grid of sample positions, we call it the force-volume technique [10]. However, the effects of non-vertical motion due to sliding of the inclined cantilever along the sample surface (e.g., shear deformation and frictional effects) as well as surface adhesion can complicate the analysis. Cuenot et al. used a resonant contact AFM technique to measure the elastic modulus of nanotubes with a small-amplitude vertical motion, allowing shear to be neglected [11]. Kos and Hurley improved the contact-resonance method by designing electronics to accurately track the resonant frequency [12]. While these methods allow measurement of the elastic modulus of the sample, they do not provide information about the viscous response. Fretigny et al. determined the complex modulus of styrene-butadiene films by modeling the longitudinal displacement of the tip on samples in the static friction regime [13]. AFM measurements using intermittent contact mode or force modulation mode, both of which image surfaces with a cantilever oscillating at a fixed frequency, can reveal contrast in the viscoelastic properties of the sample, but their nonlinear behavior complicates the analysis [14, 15]. Krotil et al. modulated a low frequency sinusoidal signal with a high frequency oscillation to simultaneously measure the topography,

the adhesion forces, applied normal forces and elastic properties of a heterogeneous polymer surface [16]. Sahin et al. recently designed torsional cantilever tips that allow detailed mechanical properties to be measured during intermittent contact imaging [17].

Measurement of viscoelastic properties requires that forces vary on time scales shorter than the duration of the vertical ramps used in the force-volume technique, which are usually applied at a rate of at most several Hz. Mahaffy et al. superimposed an external oscillation at frequencies of 50–300 Hz on a much slower vertical ramp of the AFM scanner and extended the Hertz model for a spherical tip in contact with a flat surface to include a frequency-dependent complex modulus E^*. They applied this approach to polymer gels and biological cells [8].

In this paper, we describe a new AFM technique for investigating frequency-dependent viscoelastic properties, which we demonstrate on poly (vinyl alcohol) (PVA) nanofibers and hydrogels. A small oscillatory voltage with an amplitude of approximately 0.1 V was added to the feedback loop of the AFM during contact mode operation and images were generated according to the resultant motion of the sample. The frequency-dependent viscoelastic modulus can be determined by analyzing the amplitude and phase of this motion relative to the external oscillation. This technique differs from that of Mahaffy et al. in that their oscillation was added to the sample stage during force ramps whereas ours is added to the AFM's feedback loop during contact mode imaging. The validity of this method was verified by comparing the results with those from traditional static methods. The main advantages of this method are that the mechanical measurements can be done in an imaging mode, rather than extracted by post-processing of force-volume data, and that the position and frequency dependence of the viscoelasticity can be easily measured. Moveover, this method can be easily and inexpensively retrofitted to existing AFM equipment.

4.2 Materials and Methods

4.2.1 Sample Preparation

The PVA fibers studied in this work were made by an electrospinning technique described previously [18]. PVA with a molecular weight of 89,000–98,000 g/mol (99+% hydrolyzed) was purchased as a powder from Sigma–Aldrich Co. An electrospinning solution consisting of 8.5 wt% PVA in a solvent of 80% distilled water and 20% ethanol was used. A randomly oriented non-woven fabric of nanofibers was produced by a horizontal electrospinning setup with an aluminum collector stage under a 1.5 kV/cm electric field, a distance of 15 cm to the target, and a 0.2 ml/h solution-feeding rate. Details have been published elsewhere [19]. The length and diameter of the fibers were characterized by imaging with a Leo 1530 (LEO Electron Microscopy Ltd.) scanning electron microscope.

PVA hydrogels were produced by cyclic freezing and thawing of an aqueous PVA solution [20]. The same PVA powder as above was dissolved to a concentration of 12 wt% in milli-Q water at a temperature of 90 °C under reflux and stirred for 3 h. After cooling, the solution was used to fill aluminum molds 8 cm square by 0.5 mm thick. The molds were sealed and immersed in a temperature controlled bath which contained a 50% mixture of ethylene glycol in water. The PVA in the molds was subjected to up to 6 thermal cycles, each of which involved cooling from 20 °C to −20 °C at a rate of 0.12 °C/min, staying at − 20 °C for 2 h, then warming to 20 °C at 0.12 °C/min. Hydrogel films were removed from the molds, cut into small pieces, and stored in distilled water until required for the AFM measurements.

4.2.2 Atomic Force Microscopy

A Multimode atomic force microscope with a Nanoscope IIIa controller (Veeco Instruments) was used for all AFM measurements. The PVA fibers were imaged in air, while the hydrogels were imaged in water using a fluid cell (Veeco Instruments). Si_3N_4 cantilevers with nominal

spring constants of 0.32 N/m (NP-S cantilever C, Veeco Instruments) were used for fiber imaging and cantilevers with spring constants of 0.12 N/m (NP-S cantilever B) were used for hydrogel experiments. An 8 μm diameter polystyrene microsphere was glued under the tip of the cantilever for hydrogel imaging in order to make a spherical contact with the sample surface. The force constants of the cantilevers were calibrated using the thermal noise method [21].

As described below, we modified the AFM feedback loop by adding a small sinusoidal voltage to the vertical deflection signal of the AFM. A digital lock-in amplifier implemented in LabView (National Instruments) was used to detect the amplitude and phase of the oscillation of the cantilever deflection relative to the external oscillation. The output of the lock-in amplifier was input back to the AFM through a signal access monitor to generate images simultaneous with the usual topographical image.

4.2.3 Oscillatory Method

The AFM used senses cantilever deflection with a four-quadrant photodetector that detects the position of a laser beam reflected from the cantilever, producing a signal termed V_{A-B}. In contact mode, the AFM feedback electronics causes a piezoelectric scanner to move the sample vertically so as to maintain V_{A-B} at a constant setpoint value V_s. We modified the AFM feedback loop to add a small oscillatory voltage of angular frequency ω and amplitude q to the deflection signal as shown schematically in Fig. 4.1. This results in a compensatory vertical oscillation of the sample platform, which in turn causes the cantilever to oscillate while maintaining V_{A-B} constant. The amplitude of the sample platform motion is determined by the added signal, the detector calibration, and the sample properties. For instance, if the sample is perfectly rigid, the amplitude of the cantilever oscillation would be equal to that of the scanner oscillation, and if the gain of the feedback loop is high enough, the two motions would be in phase. For a material with a finite elastic modulus, the oscillation amplitude of the cantilever deflection will be smaller than that of the scanner due to deformation of

the sample surface. If the sample is viscoelastic, the viscous component of its response will cause the cantilever deflection to be out of phase with the motion of the scanner. A voltage signal $z(t)$ proportional to the vertical position of the AFM scanner is available via a signal access monitor; we used a lock-in amplifier implemented using LabView software to measure its amplitude and phase. Below, we model this system using a viscoelastic extension of the standard Hertz theory [8, 22, 23].

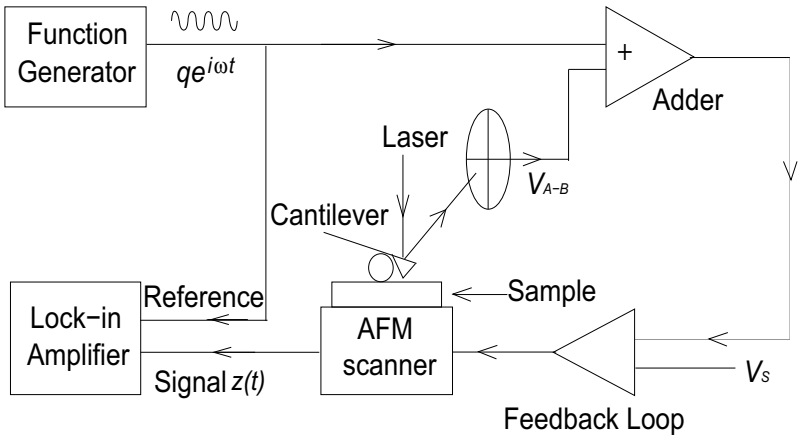

Figure 4.1: Schematic showing the basic operation of the AFM in contact mode, with modifications described in the text. The adder consists of a standard inverting adder followed by a unity-gain inverting amplifier.

In the absence of any added external oscillation, the vertical deflection signal is given by

$$V_{A-B} = V_0 + \frac{y(t)}{S}, \tag{4.1}$$

where V_0 is a constant, $y(t)$ is the deflection of the cantilever and S is the cantilever sensitivity. When the tip is in contact with the sample, $y(t)$ depends on the vertical position of the scanner $z(t)$, the unperturbed sample thickness h_0 and the deformation $\delta(t)$ of the sample due to the AFM tip,

$$y(t) = y_0 + z(t) + h_0 - \delta(t), \tag{4.2}$$

where y_0 is a constant and we have defined $\delta(t)$ to be positive downwards and all other quantities to be positive upwards.

The function of the AFM feedback electronics is to maintain V_{A-B} equal to a given setpoint voltage V_s by adjusting the vertical position $z(t)$ of the scanner. We can thus write

$$V_s = V_0 + \frac{z(t) - \delta(t)}{S}, \tag{4.3}$$

where for simplicity we have defined $y_0 = 0$ and $h_0 = 0$. For Eq. (4.3) to be true at all times, we must have $V_0 = V_s$ and $\delta(t) = z(t)$; in other words, the scanner position simply adjusts to compensate for the deformation of the sample, keeping the cantilever deflection $y(t)$ constant.

If we now add an oscillatory voltage $qe^{i\omega t}$ to V_{A-B}, the feedback attempts to maintain

$$V_s = V_0 + \frac{z(t) - \delta(t)}{S} + qe^{i\omega t} \tag{4.4}$$

constant. From the time dependent terms we get

$$z(t) = \delta(t) - qSe^{i\omega t}, \tag{4.5}$$

showing that the oscillatory motion of the scanner depends on both the externally applied voltage and the deformation of the material surface $\delta(t)$.

We first consider applying this method to a perfectly rigid sample, for which there is no surface deformation. In this case $\delta(t) = 0$, and from Eq. (4.5) the position of the scanner is given by

$$z(t) = qSe^{i(\omega t + \pi)}. \tag{4.6}$$

Here the scanner position oscillates with an amplitude qS and a phase of π relative to the added oscillation.

We now consider a suspended elastic fiber of length L subjected to a downward force F by the AFM tip, as shown in Fig. 4.2. From standard beam deflection theory [24], the

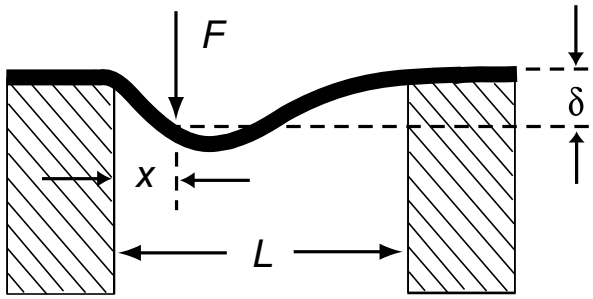

Figure 4.2: Illustration of the deformation of a fiber clamped to supports a distance L apart while subject to a vertical force F applied at a distance x from one end of the fiber.

deformation of the fiber at the location of the tip is given by [10]

$$\delta = \frac{F}{3IE}\left[\frac{x(L-x)}{L}\right]^3 = CF, \tag{4.7}$$

where x is the position along the fiber at which the force is applied, $I = \pi D^4/64$ is the area moment of inertia of a cylindrical fiber of diameter D, E its Young's modulus, and $C = [x(L-x)/L]^3/3IE$ its compliance.

The loading force F exerted by the AFM tip on the fiber is due to the bending of the cantilever. By Hooke's law, we have $F = ky(t)$, where k is the cantilever spring constant and F is downwards. Eq. (4.2) then yields

$$y(t) = z(t) - CF = z(t) - kCy(t). \tag{4.8}$$

Solving for $y(t)$, we find

$$y(t) = \frac{z(t)}{1+Ck}, \tag{4.9}$$

which upon substitution into Eq. (4.5) yields

$$z(t) = qS(1+Ck)e^{i(\omega t+\pi)}. \tag{4.10}$$

Thus for this case the oscillatory response of the scanner has an amplitude $z_0 = qS(1+Ck)$

and a phase of π relative to the added voltage. C depends on the point of application of the force, so the amplitude will vary with position x along the fiber, but the phase will remain constant if viscous effects can be neglected. Since the functional form of C is known, measurements of z_0 as a function of x can be used to determine the Young's modulus E of the fiber.

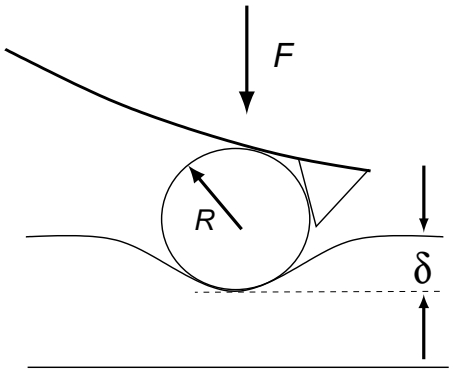

Figure 4.3: Deformation a soft surface depressed by a rigid sphere of radius R, which is glued under an AFM tip. δ is the deformation of the surface as a result of the applied force F.

Finally, we consider the case in which the AFM tip is in contact with a viscoelastic surface. In this case, the compliance of the material is in general a function of the loading force. In our experiments on hydrogel films, we use a spherical probe as shown in Fig. 4.3 and model the deformation of the sample in terms of Hertz theory [22, 23]:

$$F = \frac{4}{3} K R^{1/2} \delta^{3/2} = \alpha \delta^{3/2}. \tag{4.11}$$

Here $K = E/(1-\nu^2)$, ν is the Poisson's ratio of the sample, R is the probe radius, and $\alpha = 4KR^{1/2}/3$. K will in general be complex, reflecting both viscous and elastic contributions to the complex modulus E, and will be a function of frequency ω. In using Eq. (4.11) we have assumed that the spherical probe itself does not deform, and that δ is much smaller than both the sample thickness and the spherical probe radius [8, 22, 25]. These assumptions are well satisfied in our experiments.

To measure the frequency-dependent complex modulus of the material, a small oscillatory force $F_1(t)$ with angular frequency ω can be applied around an average loading force F_0. This leads to an oscillatory deformation of the surface $\delta_1(t)$ about the initial deformation δ_0. Expanding Eq. (4.11) in a Taylor series about δ_0, we get [8, 23]

$$F = F_0 + F_1(t) = \alpha(0)\delta_0^{3/2} + \frac{3}{2}\alpha(\omega)\delta_0^{1/2}\delta_1(t). \tag{4.12}$$

Here $\alpha(0)$ is calculated using $E(0)$, the zero-frequency value of the complex modulus, and $\alpha(\omega)$ using $E(\omega)$ evaluated at the frequency of the oscillating applied force. As above, F is related to the cantilever deflection $y(t)$ by Hooke's law. We write $y(t) = y_0 + y_1(t)$, where y_0 here is the deflection corresponding to the mean deformation δ_0, and substitute $F = ky(t)$ into Eq. (4.12) to obtain a relationship between the deformation and the cantilever deflection,

$$\delta_0 = \left[\frac{ky_0}{\alpha(0)}\right]^{2/3}, \tag{4.13}$$

and

$$\delta_1(t) = \frac{2ky_1(t)}{3\alpha(\omega)\delta_0^{1/2}}. \tag{4.14}$$

Substituting these results into Eq. (4.2) and solving for $y_1(t)$, we find

$$y_1(t) = \left[1 + \frac{2k}{3\alpha(\omega)\delta_0^{1/2}}\right]^{-1} z_1(t), \tag{4.15}$$

where $z_1(t)$ is the time-dependent part of the scanner position $z(t)$. Using Eqs. (4.4) and (4.5), we find

$$z_1(t) = -qS\left[1 + \frac{2k}{3\alpha(\omega)\delta_0^{1/2}}\right] e^{i\omega t} \tag{4.16}$$

$$= \tilde{z}e^{i(\omega t + \pi - \phi)} \tag{4.17}$$

where $\tilde{z}$ is the amplitude of the response and ϕ is the contribution to the phase shift due to the frequency-dependent complex modulus $E(\omega)$.

In practice, it is difficult to measure ϕ accurately because of additional phase shifts that may exist in the electronics and viscous effects due to the cantilever itself as it moves through a viscous medium. We therefore take the ratio ρ of $z_1(t)$ measured for the viscoelastic sample (Eq. (4.17)) to the response measured for a rigid substrate (Eq. (4.6)) with other experimental parameters (cantilever, fluid, etc.) held constant. Any additional phase shifts (e.g., due to the circuit and cables) will be the same for both measurements and so cancel out, so the ratio is

$$\rho = 1 + \frac{2k}{3\alpha(\omega)\delta_0^{1/2}} \tag{4.18}$$

$$= 1 + \frac{k}{2R^{1/2}\left[E(\omega)/(1-\nu^2)\right]\delta_0^{1/2}}. \tag{4.19}$$

Since k and R are constants determined by the experimental apparatus and δ_0 can be calculated from the setpoint and force curves obtained on the sample surface, this approach allows us to determine the value of $K(\omega) = E(\omega)/(1-\nu^2)$ as a function of the frequency of the applied oscillation.

4.2.4 Static Method

The Young's modulus of suspended fibers can be measured with the AFM using the force-volume (FV) technique described in Ref. [10]. Briefly, force curves are obtained by measuring the cantilever deflection resulting from a known vertical ramp of the sample platform at a rate up to several Hz. Since the slope of the force curve when the tip is in contact with the fiber depends on the sample compliance, the Young's modulus of the beam can be determined by modeling the shape of the curve. As discussed above, the loading force on a suspended fiber is $F = ky(t)$, and the deformation due to this force is given by Eq. (4.7). The deflection of the cantilever $y(t) = z(t) - \delta$ becomes

$$y(t) = z(t)\left[1 + \frac{k}{3EI}\left(\frac{x(L-x)}{L}\right)^3\right]^{-1}, \tag{4.20}$$

so the measured slope of the contact portion of the force curve is

$$\frac{dy}{dz} = \left[1 + \frac{k}{3EI}\left(\frac{x(L-x)}{L}\right)^3\right]^{-1}. \tag{4.21}$$

In an AFM experiment, a force-volume image of a region containing the fiber is collected. The theoretical slope is $dy/dz = 1$ for points on the rigid substrate, while the slope along the suspended portion of the fiber will be a function of the distance x from the edge of the substrate. These slopes, normalized by the mean slope on the substrate, are fitted to Eq. (4.21) to determine the Young's modulus of the fiber.

When this technique is applied to a soft film such as a hydrogel, the force curves are not linear. In this case, during the contact portion of a force curve ramp the cantilever deflection is

$$y - y_0 = z - z_c - \delta, \tag{4.22}$$

where z_c is the contact point, y_0 is the initial cantilever deflection and δ is given by Eq. (4.11). Thus

$$z - z_c = \left[\frac{3k(1-\nu^2)}{4ER^{1/2}}\right]^{2/3}(y - y_0)^{2/3} + (y - y_0). \tag{4.23}$$

This is a third-order polynomial equation of the form

$$x^3 + bx^2 + d = 0 \tag{4.24}$$

in the variable $x \equiv (y - y_0)^{1/3}$, with $b = \left[3k(1-\nu^2)/(4ER^{1/2})\right]^{2/3}$ and $d = z_c - z$. If the tip is in contact with the sample surface, d is negative and the deflection $y - y_0$ is positive.

Depending on the sign of the discriminant

$$\Delta = \frac{d^2}{4} + \frac{db^3}{27}, \tag{4.25}$$

the desired solution is

$$x = s_+ + s_- - \frac{b}{3}, \tag{4.26}$$

where

$$s_\pm = \begin{cases} \left[-108d - 8b^3 \pm 12\sqrt{3d(27d+4b^3)}\right]^{1/3}/6 & \text{for } \Delta \geq 0 \\ \frac{b}{3}\cos\frac{\theta}{3} & \text{for } \Delta < 0 \end{cases} \tag{4.27}$$

and $\theta = \arccos(-(27d + 2b^3)/2b^3)$. By fitting the measured values of $y - y_0$ as a function of $z_c - z$ to Eq. (4.26), we can extract the static Young's modulus E.

4.3 Results and Discussion

4.3.1 PVA Nanofibers

We first used our oscillatory technique to measure the Young's modulus of suspended PVA fibers. The PVA fibers were deposited on a TEM grid to suspend them across square holes with 7.5 μm sides. The suspended length and average diameter of the fiber were measured by SEM, and samples were imaged both before and after the experiment to ensure the fiber had not moved during the experiment. Fig. 4.4 shows AFM images of (a) height and (b) oscillation amplitude (measured by the lock-in amplifier) for a fiber of suspended length 2.79 μm and diameter 124 nm. In this example, the frequency of the sinusoidal voltage added to the AFM feedback was 500 Hz. The phase of the fiber oscillation was constant during imaging, as expected from Eq. (4.10) for a purely elastic fiber. Thus viscous effects are negligible, so we studied the elastic modulus of the fiber by analyzing the amplitude of the response.

The oscillation amplitude image of Fig. 4.4(b) shows a complicated structure. The amplitude on the supported portion of the fiber is the same as that on the bare substrate, where there is no fiber, as expected. Far from the suspended portion of the fiber (lower left corner) the sample lies beyond the vertical range of the scanner, resulting in no signal. In regions near the suspended fiber or the edge of the pit, it is possible for the side of the tip, a square pyramid 4 μm across at the base, rather than its apex, to contact the sample. This results in poor tracking and noisy features. Such effects were seen in the height image as well, but the gray-scale in Fig. 4.4(a) was chosen to avoid these features for clarity. Moreover, contact with the side of the tip produces deflection forces in significantly different directions from the vertical direction assumed by our model; thus, these regions are of no use for our analysis. The lines in Fig. 4.4(b) indicate a range of locations near the midline of the fiber, where our model can be applied. It can be seen that the amplitude is larger in the middle of the suspended part of the fiber, as expected from Eqs. (4.7) and (4.10).

If the gain of the AFM feedback loop is not high enough, the scanner will not be able to keep up with the external oscillation, leading to an apparent value of the Young's modulus larger than the true value. We performed measurements with a range of gain settings to verify that the gain we used was high enough that the amplitude of the response of the rigid substrate was independent of the gain. This is much the same as the way in which gain settings are chosen in conventional contact imaging to ensure that the specific settings used do not influence the height information.

To extract the Young's modulus E, we fit the oscillation amplitude z_0 from all pixels within the range shown in Fig. 4.4(b) to the model, Eq. (4.10). The results are shown in Fig. 4.5. The range covered by the fit line corresponds to the suspended length of the fiber. The value of E obtained from the fit is 4.37 ± 0.06 GPa, where the uncertainty reflects the statistical uncertainty in the fit. The uncertainty in the cantilever spring constant is not included, since it introduces a systematic effect which is the same for all measurements made with the same cantilever.

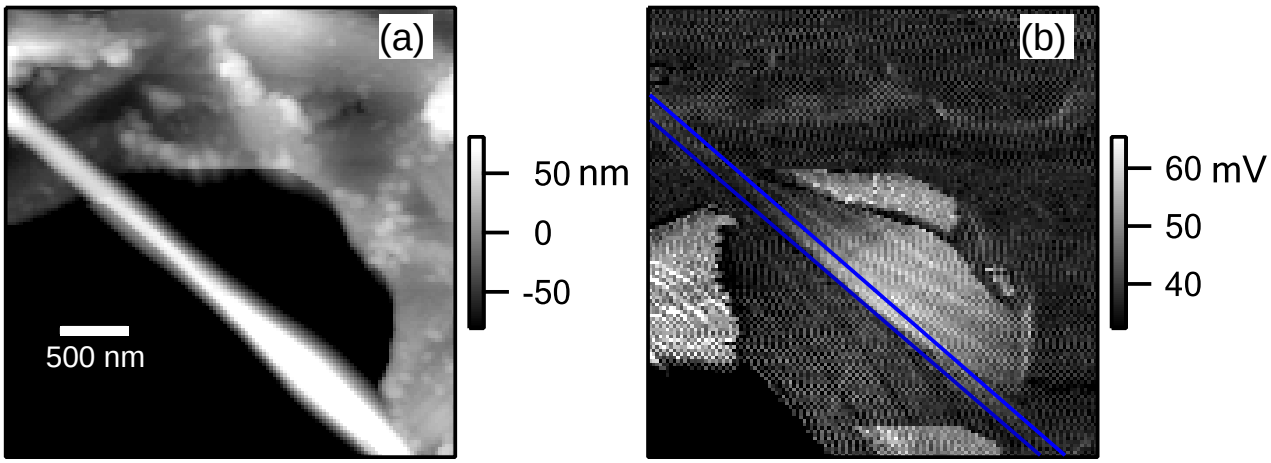

Figure 4.4: AFM images for a suspended fiber: (a) height image; (b) oscillation amplitude image. The fiber had a suspended length of 2.79 μm and a diameter of 124 nm. The lines in (b) indicate the range over which the data were analyzed.

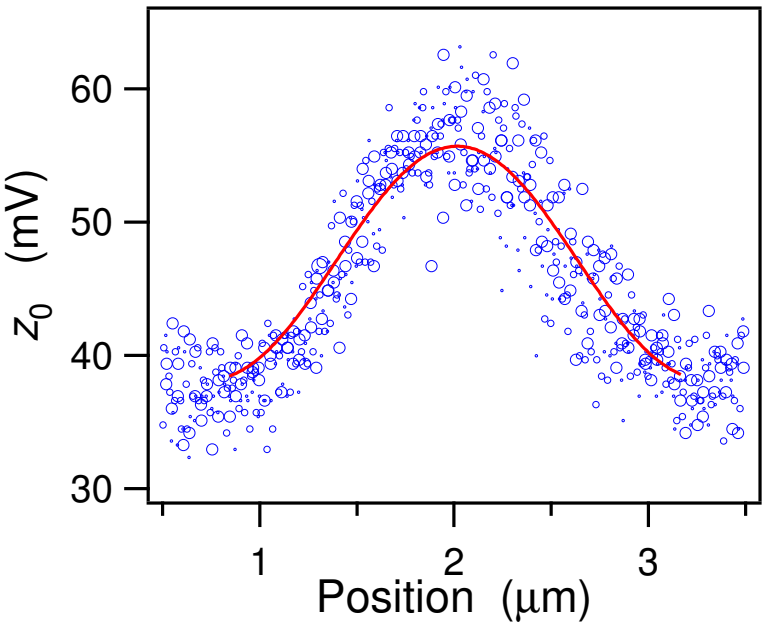

Figure 4.5: Oscillation amplitude z_0 (circles) as a function of position along the suspended fiber shown in Fig. 4.4. The sizes of the circles indicate the distance from the midline of the fitting range for each point: the larger the size, the closer to the midline. The solid curve is a fit to Eq. (4.10).

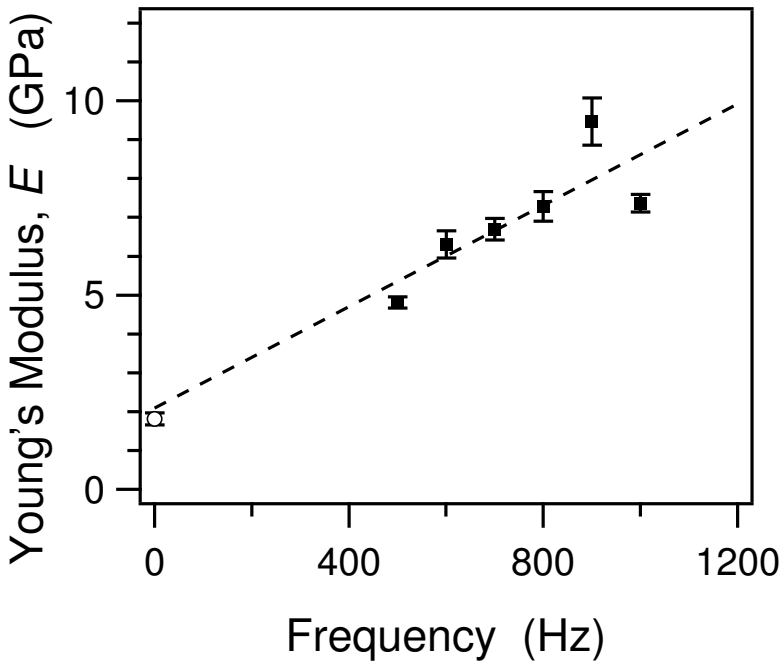

Figure 4.6: Young's modulus of a PVA fiber as a function of frequency. Solid squares: Young's modulus determined by the oscillatory method. Open circle: the low-frequency Young's modulus of the same fiber measured by the force-volume technique. The dashed line is a fit to the oscillatory data only.

We measured the Young's modulus of a PVA fiber as a function of frequency from 500 to 1000 Hz, where the maximum frequency is determined by the finite bandwidth of our modified electronics and the minimum is limited by the time required for the measurements. The time constant of the lock-in amplifier was set at 10 times the oscillation period and so was between 10 ms and 20 ms. Since the dwell time of the AFM was about 78 ms/pixel, this was long enough to give a stable response at each pixel of the AFM image. Fig. 4.6 shows the results for this fiber, which had a suspended length of 4.15 μm and diameter of 179 nm. It is seen that the modulus increases by a factor of two over the frequency range studied, highlighting the importance of frequency-dependent measurements.

We also performed force-volume measurements to determine the zero-frequency Young's modulus of the same fibers for comparison with our new method. The relative slope as a function of position for the fiber shown in Fig. 4.4 is plotted in Fig. 4.7(a). In this case the data split into two series, one above and one below the fitted curve. This is because the diameter of the fiber is small compared to the size of the tip. As a result, very few force curves are measured precisely on the midline of the fiber. Instead, many of the points in the FV data represent contact between the fiber and the sides of the pyramidal tip, resulting in off-center loading. In order to demonstrate this, Fig. 4.7(a) labels all points acquired above the midline of the fiber as circles, and those acquired below the fibers as crosses. The nearly perfect division of points verifies the dependence on the precise position of the measurement relative to the fiber.

The origin of the different slopes is easily understood: For instance, if the fiber contacts the side of the tip furthest from the cantilever base, as is the case for points measured above the fiber in Fig. 4.4, it gives rise to a torque that decreases the cantilever deflection from that which would occur for a purely vertical contact force. For the same reason, a larger vertical oscillation is needed to compensate for the added signal in the oscillatory method, explaining the fact that amplitudes measured above the fiber are higher than those measured below in Fig. 4.4(b).

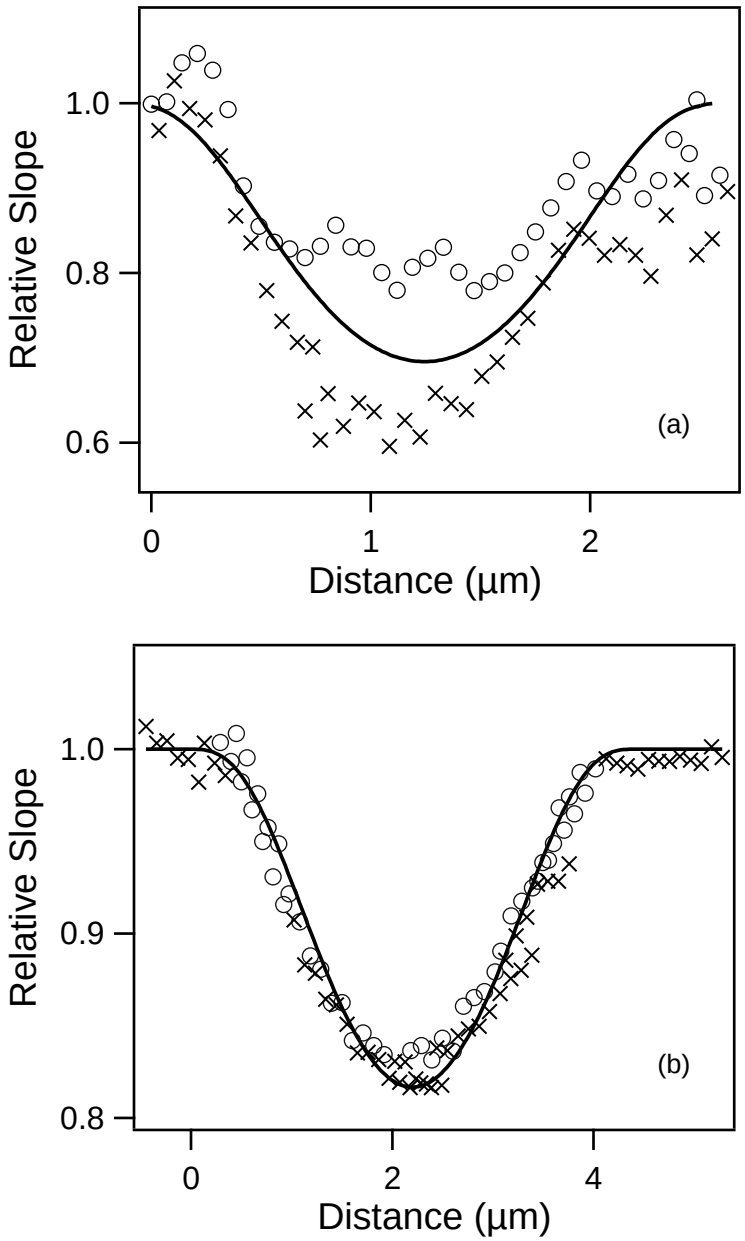

Figure 4.7: Relative slope as a function of distance along suspended fibers for (a) the fiber as shown in Fig. 4.4, and (b) a different fiber in which data more closely follow a single curve. The two series are points from above (circles) and below (crosses) the fibers, relative to their height images. The lines are fits of the relative slopes to Eq. (4.21).

Fig. 4.7(b) shows the relative slopes for a different PVA fiber with length 3.70 μm and diameter 114 nm. In this case a much smaller splitting is seen, presumably because the data were taken closer to the midline. Effects of the tip position are evident in the oscillatory method as well, but the higher pixel density always results in a scatter of points similar to that seen in Fig. 4.5, providing a realistic assessment of the uncertainties inherent in this technique. The value of the Young's modulus obtained by fitting the data in Fig. 4.7(a) is 4.6 $\pm$ 0.3 GPa. The quoted uncertainty again does not include the uncertainty in the cantilever calibration or in the fiber dimensions, since the same cantilever and fiber were used for both oscillatory and static measurements. For the fiber tested in Fig. 4.6, the zero-frequency Young's modulus (open circle in Fig. 4.6) was 1.8 $\pm$ 0.2 GPa, in agreement with the linear extrapolation of the oscillatory data to an intercept of 2.1 $\pm$ 1.8 GPa.

To test the reproducibility of the oscillatory technique, we measured the Young's modulus of nine fibers at a frequency of 500 Hz and compared these values to those obtained by the FV method for the same fibers. Since the Young's modulus varies between fibers, we examined the ratio between the values determined from the two techniques, which we found to be 1.37 $\pm$ 0.16. This agrees with our finding that the Young's modulus increases with frequency, while the magnitude of the uncertainty provides a measure of the consistency of the technique.

4.3.2 PVA Hydrogels

We also used the oscillatory technique to measure the viscoelastic properties of PVA hydrogels. PVA hydrogels of thickness 0.5 mm were attached to silicon plates using cyanoacrylate glue. AFM measurements were made in a fluid cell with a glass cantilever holder. As above, oscillatory experiments were performed in contact mode with a small sinusoidal voltage added to the feedback loop of the AFM. In order to simplify the data analysis, each measurement was done at a single point on the surface of the sample by setting the imaging size to zero. We performed measurements at three different locations on each sample. Fig. 4.8 shows how

the mean deformation δ_0 was determined. The hydrogel sample was mounted on a rigid silicon plate and force curves were recorded on the hydrogel and on a base portion of the silicon plate. The difference in $z - z_c$ between the two force curves at the setpoint V_s is equal to the deformation δ_0. The exact value of V_s is unimportant as long as the deflection of the cantilever remains in the linear regime. For the force curve in Fig. 4.8, V_s is about 1.65 V and δ_0 is about 95 nm. The force constant of the cantilever here is 0.093 N/m and its sensitivity is about 47 nm/V.

Fig. 4.9 summarizes the results of measurements made at 50 Hz on hydrogels prepared with different numbers of thermal cycles. The moduli were found to vary from point to point on a given sample by substantially more than the experimental uncertainties, confirming earlier reports that the PVA hydrogel surface is nonuniform [20]. The linear fit indicates that although there is a wide variability, the average modulus increases with the number of cycles.

Fig. 4.10 shows the dependence on frequency of the complex modulus of a PVA hydrogel subjected to four thermal cycles during preparation. The magnitude of the modulus increases with frequency from a low-frequency value of about 55 kPa, which is consistent with bulk results reported elsewhere [20]. The storage modulus E', the real part of the complex modulus, dominates the mechanical response at low frequency while the loss modulus E'', the imaginary part, dominates at high frequency. We interpret this as an indication that viscous effects due to motion of the polymer chains in the fluid within the hydrogel become increasingly important as the frequency increases. Note that the main source of uncertainty in the moduli comes from the determination of the mean deformation δ_0. In our instrument, variation in the deflection signal due to, for example, mechanical creep or electrical drift can result in uncertainties of up to 5% in δ_0.

We also compared the magnitude of the complex modulus of the PVA hydrogels to the Young's modulus measured by fitting the force curves to Eq. (4.23). Since the viscoelastic properties of the hydrogels vary across the sample, force curves were measured before and after each oscillatory measurement, at the same location on the hydrogel sample and with

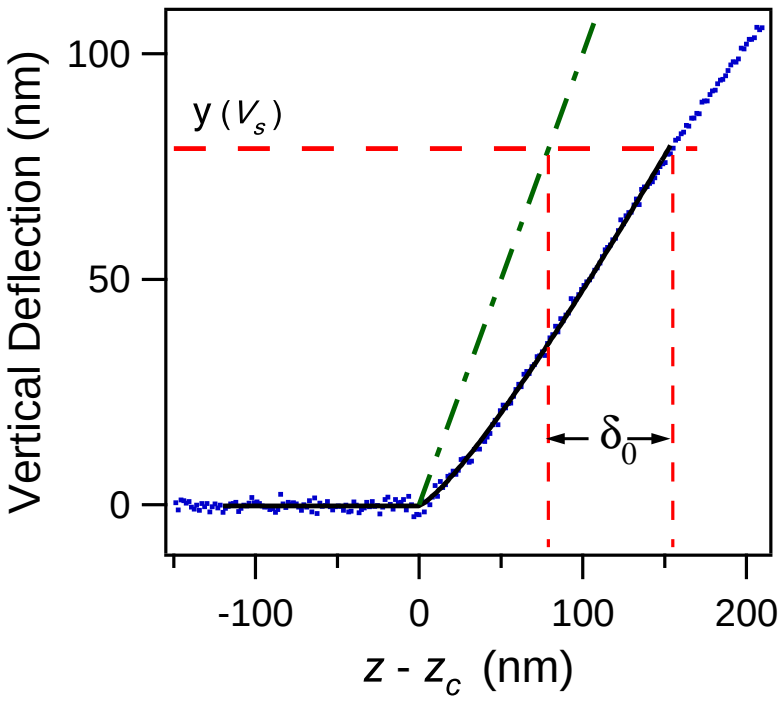

Figure 4.8: Force curve used to determine δ_0 for the oscillatory method. Dots: Measured force curve for a 4-cycle PVA hydrogel. Dot-dashed line: Theoretical force curve on a silicon plate. Solid line: a fit to Eq. (4.23) used to determine the static Young's modulus of the PVA hydrogel.

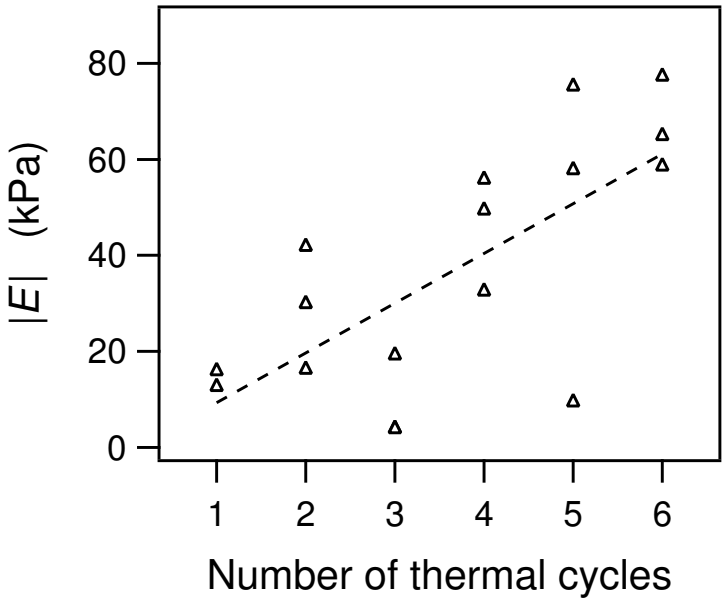

Figure 4.9: Magnitude of the complex modulus measured by the oscillatory technique at 50 Hz for PVA hydrogels subjected to a varying number of thermal cycles during preparation. $|E|$ was measured at three locations on each of six samples. The dashed line is a linear fit to the data points as a function of the number of thermal cycles.

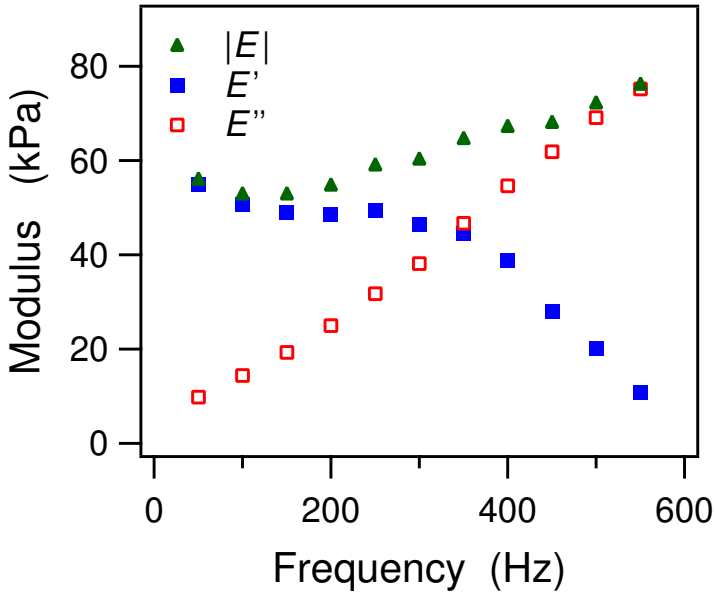

Figure 4.10: Complex modulus of a PVA hydrogel (four thermal cycles) as a function of frequency. E' is the storage modulus (real part); E'' is the loss modulus (imaginary part); $|E| = (E'^2 + E''^2)^{\frac{1}{2}}$ is the magnitude of the complex modulus.

the same experimental parameters, to allow for a meaningful comparison. One example is shown in Fig. 4.8, for which the fit indicates a Young's modulus of 71$\pm$1 kPa, which is within the range of $|E|$ determined by the oscillatory method for the four-cycle hydrogel (see Fig. 4.10). Fig. 4.11 compares the moduli of hydrogel samples measured from the force curves at a 1 Hz ramp rate with those measured by the oscillatory technique at 50 Hz. The data points are taken from various locations on each of the hydrogel samples. The ratio of the modulus obtained from the oscillatory technique to that from the static technique is 1.14 $\pm$ 0.08, indicating that, on average, the modulus at 50 Hz is slightly larger than that at 0 Hz.

4.4 Conclusion

We have developed a new technique for measuring the viscoelastic response of soft materials using atomic force microscopy. This technique was implemented by using an external circuit

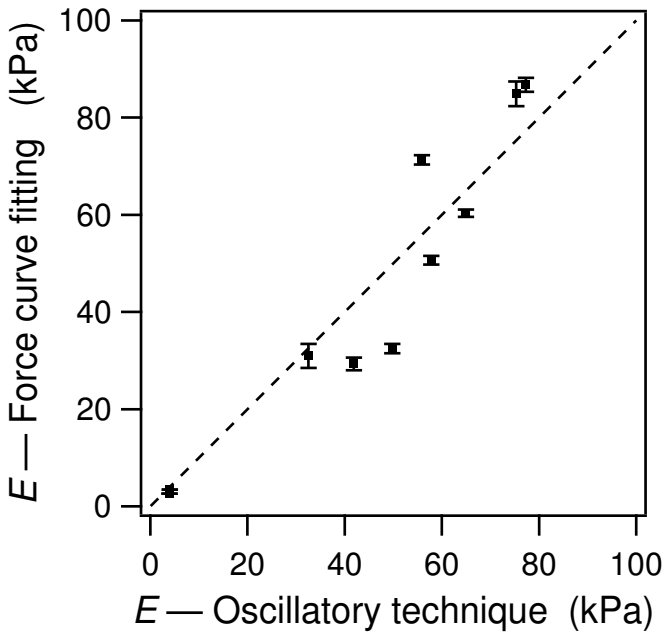

Figure 4.11: Comparison of moduli determined by static force curve fitting technique and the oscillatory technique at 50 Hz. The dashed line corresponds to equality of the values determined from the two techniques.

to add an oscillatory voltage to the feedback loop of the AFM. The response was measured using a lock-in amplifier and viewed as an image alongside the usual AFM topography image. The main advantages of this technique over conventional AFM-based techniques for measuring mechanical properties are that it can be done in imaging mode, simplifying the set-up and analysis, and the excitation frequency can be easily varied, allowing viscoelastic properties to be determined as a function of frequency. The validity of this method was confirmed by comparing results for electrospun PVA nanofibers and physically cross-linked PVA hydrogels with those measured by the static techniques. The Young's modulus of the nanofibers increased linearly with frequency; extrapolating the data to zero frequency gave a static Young's modulus in good agreement with that measured with the FV method. This shows that static measurements are not sufficient to describe the mechanical properties of PVA nanofibers. Viscoelastic effects were evident in the PVA hydrogels. Our results for the frequency dependence of the complex modulus show that the storage modulus dominates the viscoelastic response of these materials at low frequency, while the loss modulus dominates at high frequency.

BIBLIOGRAPHY

[1] B. Drake, C. B. Prater, A. L. Weisenhorn, S. A. C. Gould, T. R. Albrecht, C. F. Quate, D. S. Channell, H. G. Hansma, and P. K. Hansma, Science **243**, 1586(1989).

[2] E. Henderson, P. G. Haydon, and D. S. Sakaguchi, Science **257**, 1944 (1992).

[3] R. M. Henderson and H. OberleithnerPushing, Am. J. Physiol. Renal Physiol. **278**, 689 (2000).

[4] S. Kasas, N. H. Thomson, B. L. Smith, P. K. Hansma, J. Mikossy, and H. G. Hansma, Int. J. Img. Sys. Tech. **8**, 151 (1997).

[5] N. J. Tao, S. M. Lindsay, and S. Lees, Biophys. J. **63**, 1165 (1992).

[6] M. Radmacher, M. Fritz, and P. K. Hansma, Biophys. J. **69**, 264 (1995).

[7] J. Domke and M. Radmacher, Langmuir **14**, 3320 (1998).

[8] R. E. Mahaffy, C. K. Shih, F. C. MacKintosh, and J. Käs, Phys. Rev. Lett. **85**, 880 (2000).

[9] M. Radmacher, M. Fritz, C. M. Kacher, J. P. Cleveland, and P. K. Hansma, Biophys. J. **70**, 556 (1996).

[10] G. Guhados, W. K. Wan, and J. L. Hutter, Langmuir **21**, 6642 (2005).

[11] S. Cuenot, C. Frétigny, S. Dmeoustier-Champagne, and B. Nysten, J. Appl. Phys. **93**, 5650 (2003).

[12] A. B. Kos and D. C. Hurley, Meas. Sci. Technol. **19**, 015504 (2008).

[13] C. Fretigny, C. Basire, and V. Granier, J. Appl. Phys. **82**, 43 (1997).

[14] L. Nony L, R. Boisgard, and J. P. Aimé, J. Chem. Phys. **111**, 1615 (1999).

[15] S. L. Lee, S. W. Howell, A. Raman, and R. Reifenberger, Phys. Rev. B **66**, 115409 (2002).

[16] H. U, Krotil, T. Stifter, and O. Marti, Rev. Sci. Instrum. **71**, 2765 (2000).

[17] O. Sahin, S. Magonov, C. Su, C. F. Quate, and O. Slogaard, Nat. Nanotechnol. **2**, 507 (2007).

[18] A. Frenot and I. S. Chronakis, Curr. Opin. Colloid Interface Sci. **8**, 64 (2003).

[19] K. H. Wong, M. Zinke-Allmang, and W. K. Wan, Nucl. Instrum. Methods Phys. Res. B **249**, 362 (2006).

[20] L. E. Millon, M. P. Nieh, J. L. Hutter, and W. K. Wan, Macromolecules **40**, 3655 (2007).

[21] J. L. Hutter and J. Bechhoefer, Rev. Sci. Instrum. **64**, 1868 (1993).

[22] I. N. Sneddon, Int. J. Eng. Sci. **3**, 47 (1965).

[23] K. L. Johnson, K. Kendall, and A. D. Roberts, Proc. R. Soc. Lond. A. **324**, 301 (1971).

[24] J. M. Gere and S. P. Timoshenko, *Mechanics of Materials* (PWS Publishing, Boston, 1997).

[25] R. E. Mahaffy, S. Park, and E. Gerde, J. Käs, and C. K. Shih, Biophys. J. **86**, 1777 (2004).

Chapter 5

Rheology and Structure of Poly(vinyl alcohol)-Poly(ethylene glycol) Blends during Aging

5.1 Introduction

Polymer gels and networks have attracted much attention in recent years because of their enormous potential as biomaterials [1, 2, 3, 4, 5, 6]. Of these, physical gels based on poly(vinyl alcohol) (PVA) are among the most interesting due to their biocompatibility and nonlinear mechanical properties. These materials have biomedical and pharmaceutical applications as artificial tissues, contact lenses and drug delivery reservoirs [4, 5, 6, 7].

In a physical gel, polymer chains are interconnected by physical crosslinks such as microcrystalline junctions or weak associative bonds [8, 9, 10, 11]. These are typically much weaker than the bonds in a chemically-crosslinked gel, so most physical gels are thermoreversible while chemical gels are not [1]. Gelation occurs when the crosslinks create a percolation network that spans the system [1, 12, 13]. PVA has an upper critical solution temperature and phase separates when quenched into the unstable region of the phase diagram. Consequently, gelation can take place in combination with microphase separation [14, 15, 16, 17]. The physical properties of PVA gels are related to the microstructure that develops during

gelation. For example, PVA gels with high elasticity made from dimethyl sulfoxide (DMSO)-water solutions are transparent, possibly because the gelation rate is much faster than the phase separation [18], while the occurrence of phase separation before gelation in aqueous PVA solutions results in opaque gels [19].

The gelation of PVA in various solvents has been widely studied, but different authors have reached different conclusions [14, 15, 16, 17, 20, 21]. Kanaya *et al.* studied the structural evolution of PVA in DMSO using light scattering and small angle neutron scattering [14, 15]. They found that phase separation by spinodal decomposition occurs before gelation of the PVA. On the other hand, Takahashi *et al.* recently suggested that gelation occurs first and induces phase separation in solutions of PVA in DMSO and water [16].

Polymer solutions and gels are viscoelastic materials which both store and dissipate energy when subjected to an externally applied stress [22, 23]. Rheological measurements can characterize their mechanical properties and provide information about their microstructure [12, 13, 23]. For example, the material's response to an applied oscillatory strain or stress with an angular frequency ω can be used to identify the gel transition [12, 13]. In the fluid phase, $G''(\omega) > G'(\omega)$, and $G'(\omega) \to 0$ while $G''(\omega)/\omega$ approaches a constant as $\omega \to 0$. In the gel phase, $G''(\omega) < G'(\omega)$, and $G'(\omega)$ is constant while $G''(\omega)/\omega \to \infty$ as $\omega \to 0$. At the gel point, the loss modulus $G''(\omega)$ and the storage modulus $G'(\omega)$ both show the same power law dependence on frequency, with $G'(\omega) \approx G''(\omega) \propto \omega^{\nu}$. The gel transition can therefore be studied by monitoring a system's viscoelastic properties [12, 24]. Rheological data on PVA solutions have been reported as a function of concentration, molecular weight, temperature and degree of saponification [24, 25, 26, 27, 28]. Lyoo *et al.* found that PVA molecules in high concentration solutions or with high molecular weight were easily oriented by shear [25, 26]. Lee *et al.* [27] found that solutions of PVA in DMSO were rheologically heterogeneous, although they were optically transparent. They also found that gelation of PVA was dramatically affected by shear rate [28] and that the behavior near the gel transition depended on tacticity (the degree to which hydroxyl groups along the polymer chain are ordered) and concentration [24].

Dynamic light scattering can be used to investigate the mobility of macromolecules in solution [29], as well as structure and dynamics at the sol-gel transition [3, 17, 30, 31, 32, 33]. Shibayama *et al.* proposed four features that should be observed in a dynamic light scattering measurement at the gel point [35, 36]: a large increase in scattering intensity, power-law behavior of the intensity autocorrelation function, a characteristic broadening in the distribution of relaxation times, or a depression of the initial amplitude of the intensity autocorrelation function. Although these features have been confirmed for many chemical and physical gels [32], it is not clear whether the "microscopic" gel-point determined by these methods is the same as the "macroscopic" gel point determined by rheological methods. Matsunaga *et al.* reported good agreement between the microscopic and macroscopic gel points of gelatin hydrogels [32], while Oppong *et al.* observed that gelation of Laponite clay suspensions occured earlier on the macroscopic scale than on the microscopic scale [12].

In the present work, we use rheological and dynamic light scattering techniques to study the formation of physically cross-linked PVA gels made by the theta-gel method [37], in which poly(ethylene glycol) (PEG) is added to the PVA solutions as a gelling agent. These blends undergo gelation as they age. We study PVA/PEG blends consisting of 10 wt% PVA and 0%, 3%, 5% and 7% PEG. Rheological measurements and dynamic light scattering are performed over a period of about 30 days, during which gelation of the 10% PVA/7% PEG blend and partial gelation of the blends with lower PEG concentrations were observed. The chapter is organized as follows. The experimental details and data analysis are described in Section 5.2. Results are presented in Section 5.3 and discussed in Section 5.4, and conclusions are given in Section 5.5.

5.2 Experiment

5.2.1 Materials

PVA with a molecular weight M_w=115,000 g/mol and PEG with M_w = 1,500 g/mol were purchased from Scientific Polymer Products, Inc., and used without further purification. PVA solutions of concentration c ranging from 0.5 wt% to 10 wt% were prepared by weighing the components and dissolving in distilled water at 90°C in a covered conical flask, followed by stirring for 3 hours. PVA/PEG blends were prepared by adding PEG powder to 10 wt% PVA solutions that had been stirred for one hour at 90 °C. The blends were stirred for another two hours. We refer to the blends by their nominal PEG concentrations (c_{PEG} = mass PEG/(mass PEG + mass water)) as indicated in Table 5.2.1; their actual compositions are given in the Table. The covered samples were then cooled to room temperature in air, which took about 40 minutes. Samples were poured into cylindrical glass cuvettes 10 mm in diameter and 130 mm in length for the light scattering experiments, and the remainder was poured into separate bottles and retained for rheological measurements. Samples were stored at room temperature (23.5°C ± 1.5°C) for the duration of the aging experiments.

Table 5.1: Composition of the polymer blends.

Sample	Composition					
	water		PVA		PEG	
	mass(g)	wt%	mass(g)	wt%	mass(g)	wt%
10% PVA/0% PEG	50	90.00	5.56	10.00	0.00	0.00
10% PVA/3% PEG	50	87.56	5.56	9.73	1.55	2.71
10% PVA/5% PEG	50	85.93	5.56	9.55	2.63	4.52
10% PVA/7% PEG	50	84.29	5.56	9.37	3.76	6.34

5.2.2 Measurements and Data Analysis

Rheological measurements were performed on the samples at aging times up to about 30 days using an AR-1500ex stress-controlled rheometer (T.A. Instruments) using a parallel-plate

geometry with an upper plate diameter of 40 mm and a gap of 1 mm. Both steady-state flow and oscillatory shear measurements were performed for each sample. In both cases, the sample was pre-sheared at a shear stress of 1 Pa followed by a 20 min relaxation to ensure that the sample was in a reproducible initial state prior to beginning the measurements. For the steady-state flow experiments, the range of applied stress was 0.01 Pa to 1000 Pa. The oscillatory experiments were performed at a stress amplitude of 1 Pa, which we confirmed was within the linear regime, over a frequency range of 0.01 Hz to 100 Hz. The rheological experiments were performed at a temperature of at $T = 25°\mathrm{C}$. A home-made environmental housing enclosed the rheometer tool to minimize solvent evaporation during the experiments.

Dynamic light scattering measurements were carried out for each sample around the same time as the rheological measurements. We used an ALV-CGS3 spectrometer-goniometer equipped with a digital correlator and a helium-neon laser with wavelength $\lambda = 632.8$ nm. The scattering angle was varied from 30° to 150°. All light scattering experiments were done at room temperature. The intensity autocorrelation function $g^{(2)}(q,\tau)$ of the scattered light was measured as a function of the lag time τ. For scattering obeying Gaussian statistics, $g^{(2)}(q,\tau)$ is related to the electric field autocorrelation function $g^{(1)}(q,\tau)$ through the Siegert relation [29],

$$g^{(2)}(q,\tau) = 1 + \beta \left| g^{(1)}(q,\tau) \right|^2, \tag{5.1}$$

where β is a geometric factor with a value of $\beta = 0.35$ for our experiments.

Previous light scattering studies of semidilute polymers have revealed two relaxation modes, one of which is due to the translational diffusion of individual polymer coils while the other results from the motion of aggregates [29, 30, 31]. The correlation functions we measure in our experiments are similar, all showing two non-exponential contributions to their decay. We therefore fit $g^{(1)}(q,\tau)$ to a sum of two Kohlrausch-Williams-Watts (KWW)—stretched exponential functions [29, 30],

$$g^{(1)}(q,\tau) = A_f \exp[-(\tau/\tau_{fe})^{\gamma_f}] + A_s \exp[-(\tau/\tau_{se})^{\gamma_s}], \tag{5.2}$$

where the parameters A_f and A_s represent the amplitudes of the fast and slow modes and $A_f + A_s = 1$. τ_{fe} and τ_{se} are the effective relaxation times of the fast and slow modes, and the exponents γ_f and γ_s characterize the widths of the distributions of relaxation times. The mean relaxation times for each mode are

$$\tau_f = \int_0^\infty \exp[-(\tau/\tau_{fe})^{\gamma_f}]d\tau = (\tau_{fe}/\gamma_f)\Gamma(1/\gamma_f) \tag{5.3}$$

and

$$\tau_s = \int_0^\infty \exp[-(\tau/\tau_{se})^{\gamma_s}]d\tau = (\tau_{se}/\gamma_s)\Gamma(1/\gamma_s), \tag{5.4}$$

respectively, where Γ is the gamma function. In practice, it is the intensity autocorrelation function that is measured, so we fit to $g^{(2)}(q,\tau)$ to the function

$$\sqrt{g^{(2)}(q,\tau) - 1} = B + n[A_f \exp[-(\tau/\tau_{fe})^{\gamma_f}] + (1 - A_f)\exp[-(\tau/\tau_{se})^{\gamma_s}], \tag{5.5}$$

where B is a background term and n is a normalization factor that accounts for the fact that some of the data were summed over more than one run.

More generally, the field autocorrelation function $g^{(1)}(q,\tau)$ can be modeled as a sum over a distribution of experimental relaxation times $A(t)$ according to

$$g^{(1)}(q,\tau) = \int_0^\infty A(t)\exp(-\tau/t)dt. \tag{5.6}$$

We determine the distribution function $A(t)$ using a regularized Laplace inversion program [38] based on that originally presented by Provencher [39, 40].

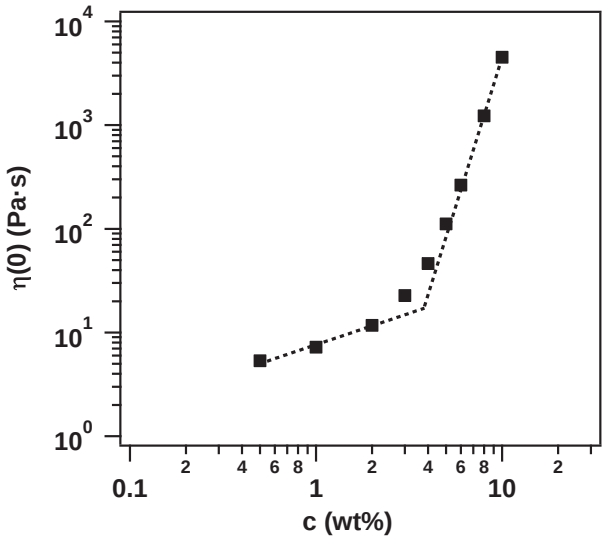

Figure 5.1: Concentration dependence of the zero-shear-rate viscosity of PVA solutions. The line through the data at low c has a logarithmic slope of 0.60, while that at high c has a slope of 5.76. The lines intersect at the overlap concentration c_e of 3.8 wt% in this case.

5.3 Results

5.3.1 Rheological Measurements

We first measured the viscosity η of pure PVA solutions as a function of concentration c. The zero-shear-rate viscosity $\eta(0)$ is plotted as a function of c in Fig. 5.1. At low concentrations, $\eta(0)$ increases approximately as $c^{0.6}$, while the increase is substantially faster at higher c. The crossover between the low and high concentration behavior occurs at $c \approx 3.8$ wt%, which we identify as the overlap concentration c_e at which entanglements between polymer chains become significant [41]. The concentration of PVA in the solutions studied in our aging experiments is 10 wt%, about 2.6 times greater than c_e. At this concentration, we expect the polymer chains to be highly overlapped and the solution to be strongly viscoelastic. The mesh size ξ which characterizes the distance between entanglement points in the chains can be estimated using [1, 42, 43]

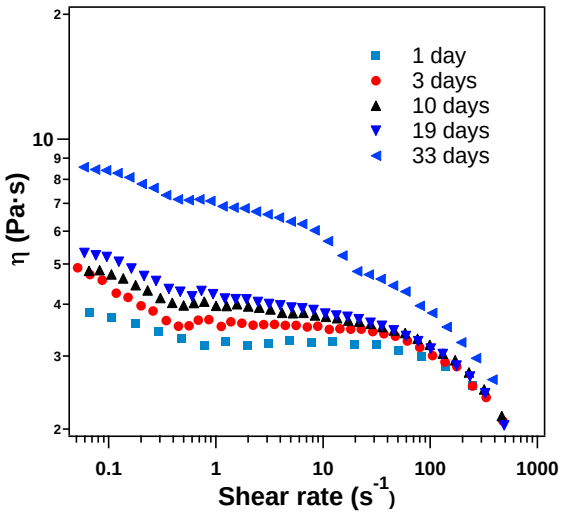

Figure 5.2: Viscosity as a function of shear rate determined from steady-state flow measurements for a 10% PVA solution at the aging times indicated.

$$\xi = R_g(c_e/c)^{0.75}, \tag{5.7}$$

where R_g is the radius of gyration of the polymer molecules. ξ decreases with increasing polymer concentration above c_e. R_g can be estimated from c_e and the molecular weight M_w as

$$R_g = \left(\frac{3M_w}{4N_A\pi c_e}\right)^{1/3}, \tag{5.8}$$

where N_A is Avogadro's number [42, 43]. For $c = 10$ wt% and $M_w = 115,000$ g/mol, Eqs. (5.7) and (5.8) give $R_g \approx 10$ nm and a mesh size ξ around 5 nm, which is similar to the value of about 7 nm estimated from the number of PVA chains per unit volume at this concentration.

Fig. 5.2 shows the viscosity of a 10 wt% PVA solution as a function of shear rate $\dot{\gamma}$ for ages ranging from 1 to 33 days. Generally, three regimes are observed as $\dot{\gamma}$ is increased. At low shear rates, η decreases with increasing shear rate. η becomes relatively constant at intermediate $\dot{\gamma}$, then at high shear rates it decreases again, but more rapidly. At a given shear rate, η increases with age. At $\dot{\gamma} = 1$ s^{-1}, η increases from 3.26 Pa·s at an age of one

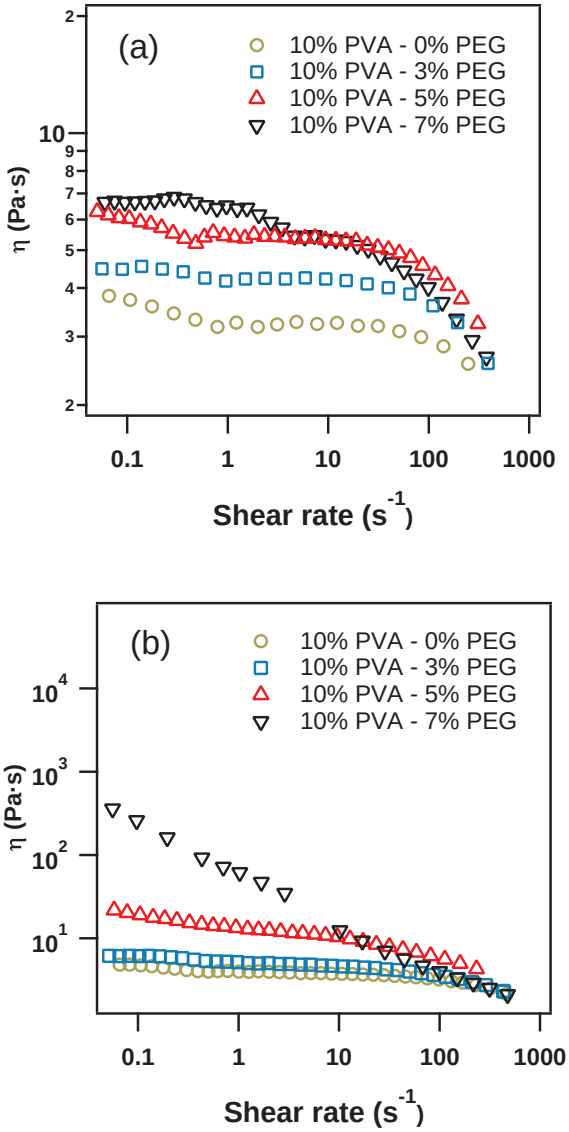

Figure 5.3: Viscosity of PVA/PEG blends with different concentrations of PEG as a function of shear rate at aging time of: (a) 1 day and (b) 10 days.

day to 6.85 Pa·s after 33 days. As the sample ages, the plateau at intermediate $\dot{\gamma}$ becomes less distinct, and after 33 days the solution is shear thinning over the entire range of shear rates.

Fig. 5.3 shows η as a function of shear rate for PVA/PEG blends at ages of 1 day (Fig. 5.3(a)) and 10 days (Fig. 5.3(b)). The viscosity generally increases with c_{PEG} at both ages. At 1 day, the viscosity at $\dot{\gamma} = 1$ s^{-1} increases by about a factor of two as c_{PEG} increases from 0 to 7 %. At high c_{PEG}, the low shear-rate shear-thinning regime disappears and the viscosity shows a Newtonian plateau at low $\dot{\gamma}$. Aging has a dramatic effect on the viscosity of the high-PEG-concentration blends, as shown in Fig. 5.3(b). After aging for 10 days, the low-shear viscosity of the blend with $c_{PEG} = 7\%$ is almost two orders of magnitude higher than that of the pure PVA solution. In this case, the blend is shear-thinning over the full range of $\dot{\gamma}$ studied.

The storage modulus G' and loss modulus G'' of the PVA/PEG blends were determined from small-amplitude oscillatory shear measurements. The results are shown as a function of frequency ω and age in Fig. 5.4. Fig. 5.4(a) shows the moduli for the pure PVA solution. In this case, $G'' > G'$ for all ages at all accessible frequencies. Both G' and G'' increase with frequency over the entire frequency range examined. The data suggest a crossover frequency just beyond the high end of the experimental range, at around 1000 rad/s. In the linear viscoelastic approximation this frequency would correspond to the longest relaxation time in the system, i.e., about 6.3 ms. G'' increases slightly with age at all frequencies. G' also increases with age, although in this case the increase is frequency-dependent. As seen in Fig. 5.4(a), for ω ranging from a few times 10^{-1} s^{-1} to a few times 10^{0} s^{-1}, G' increases by more than an order of magnitude as the sample ages 33 days, but the increase is much less at both lower and higher frequencies. The values of G' and G'' at $\omega = 1$ rad/s are plotted for all our materials in Fig. 5.5.

The Maxwell model predicts that $G' \propto \omega^2$ and $G'' \propto \omega^1$ at low frequencies. As seen in Fig. 5.4(a), the viscous modulus and the elastic modulus at the upper end of the experimental

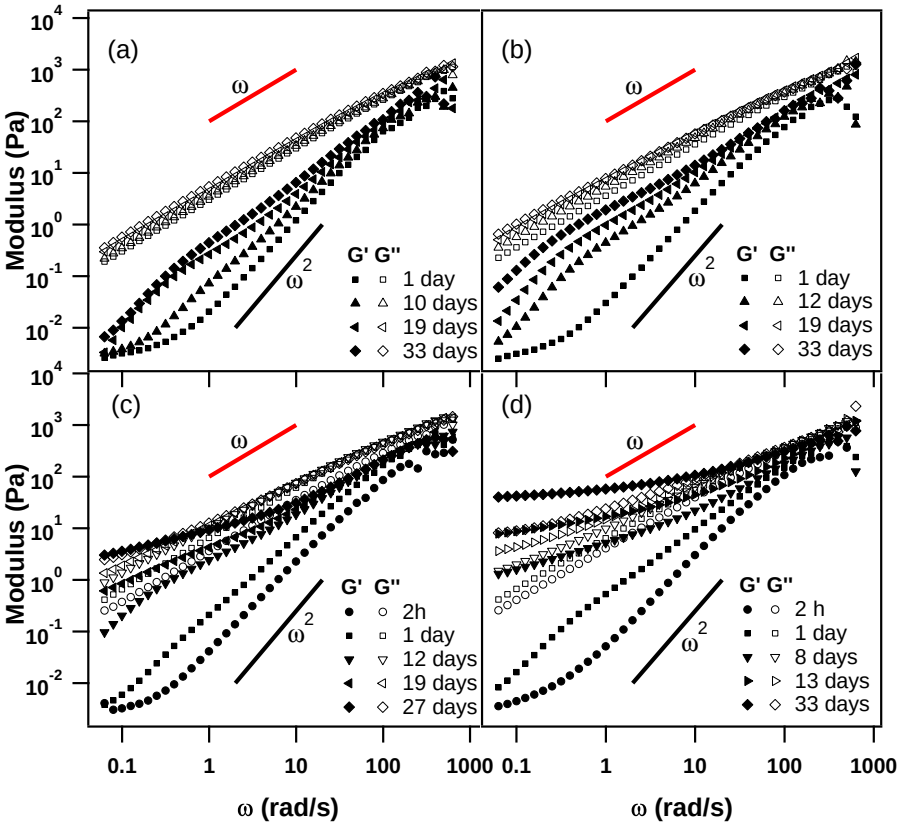

Figure 5.4: Storage and loss moduli for the PVA solution and PVA/PEG blends during aging: (a) 10% PVA/0% PEG; (b) 10% PVA/3% PEG; (c) 10% PVA/5% PEG; (d) 10% PVA/7% PEG.

frequency range show a frequency dependence reasonably close to the predicted behavior. At low frequencies, however, the behavior of the elastic modulus is more complicated and depends on age. For the fresh PVA sample, G' appears to approach a plateau at low frequencies, suggesting the presence of some very slow dynamics. This plateau appears to smear out somewhat and move to slightly higher frequencies as the sample ages. This slower-than-Maxwell frequency dependence of G' indicates a heterogeneous microstructure which can not relax at low frequencies [22, 23, 25, 45, 46], and we interpret it as a signature of the presence of microphase-separated domains.

Data for the PVA/PEG blends are shown in Fig. 5.4(b)-(d). For all of the freshly prepared blends, G'' remains greater than G' over the entire accessible frequency range and both quantities show a frequency dependence similar to that for the pure PVA. As shown in Fig. 5.5, both moduli increase with age, but while G'' increases only slightly as c_{PEG} increases, the interesting low-frequency behavior of the elastic modulus becomes much more pronounced, and for $c_{PEG} = 7\%$, the value of G' at $\omega = 1$ rad/s increases by more than two orders of magnitude after 33 days. Both the 10% PVA/5% PEG and the 10% PVA/7% PEG blends undergo a gel transition: $G'(\omega)$ first becomes parallel to and then crosses over the G'' data, with G' approaching a constant at low frequencies in the gel state. The transition occurs at an age of about 27 days for the material with 5% PEG and about 8 days for the 10% PVA/7% PEG blend.

Figure 5.6(a) shows n_1, the average logarithmic slope of $G'(\omega)$ for frequencies between 0.0628 to 0.314 rad/s, plotted as a function of age. $n_1 = 2$ for the simple Maxwell model. For the pure PVA, $n_1 < 2$ at early times, but rises to a value close to 2 as the sample ages. For the PVA/PEG blends, n_1 increases initially, but then decreases again as the materials gel over time. This late-time decrease occurs at earlier ages as the concentration of PEG is increased. The low value of n_1 in the fresh samples is an indication of rheological heterogeneity due to microphase separation, while the drop in n_1 at high ages in the blends indicates the appearance of a low-frequency elastic plateau in the gel phase. The loss tangent $\tan\delta = G''/G'$ for the pure PVA and the 10% PVA/7% PEG blend is plotted in Fig. 5.6(b). A primarily

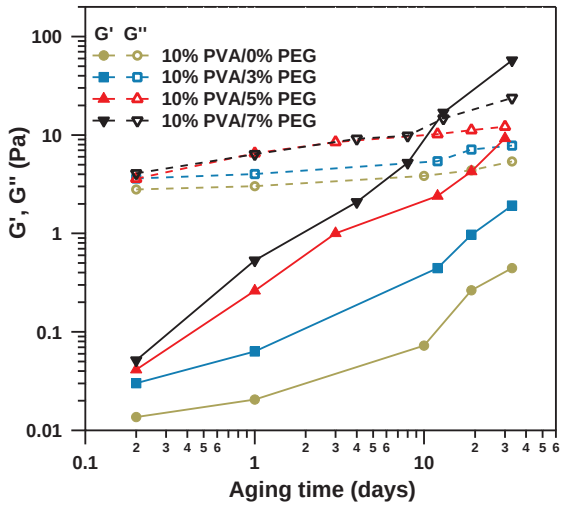

Figure 5.5: G' and G'' at $\omega = 1$ s^{-1} as a function of age for the pure PVA and the PVA/PEG blends with different c_{PEG} as indicated.

viscous material is characterized by $\tan\delta > 1$, while $\tan\delta < 1$ for an elastic material [13, 24]. As implied by the data in Fig. 5.4, our freshly prepared materials all have $\tan\delta > 1$ for all frequencies studied. $\tan\delta$ decreases with age for all samples, but for the pure PVA solution it is still greater than one at all frequencies after 33 days. In the case of the 10% PVA/7% PEG blend, $\tan\delta$ becomes less than 1 at low frequencies at an age of 10 days, but it remains greater than 1 at high frequencies.

5.3.2 Dynamic Light Scattering

The field autocorrelation functions $g^{(1)}(\tau)$ determined from dynamic light scattering experiments on a one-day old 10% PVA solution are shown in Fig. 5.7. Data for three different scattering angles are shown. $g^{(1)}(\tau)$ was determined from the measured intensity autocorrelation function $g^{(2)}(\tau)$ using Eq. (5.1). In each case, two dominant decay modes are observed: one at time scales around 1 ms and a second at time scales of 10 s. Similar behavior has been observed previously [30, 31], and it has been determined that the fast mode arises from

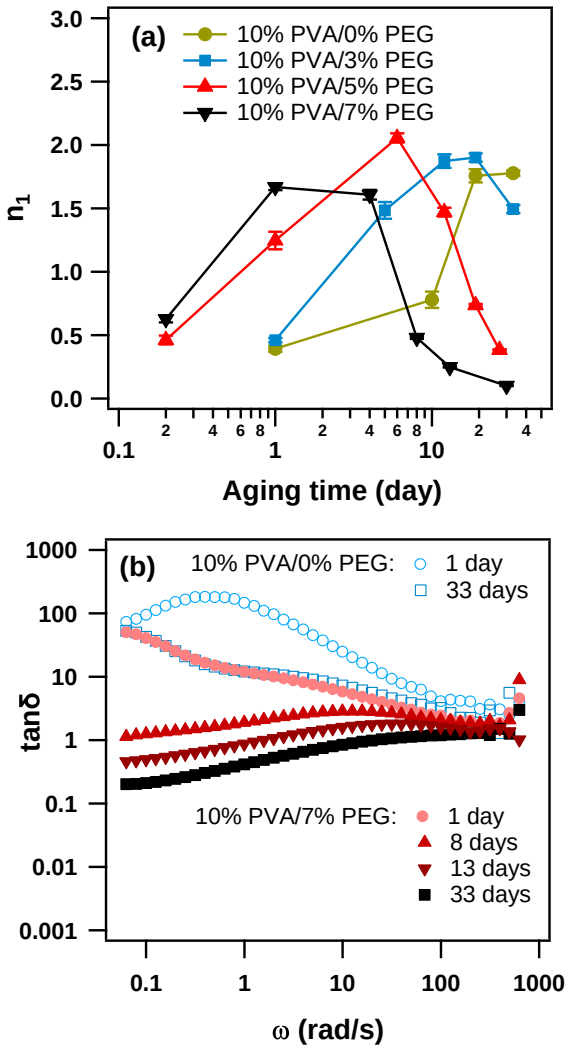

Figure 5.6: (a) The logarithmic slope n_1 of $G'(\omega)$ at frequencies between 0.0628 to 0.314 rad/s of PVA blends with different concentrations of PEG versus aging time; (b) $\tan\delta$ versus frequency for 10% PVA and 10% PVA/7% PEG at different aging times as indicated.

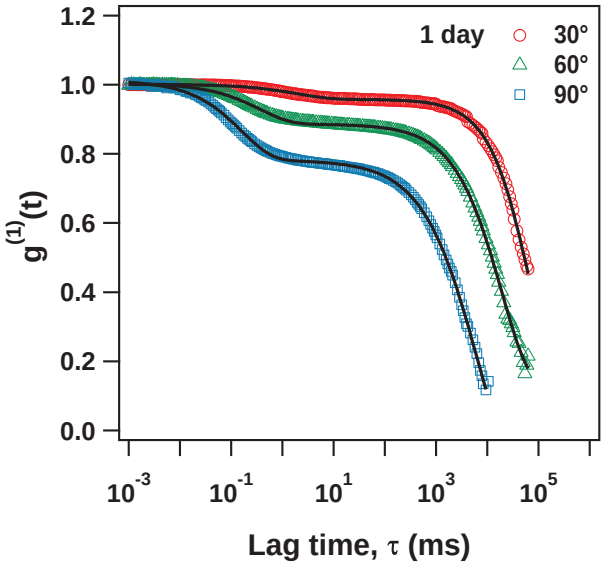

Figure 5.7: Field autocorrelation function $g^{(1)}(\tau)$ for 10% PVA solution at different scattering angles as indicated. The solid curves are fits to Eq. (5.2). The sample age is 1 day.

the motion of free polymer coils and the slow mode from the motion of larger aggregates in the solution [30, 29, 31]. Fits to the double-stretched-exponential model given by Eq. (5.2) are also plotted in Fig. 5.7 and describe the data well in all cases. Both the fast and slow relaxation times depend on scattering angle. We find that the mean relaxation time τ_f of the fast mode is well-described by a power-law dependence on q, with $\tau_f \propto q^{-2.3\pm0.2}$. The stretching exponent for this mode is $\gamma_f = 0.75 \pm 0.08$, independent of q. τ_s, the mean relaxation time of the slow mode, behaves as $\tau_s \propto q^{-2.9\pm0.6}$, with stretching exponent $\gamma_s = 0.84 \pm 0.02$ at $\theta = 30°$ and $\gamma_s = 0.73 \pm 0.01$ at $\theta = 90°$. For dilute PVA solutions, the fast mode is characterized by a diffusion coefficient $D_c = (\tau_f q^2)^{-1}$ [30, 31], in which case, $\tau_f \propto q^{-2}$ and $\gamma_f \approx 1$. In semi-dilute PVA solutions, the slow mode has been reported to show a power-law dependence on q with an exponent in the range 2.1–2.3, and with γ_s depending strongly in q due to the formation of large clusters [30]. In our case, the power law index for τ_f is slightly more negative than -2 indicating that the fast mode is slightly subdiffusive, and our value of γ_f is less than one, which indicates that the fast relaxation time has a wider distribution. The higher value of the power-law index for τ_s suggests that the dynamics governing the slow mode is significantly subdiffusive, probably reflecting the formation of large aggregates that cannot diffuse freely. The q dependence of γ_s suggests that the aggregates are quite heterogeneous [30, 47, 48, 49].

Fig. 5.8(a) shows $g^{(1)}(\tau)$ at a scattering angle of 90° for a 10% PVA solution at different aging times. As above, $g^{(1)}(\tau)$ exhibits two decay modes at each age. As the sample ages, the fast mode contributes less to the decay of $g^{(1)}(\tau)$ while the contribution of the slow mode increases. The mean relaxation times τ_f and τ_s, the ratio A_s/A_f of the amplitudes of the two modes, and the stretching exponents γ_f and γ_s obtained from fits of Eq. (5.2) to the data are plotted as a function of aging time in Fig. 5.9. The data for the 10% PVA solution are plotted as circles in each sub-figure of Fig. 5.9. Neither τ_f (plotted in Fig. 5.9(a)) nor γ_f (Fig. 5.9(c)) changes significantly with age for the pure PVA solution, although γ_f shows some scatter. τ_s (Fig. 5.9(a)) decreases and γ_s (Fig. 5.9(d)) increases slightly with age initially, but both remain constant within the experimental scatter at later ages. On the other hand, the ratio

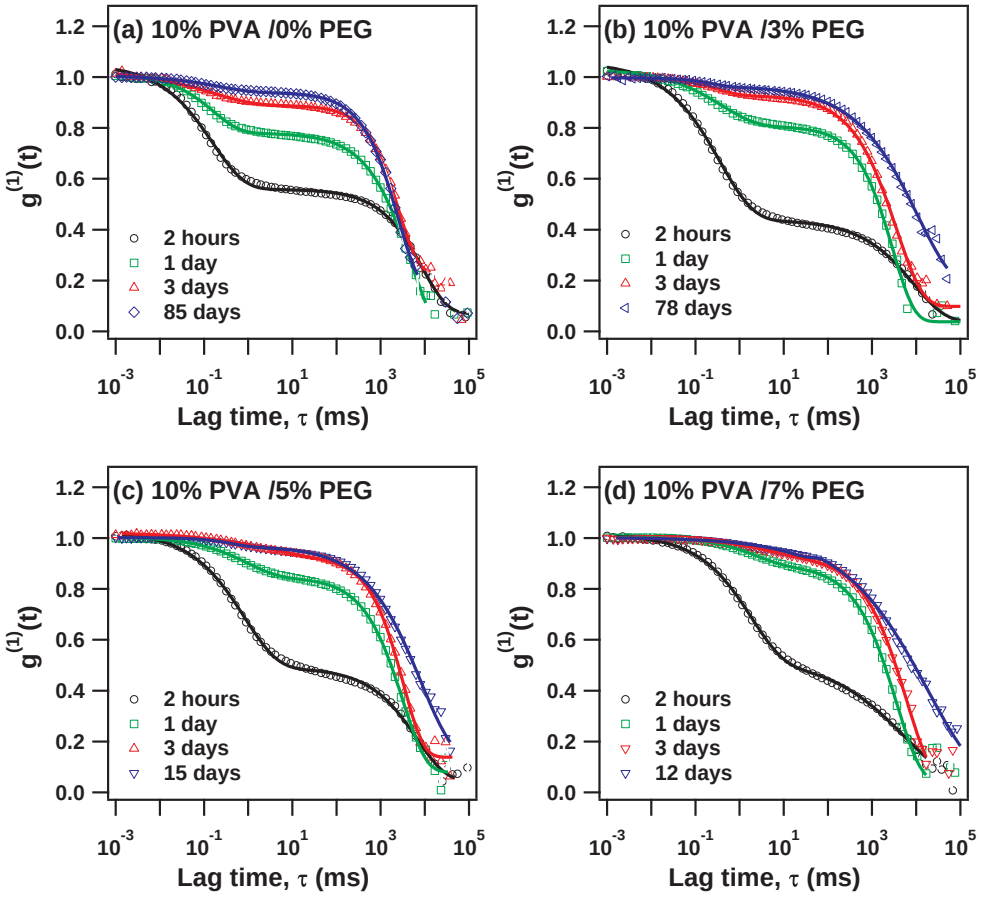

Figure 5.8: Field autocorrelation function $g^{(1)}(\tau)$ for PVA/PEG blends at a scattering angle of 90° and at different ages as indicated. The solid curves are fits to Eq. (5.2).

A_s/A_f (Fig. 5.9(b)) increases steadily as the sample ages, consistent with the observations made above.

The distribution of the relaxation times for the 10% PVA solution, calculated using the regularized inverse Laplace transform method discussed in Section 5.2.2, is shown in Fig. 5.10(a). As expected, the distribution has two peaks, one centered around 10^{-1} ms, and the other around a few times 10^3 ms. The position of the peak corresponding to the fast relaxation does not change during aging. In contrast, the peak of the distribution of the slow relaxation times is centered at a longer time for the fresh PVA solution (indicated as "2h" in Fig. 5.10(a).) than at later ages. However, the contribution of the fast mode (corresponding to the area under the fast relaxation time peak) decreases and that of the slow mode increases substantially with aging time. These results are consistent with the stretched exponential fits discussed above.

The field autocorrelation functions $g^{(1)}(\tau)$ measured at 90° for the PVA/PEG blends are shown in Fig. 5.8(b)–(d) for several aging times. For each blend, the contribution of the slow mode to the decay of $g^{(1)}(\tau)$ is similar to that of the fast mode at an age of 2 hours. As the samples age, the slow mode contributes more, and the slow mode dominates after 1 day for all of the blends. It is seen from Fig. 5.8 that the contribution of the slow mode to the relaxation of $g^{(1)}(\tau)$ increases more quickly as c_{PEG} increases.

We also fit the $g^{(1)}(\tau)$ data for the blends to Eq. (5.2). The results are plotted in Fig. 5.9 along with those for the pure PVA solution. The addition of PEG has different effects on the fast and slow modes, and in fresh and aged samples. In samples less than about four days in age, increasing c_{PEG} from 0 to 7% has no effect on τ_s, while in contrast τ_f increases (i.e., the fast relaxation process slows down) by an order of magnitude. This suggests that PEG has a significant effect on the motion of single PVA molecules, but not the motion of the larger aggregates.

The effect of PEG on the aging of the blends is quite significant. As shown in Fig. 5.9(a),

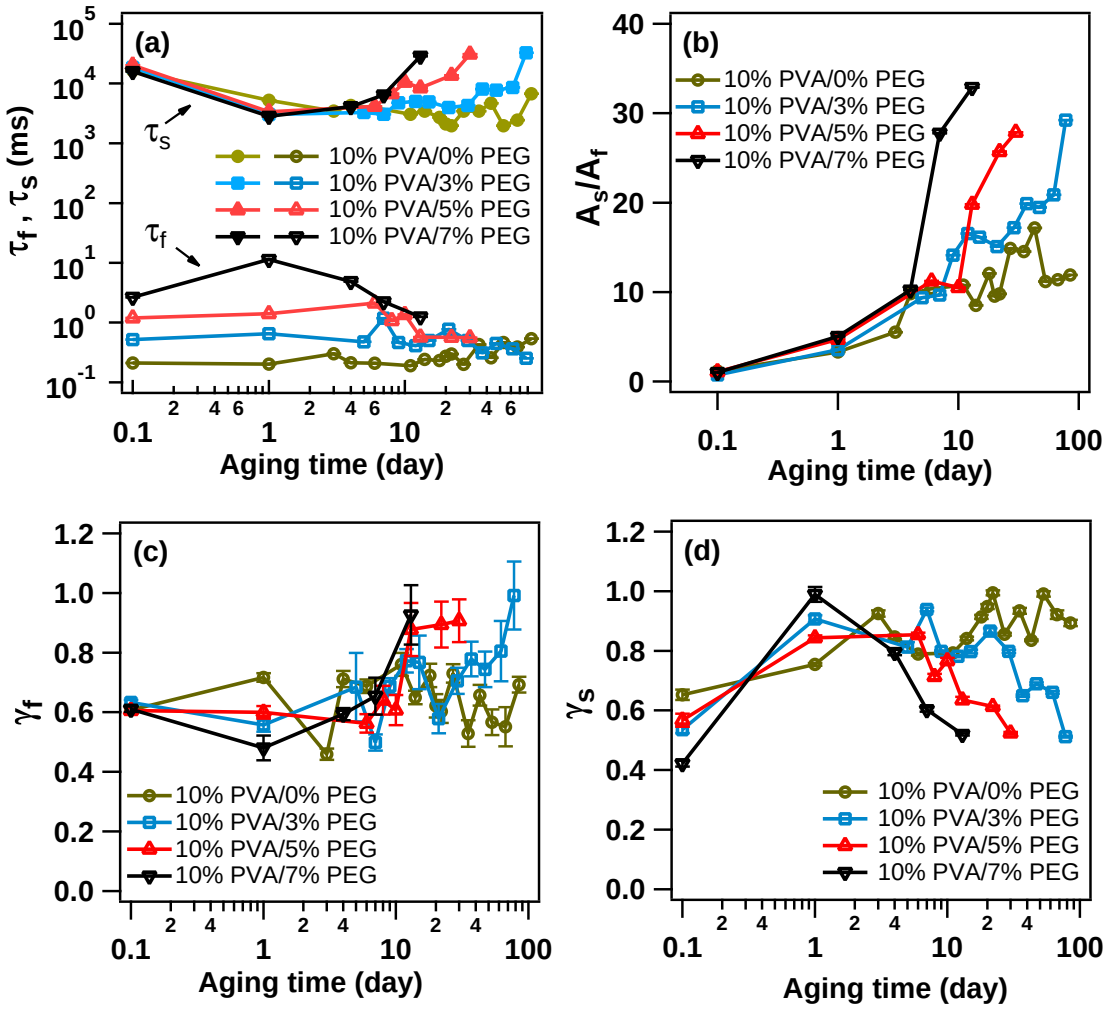

Figure 5.9: Parameters obtained by fitting the field autocorrelation functions to Eq. (5.2): (a) fast and slow relaxation time τ_f (open symbols) and τ_s (filled symbols), (b) ratio of amplitude A_s/A_f, (c) fast mode stretching exponent γ_f and (d) slow mode stretching exponent γ_s. Lines are to guide the eye. Statistical error bars from the fit are shown in each case.

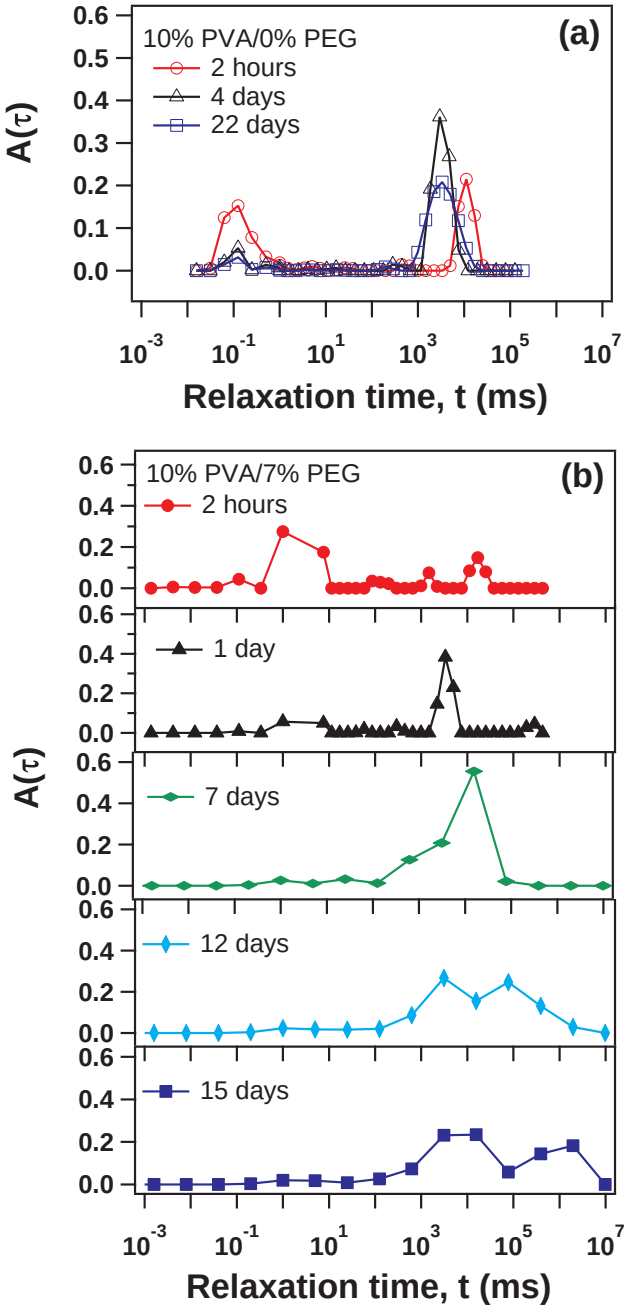

Figure 5.10: Distribution of relaxation times computed by the inverse Laplace transform method for (a) the 10% PVA solution and (b) the 10% PVA/7% PEG blend at different aging times as indicated in the figure.

τ_s increases with age after the first few days, and the age at which this becomes noticeable decreases as c_{PEG} increases. On the other hand, τ_f decreases with age, particularly for the samples with higher PEG concentration, and at high ages appears to be the same within the experimental scatter for all of our samples. Fig. 5.9(b) shows that the slow mode grows in importance more quickly as c_{PEG} is increased. A_s/A_f shows an upturn on this semi-logarithmic plot at an age that again decreases as the concentration of PEG is increased. Although the data for γ_f are scattered, Fig. 5.9(c) suggests that, for the blends, γ_f starts to increase—indicating a narrowing of the distribution of relaxation times—at a certain age, with the increase again appearing earlier for higher c_{PEG}. Finally, the stretching exponent γ_s of the slow relaxation process, plotted in Fig. 5.9(d), initially increases, then later decreases with age. As above, increasing c_{PEG} moves the change in behavior to earlier ages. For the 10% PVA/7% PEG blend, which has the highest c_{PEG} used in our study, $A_s/A_f \approx 33$ and $\gamma_s \approx 0.52$ at an age of 12 days. Consistent with this, the corresponding field autocorrelation function, shown in Fig. 5.8(d), shows almost no evidence of the fast decay and has a slowly-decaying tail at long lag times.

As in the rheological data presented above, the changes we observe in the light scattering data are a result of the materials undergoing a gel transition as they age. Beyond the gel transition, the motion of the polymer molecules becomes non-ergodic and the magnitude of the intensity autocorrelation function $g^{(2)}(\tau)$ decreases at low τ. In this case the Siegert relation, Eq. (5.1), can no longer be used to calculate $g^{(1)}(\tau)$ from $g^{(2)}(\tau)$ [29]. The intensity autocorrelation functions for the four samples are plotted at ages of 12, 15, 30 and 38 days in Fig. 5.11(a), (b), (c) and (d), respectively.

At an age of 12 days, the intensity autocorrelation function for the 10% PVA/7% PEG blend shows a slowly-decreasing long-τ tail. At an age of 15 days, the low-τ value of $g^{(2)}(\tau)$ for the blend with the highest PEG concentration decreases from 1 to 0.8. By 30 days, it has decreased to 0.65. This decrease signals the appearance of non-ergodicity resulting from the gel transition [35, 36], which we estimate to occur at an age of 15 days for the 10% PVA/7% PEG blend. At smaller scattering angles, the depression of the intensity correlation function

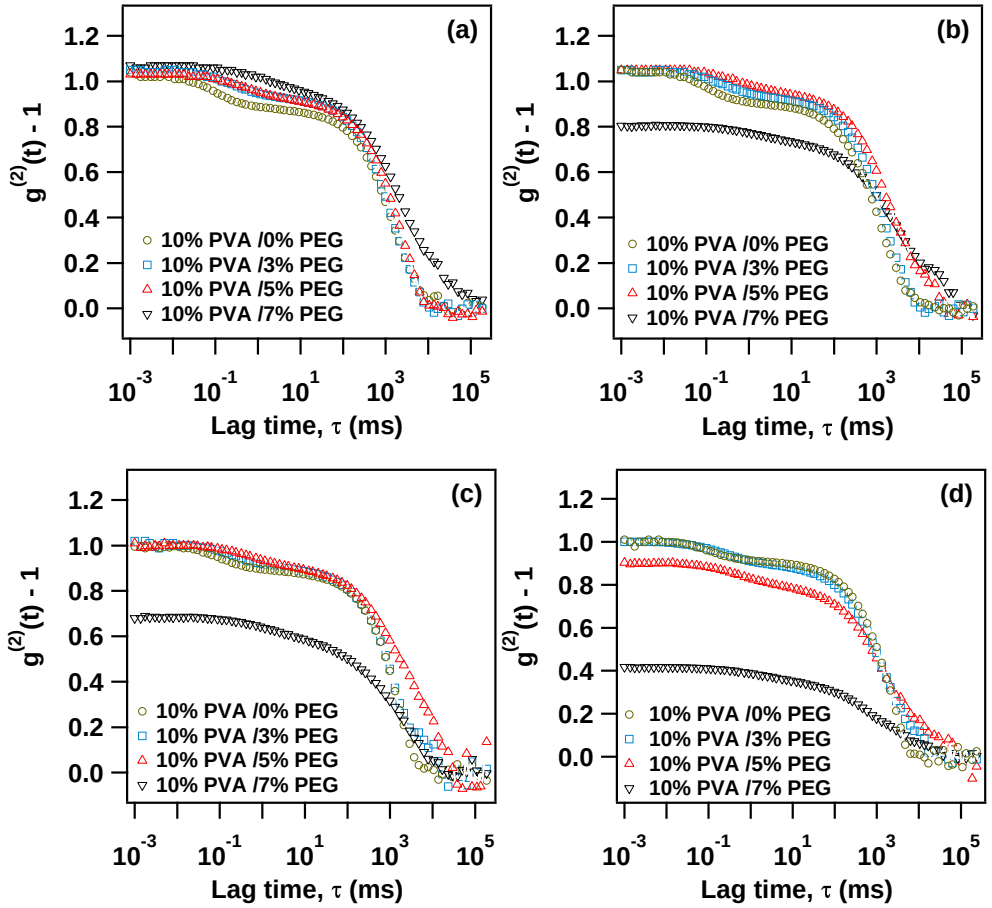

Figure 5.11: Intensity autocorrelation functions for PVA/PEG blends with concentrations of PEG as indicated and at aging times of (a) 12 days, (b) 15 days, (c) 30 days and (d) 38 days. The scattering angle is 90°.

occurs even earlier. $g^{(2)}(\tau)$ becomes smaller than one after 12 days at $\theta = 60°$.

The intensity autocorrelation function for the 10% PVA/5% PEG blend shows a slowly-decreasing long-τ tail at an age of 30 days (Fig. 5.11(c)) while its limiting value at low τ decreases at 38 days (Fig. 5.11(d)). A slowly-relaxing tail for the 10% PVA/3% PEG blend appears by 78 days, but no depression of the initial amplitude of $g^{(2)}(\tau)$ was observed during the aging times examined.

The distribution of the relaxation times for the 10% PVA/7% PEG blend calculated by the inverse Laplace transform method is shown in Fig. 5.10(b) at five different ages. Compared with the results for the pure PVA solution plotted in Fig. 5.10(a), the peak corresponding to the distribution of fast relaxation times is shifted to longer times in the fresh blend while the position of the slow relaxation time peak is similar to that of the PVA solution. The fast peak almost disappears after 7 days, consistent with the behavior of the intensity autocorrelation function discussed above. Interestingly, the slow peak becomes very broad as the blend ages, with a sudden broadening to long relaxation times occurring at day 12. This broadening is also a sign of the gel transition [35, 36] and gives a gel point at 12 days for the 10% PVA/7% PEG blend and 30 days for the 10% PVA/5% PEG blend. Not surprisingly, these ages coincide with the appearence of the long-τ tail in the correlation function, but are slightly earlier than the ages at which the materials become non-ergodic.

5.4 Discussion

Our rheological and dynamic light scattering measurements of the PVA/PEG blends provide complementary information about their structure and the changes that take place as they age.

Our measurements of steady–state viscosity as a function of shear rate showed that the PVA solution and PVA/PEG blends are shear thinning at low and high shear rates with a

viscosity plateau at intermediate $\dot{\gamma}$. PVA has a large number of hydroxyl groups [25, 28, 44]. In our materials, the concentration of PVA is above the overlap concentration, and the average distance between the PVA chains is small, typically about 5 nm. As a result, hydrogen bonds form between the chains, and at the lowest stress, the viscosity is relatively high. Some of these hydrogen bonds are broken when the solution is sheared, leading to shear thinning in the low-shear-rate regime.

At intermediate shear rates, however, the PVA polymers tend to be aligned by the shear. This allows the chains to approach each other more closely, resulting in the shear-induced formation of new hydrogen bonds [28, 44]. A balance between the breakage of existing hydrogen bonds and the formation of new bonds results in the observed plateau in the viscosity. At high shear rates, the rate at which hydrogen bonds are broken by the shear exceeds the rate of new bond formation, and the material becomes shear-thinning again.

Both the rheology and dynamic light scattering show that the addition of PEG has little effect on the macroscopic properties of the fresh PVA materials, although it does affect the microscopic properties and has a dramatic effect on their aging behavior. The millimeter-scale viscosity and shear modulus of the fresh PVA/PEG blends, measured with the rheometer, are within a factor of two of those of pure PVA solution. In addition, the slow relaxation time τ_s measured in the dynamic light scattering experiments, which corresponds to the diffusion of large aggregates, is the same for the pure PVA solution and the PVA/PEG blends. These results indicate that the PEG has little effect on the large-scale structure in the fresh samples. The bulk properties of these PVA blends are due to the entangled/hydrogen-bonded aggregates, which are not changed significantly by the PEG. On the other hand, the fast relaxation time τ_f, which corresponds to the diffusive motion of free polymer coils, becomes significantly longer as the concentration of PEG is increased, likely indicating that the PEG molecules increase the viscosity of the solvent through which the PVA molecules diffuse. We have observed the same behavior in microrheological measurements presented in Chapter 6 [51].

The influence of PEG becomes more pronounced as the materials age, its most obvious effect being to increase the low-frequency elasticity of the blends and to accelerate gelation. As seen in Figs. 5.4 and 5.5, the low frequency viscous modulus of pure PVA increases very slowly with age. The increase becomes more rapid as the concentration of PEG is increased. The effect of PEG on the viscous modulus becomes particularly pronounced in the 10%/7% blend (Fig. 5.4(d)), for which G'' increases by about a factor of 30 at the lowest frequencies over 33 days and becomes much more weakly dependent on frequency. This indicates the development of microstructure which inhibits the low-frequency relaxation of the system.

The effect of PEG on the elasticity of the blends is more dramatic. The pure PVA shows the development of a "hump" in $G'(\omega)$ for frequencies between 0.1 and 10 rad/s. This hump appears at earlier times as c_{PEG} increases, and in the blends with 7% and 5% PEG it broadens and grows to the extent that G' becomes larger than G'' at low frequency. At long ages this feature develops into a flat low-frequency elastic plateau, indicating gel-like behavior at low ω, although G' continues to increase with ω at high frequencies.

The gel point is normally identified as the point – in this work, the age – at which the viscous and elastic moduli have the same power-law dependence on frequency, for all frequencies. By definition, $\tan\delta = G''/G'$ would be constant, independent of frequency, at the gel point. This behavior is not seen in our blends, however—$\tan\delta$ is never independent of frequency over even a small range of frequencies, as seen in Fig. 5.6(b), and there is thus no clearly-defined gel transition in the rheological data. Similar behavior has been observed in the gelation as a function of temperature of low concentration solutions of syndiotactic PVA with a molecular weight five times higher than ours [24], and was attributed to microscopic phase separation in the sol phase prior to gelation. Our results are also consistent with this explanation, with the blends separating into PVA-rich and PVA-poor domains.

The low value of the power-law exponent of $G'(\omega)$, n_1, indicates the existence of inhomogeneity in our young samples before gelation [22, 44]. For a homogeneous polymer solution, the Maxwell model predicts $n_1 = 2$ at low frequencies [22, 23]. The deviation of n_1 from

this behavior indicates the presence of a heterogeneous microstructure, such as microphase-separated domains, which cannot relax at low frequencies [22, 23, 25, 45, 46]. As the blends age, the logarithmic slope of G' decreases due to the appearance of a low-frequency elastic plateau as the gel.

The intensity autocorrelation functions obtained from light scattering experiments on PVA solutions and the PVA/PEG blends display two relaxation modes in all cases. Previous studies have shown that the fast mode is related to the diffusion of free polymer coils, while the slow mode is due to the motion of aggregates or large clusters [29, 30, 31, 41]. For young samples, τ_f depends on c_{PEG} while τ_s does not, indicating that PEG affects the motion of the free chains but not of the aggregates. As the blends age, however, the fast relaxation time becomes faster and the slow relaxation time becomes slower, particularly for blends with higher c_{PEG}. Thus the mobility of the free polymer coils increases and that of the aggregates decreases with age. We suggest that as the blends age, an increasing amount of PVA is incorporated into aggregates in the PVA-rich domains, and the motion of the smaller PEG molecules begins to dominate the fast mode. This results in the fast mode becoming faster and an increase in the stretching parameter γ_f due to a narrower distribution of relaxation times.

Shibayama *et al.* suggested that the gel point can be determined from dynamic light scattering measurements by a dramatic increase in the scattered intensity, power-law behavior of the intensity autocorrelation function tail, a broadening of the relaxation time distribution function, or a depression of the initial amplitude of intensity autocorrelation function [32, 34, 36]. The first effect is due to the fact that inhomogeneities in the gel scatter light much more strongly than does the solution. The second and the third effects results from the formation of a large-scale network at the gel transition. The fourth occurs because the material becomes nonergodic at the gel point. We did not observe a sharp increase in intensity with aging time, and while the autocorrelation function broadened, it did not obviously display power-law behavior. We estimated the time of the gel transition using the latter two effects, but they did not occur simultaneously. For the 10% PVA/7% PEG blend, the

distribution of the slow relaxation times broadens after about 12 days, while $g^{(2)}(\tau)$ becomes depressed at low τ at an age of 15 days. For the 10% PVA/5% PEG blend, the relaxation time distribution broadens around 30 days and the amplitude of the intensity autocorrelation function decreasas after 38 days. It is clear that these two effects signal two different physical phenomena. The broadening of the relaxation time distribution occurs as a result of growth of the aggregates, while the decrease in $g^{(2)}(\tau)$ occurs when the system becomes nonergodic [35, 36]. Only the latter is an unambiguous indication that the material has gelled.

The bulk gel point determined from the shear rheometry is earlier than both of the microscopic estimates discussed above: 8 and 27 days for the 10% PVA/7% PEG and 10% PVA/5% PEG blends, respectively. The length scale probed in the oscillatory experiments is about 1 mm – the thickness of the samples in the rheometer – while the length scale l studied in our light scattering measurements is inversely proportional to the scattering vector q: $l = 2\pi/q$ [29]. At an scattering angle of 90°, $l \approx 335$ nm. Our results therefore suggest that the gel transition of our PVA/PEG blends happens earlier at larger scales than at smaller scales. More evidence for this comes from the scattering angle dependence of the decrease of the low-τ $g^{(2)}(\tau)$, which shows that the material becomes nonergodic earlier when probed on the larger length scales. The microrheological study reported in Chapter 6 [51] showed that the gel point is even later on the 100 nm scale.

Finally, we discuss the relationship between phase separation and gelation in these PVA materials. The gelation process of PVA materials has been studied for some time [14, 15, 16, 17, 20, 21], but there is still controversy about the details of the process [16]. Kanaya *et al.* suggested that gelation of PVA in dimethyl sulfoxide/water occurs after phase separation by spinodal-decomposition [14, 15, 17], while Takahashi *et al.* suggested that gelation occurs first and induces the phase separation [16].

Our experiments were performed on PVA and blends of PVA/PEG using pure water as a solvent, and so cannot be directly compared with the work of Ref. [16]. Nonetheless, our results do not support the gelation-induced phase separation mechanism. First, our low-

frequency oscillatory rheological measurements indicate micro-phase separation in our freshly made blends. The frequency-dependent behavior of $\tan\delta$ near the gel point provides further evidence that phase separation occurs before gelation [24]. In fact, we do not see evidence for gelation in our younger samples on either the bulk or the microscopic scale. In contrast, as discussed above, the different gel points observed by bulk rheology and dynamic light scattering indicate that the gel transition is length-scale dependent and proceeds from large to small scales [12]. It is therefore unlikely that the early microscopic phase separation could be induced by gelation. Preliminary small angle neutron scattering experiments (unpublished) are also consistent with phase separation occuring before gelation.

Overall, our results show that the addition of PEG to PVA solutions alters the microstructure of the material and causes the systems to phase separate, which enhances the formation of aggregates in the PVA-rich domains. Aggregates grow as the samples age and eventually form a continuous gel network. At the bulk gel point, a fractal percolation network spans the sample and the material becomes predominately elastic, but the sample still contains many regions that remain ungelled. As the sample ages further, the gelation proceeds from large scales to smaller scales as the network continues to grow.

5.5 Conclusion

Rheological and dynamic light scattering measurements were performed on concentrated PVA solution and PVA/PEG blends. Shear, the addition of PEG, and aging all affect the structure of the PVA solution. Shear-induced orientation induces increased hydrogen bonding in the PVA solution, but these hydrogen bonds break under stronger shear. In fresh samples, the presence of PEG affects the microscale properties significantly, but has less of an effect on the bulk response of the material. The blends with higher concentrations of PEG gel over the duration of these experiments.

Both the rheological and dynamic light scattering measurements show the existence of

micro-phase separation in the blends and suggest that the presence of PEG forces the PVA solution to phase separate and eventually to gel. There is no sharp gel transition as broadening of the distribution of the cluster sizes occurs before the material becomes nonergodic. The gel point at the bulk scale is earlier than that at the microscale, indicating that the sol-gel transition of the PVA/PEG material is length-scale dependent.

BIBLIOGRAPHY

[1] J. P. Cohen Addad, *The Physical Properties of Polymeric Gels* (Wiley, New York, 1996).

[2] M. Shibayama, Polym. J. **43**, 18 (2011).

[3] S. Santinath Singh, V. K, Aswal, and H. B. Bohidar, Polymer **50**, 5589 (2011).

[4] H. Bodugoz-Senturk, C. E. Macias, J. H. Kung, and O. K. Muratoglu, Biomaterials **30**, 589 (2009).

[5] C. M. Hassan and N. A. Peppas, Adv. Polym. Sci. **153**, 37 (2000).

[6] A. Dashevsky, A. R. Ahmed, J. Mota, M. Irfan, K. Kolter, and R. A. Bodmeier, Biomaterials **29**, 141 (2008).

[7] S. D. Hudson, J. L. Hutter, M.-P. Nieh. J. Pencer, L. E. Millon, and W. K. Wan, J. Chem. Phys. **130**, 034903 (2009).

[8] K. Urayama, S. Ogasawara, and T. Takigawa, Polymer **47**, 6868 (2006).

[9] H. S. Mansur, R. L. Oréfice, and A. A. P. Mansur, Polymer **45**, 7193 (2004).

[10] H. Assender and A.H. Windle, Polymer **39**, 4295 (1998).

[11] F. K. Oppong and J. R. de Bruyn, Eur. Phys. J. E **31**, 25 (2010).

[12] F. K. Oppong, P. Coussot, and J. R. de Bruyn, Phys. Rev. E **78**, 021405 (2008).

[13] F. Chambon and H. H. Winter, Polym. Bull. **13**, 499 (1985).

[14] T. Kanaya, M. Ohkura, H. Takeshita, and K. Kaji, Macromolecules **28**, 3168 (1995).

[15] H. Takeshita, T. Kanaya, K. Nishida, and K. Kaji, Macromolecules **32**, 7815 (1999).

[16] N. Takahashi,T. Kanaya, K. Nishida, and K. Kaji, Macromolecules **40**, 8750 (2007).

[17] S. J. Hong, P. D. Hong, J. Ch. Chen, and K. S. Shih, Eur. Polym. J. **45**, 1158 (2009).

[18] M. Ohkura, T. Kanaya, and K. Kaji, Polymer **33**, 3686 (1992).

[19] H. Takeshita, T. Kanaya, K. Nishida, and K. Kaji, Physica B **311**, 78 (2002).

[20] P.-D. Hong, J.-H. Chen, and H.-L. Wu, J. Appl. Polym. Sci. **69**, 2477 (1998).

[21] K. Yamaura, H. Kitahara, and T. Tanigami, J. Appl. Polym. Sci. **64**, 1283 (1996).

[22] F. A. Morrison, *Understanding Rheology* (Oxford University Press Inc., New York, 2001).

[23] R. G. Larson, *The Structure and Rheology of Complex Fluids* (Oxford University Press Inc., New York, 1999).

[24] J. H. Choi, S. W. Ko, B. C. Kim, J. Blackwell, and W. S. Lyoo, Macromolecules **34**, 2964 (2001).

[25] H. W. Gao, R. J. Yang, J. Y. He, and L. Yang, J. Appl. Polym. Sci. **116**, 1459 (2010).

[26] W. S. Lyoo, S. J. Lee, and J. H. Kim, J. Appl. Polym. Sci. **93**, 41 (2004).

[27] E. J. Lee, N. H. Kim, and K. S. Dan, J. Polym. Sci. Part B **42**, 1451 (2004).

[28] E. J. Lee, K. S. Dan, and B. C. Kim, J. Appl. Polym. Sci. **101**, 465 (2006).

[29] W. Brown, ed., *Dynamic Light Scattering: The Method and Some Applications* (Oxford University Press Inc., New York, 1993).

[30] A. L. Kjniksen and B. Nyström, Macromolecules **29**, 7116 (1996).

[31] N. Nemoto, A. Koike, and K. Osaki, Macromolecules **29**, 1445 (1996).

[32] T. Matsunaga and M. Shibayama, Phys. Rev. E **76**, 030401(R) (2007).

[33] M. Shibayama, Bull. Chem. Soc. Jpn. **79**, 1799 (2006).

[34] J. E. Martin and J. P. Wilcoxon, Phys. Rev. Lett. **61**, 373 (1988).

[35] M. Shibayama, S. Takata, and T. Norisuye, Physica A **249**, 245 (1998).

[36] M. Shibayama and T. Norisuye, Bull. Chem. Soc. Jpn. **75**, 641 (2002).

[37] J. W. Ruberti and G. J. C. Braithwaite, US Publication no. 20040092653. May 13, 2004.

[38] http://www.mathworks.com/matlabcentral/fileexchange/6523-rilt

[39] S. W. Provencher, Comput. Phys. Commun. **27**, 229 (1982).

[40] S. W. Provencher, Comp. Phys. Commun. **27**, 213 (1982).

[41] T. Narita, A. Knaebel, J.-P. Munch, and S. J. Candau, Macromolecules **34**, 8224 (2001).

[42] E. C. Cooper, P. Johnson, and A. M. Donald, Polymer **32**, 2815 (1991).

[43] B. R. Dasgupta, Sh.-Y. Tee, J. C. Crocker, B. J. Frisken, and D. A. Weitz, Phys. Rev. E **65**, 051505 (2002).

[44] S. I. Song and B. C. Kim, Polymer **45**, 2381 (2004).

[45] J. C. Scanlan and H. H. Winter, Macromolecules **24**, 47 (1991).

[46] A. Izuka, H. H. Winter, and T. Hashimoto, Macromolecules **25**, 2422 (1992).

[47] B. Nyström, J. Roots, A. Carlsson, and B. Lindman, Polymer **33**, 2875 (1992).

[48] B. Nyström, H. Walderhaug, and F. K. J. Hansen, J. Phys. Chem. **97**, 7743 (1993).

[49] N. P. Balsara, P. Stepanek, T. P. Lodge, and M. Tirell, Macromolecules **24**, 6227 (1991).

[50] E. Prokopová, P. Šern, and O. Quadrat, Colloid Polym. Sci. **263**, 899 (1985).

[51] N. Yang, J. L. Hutter, and J. R. de Bruyn, submitted to J. Rheol.

Chapter 6

Microrheology, Microstructure, and Aging of Physically Cross-Linked Poly(vinyl alcohol)/Poly(ethylene glycol) Blends

6.1 Introduction

Soft materials such as gels are typically structured on the microscopic scale, so bulk methods cannot completely define their viscoelastic properties. The techniques of microrheology have been developed to probe viscoelastic properties on the micron length scale [1, 2]. Microrheology involves extracting the local viscous and elastic moduli from measurements of the motion of small tracer particles suspended in the material [2, 3]. Techniques based on diffusing wave spectroscopy [3, 4], optical tweezers [5, 6], dynamic light scattering [7, 8, 9] and direct imaging of the thermal motion of tracer particles [10, 11] have been used to study the viscoelastic properties of complex fluids such as polymer solutions [3, 9, 12, 13], polymer gels [14, 15, 16, 17, 18, 19], clay suspensions [20, 21, 22] and biomacromolecules [23, 24, 25].

The bulk rheology of PVA solutions and gels has been studied in a number of recent papers. Lyoo *et al.* studied the effect of concentration and molecular weight on the rheological behavior of atactic PVA (in which, the chirality of successive monomers is random) and found that PVA polymers in high-concentration solutions were easily oriented by shear [26, 27]. Lee

et al. [28] found from the deviation of the master curve (superposition of the shear modulus at different time and temperature by shifting) that solutions of PVA in dimethyl sulfoxide were rheologically heterogeneous, although they were optically transparent. They also found that the gelation of PVA was strongly affected by shear rate [29] and proceeded differently depending on the PVA concentration [30]. They observed a well-defined gel transition for solutions above a critical concentration, while at lower concentrations gelation occurred gradually with no definite gel point. Previous studies of the microrheology of PVA materials have been limited. Narita *et al.* studied the microrheology of PVA solutions and chemically cross-linked gels using diffusing wave spectroscopy and compared the local elastic modulus with bulk results [17, 18], but we are not aware of any previous microrheological experiments on physically cross-linked PVA gels.

In the present work, we use microrheological techniques to study the gelation and phase separation of physically cross-linked PVA gels made by the theta-gel method [31, 32], in which a gelling agent, poly(ethylene glycol) (PEG), in our case, is added to the PVA solutions. We present the results of a microrheological study of the microphase separation and gelation over time of the PVA gels as a function of PEG concentration in the PVA solutions. We use dynamic light scattering to determine the mean–square displacement of small probe particles suspended in the material, from which the micron-scale viscous and elastic moduli can be obtained over a range of about five orders of magnitude in frequency. We also use video-based particle tracking to investigate the micron-scale inhomogeneity of the system. We study the changes in structure and viscoelastic properties that take place due to gelation as the material ages. The experimental details and data analysis are described in Section 6.2. The results are presented in Section 6.3 and discussed in Section 6.4. Conclusions are given in Section 6.5.

6.2 Experiment

6.2.1 Sample Preparation

PVA powder with a molecular weight M_w of 115 000 g/mol and PEG with M_w = 1 500 g/mol were purchased from Scientific Polymer Products, Inc (New York, US). They were used as received, without further purification. Fluorescent polystyrene microspheres with diameters of 110 ± 10 nm, 210 ± 10 nm and 520 ± 15 nm were purchased from Thermal Scientific, Inc (Fremont, CA, US). The microspheres were dispersed in milli-Q water at a volume fraction of 2×10^{-5} for dynamic light scattering experiments and 8×10^{-5} for particle tracking experiments and sonicated for 30 min to break up any clumps. The water used in the dynamic light scattering experiments was pre-filtered to remove dust and other suspended impurities using filters with a pore size of 0.2 μm. Concentrated solutions of 10 wt% PVA and blends of 10 % PVA with 3 %, 5 %, and 7 % PEG as described in Chapter 5 were prepared by weighing the components and dissolving them in water containing the polystyrene spheres at 85 °C in a covered conical flask, followed by stirring for 3 hours. The covered samples were then cooled to room temperature in the ambient air, which took about 40 mins. We observed that the microspheres tended to clump together when heated to 85 °C, so the solutions were sonicated again after preparation to break up the aggregates. Samples were poured into a cylindrical glass cuvette 10 mm in diameter and 130 mm in length for light scattering experiments, or loaded into a specially fabricated sample cell, described in detail below, for video particle tracking experiments.

6.2.2 Dynamic Light Scattering

Dynamic light scattering measurements were performed using an ALV-CGS3 spectrometer-goniometer equipped with a digital correlator and a 20 mW helium-neon laser with a wavelength of 632.8 nm. Most of our experiments were carried out at scattering angle of 60°, at

which the scattering from the spheres was at least 10 times larger than that measured for the polymer solution with no added spheres. At the volume fraction of probe particles used, the scattering from the particles dominates that of the polymer solution, while multiple scattering is negligible. Although the solution with the highest concentration of PEG becomes slightly cloudy a few hours after preparation, its transparency remains higher than 90%. All measurements were done at room temperature, 24 $\pm$ 1 °C.

The dynamic light scattering system measures the intensity autocorrelation function $g^{(2)}(\tau)$ of the scattered light intensity as a function of lag time τ. The correlation function of the scattered electric field $g^{(1)}(\tau)$ is then calculated from $g^{(2)}(\tau)$. Because all of our samples are ergodic (as discussed below), the scattering of the electric field is a Gaussian process, in which case $g^{(1)}(\tau)$ and $g^{(2)}(\tau)$ are related through the Siegert relation [33],

$$g^{(2)}(\tau) = 1 + \beta \left| g^{(1)}(\tau) \right|^2, \tag{6.1}$$

where $\beta = 0.36 \pm 0.03$ is an instrumental constant related to the finite area of the photodetector. The three-dimensional mean squared displacement, $\langle \Delta r^2(\tau) \rangle$, is related to $g^{(1)}(\tau)$ by [33]

$$g^{(1)}(\tau) = e^{-q^2 \left\langle \Delta r^2(\tau) \right\rangle / 6}, \tag{6.2}$$

where $q = (4\pi n/\lambda)\sin(\theta/2)$ is the magnitude of the scattering wavevector, λ the vacuum wavelength of the incident light, n the refractive index of the medium, and θ the scattering angle.

6.2.3 Video-Based Particle Tracking

The trajectories of microspheres suspended in the PVA/PEG samples were tracked using a Lumenera Infinity2 digital CCD camera (Lawrenceville, GA) attached to an Olympus IX2 inverted fluorescence microscope. Glass sample chambers were made by gluing three small glass pieces cut from a microscope slide onto a second slide with optical glue to form a U-

shaped wall. A cover slip was then glued on top to make a chamber 10 mm $\times$ 8 mm $\times$ 1 mm high. About 0.16 ml of the PVA/PEG solution was loaded into the chamber with a glass dropper, after which the chamber was sealed with vacuum grease. The samples were allowed to equilibrate at room temperature for one hour before measurements were started. Preliminary observations were made to ensure that there was no overall flow in the sample, e.g., due to leaks in the sample chamber.

The particles were fluorescence imaged using dark field illumination with a mercury lamp. The field of view typically contained up to 60 particles when a 40$\times$ objective was used. Images were recorded by a personal computer at a frame rate of 12 frames per second for 2 min, with the total number of frames recorded being limited by the computer's memory. The scale of the images was calibrated using an etched calibration slide. In order to limit changes in particle position during image acquisition while keeping the signal-to-noise ratio reasonable, an exposure time of about 25 ms (shorter than the time between frames, which was at least 80 ms) and a high intensity light source were used.

The particles were identified in the images and their trajectories analyzed using particle-tracking software written by Crocker and co-workers and described in detail in Refs. [10, 34]. The two-dimensional mean squared displacement $\langle \Delta r^2(\tau) \rangle$ of the moving particles was determined from their trajectories. The accuracy of the tracking software and the experimental setup was verified by analyzing the motion of fluorescent spheres with a diameter of 520 nm in water under the same experimental conditions as used for the main experiments. The uncertainty of $\langle \Delta r^2(\tau) \rangle$ was determined to be 3×10^{-4} μm^2 by imaging immobile particles glued to a glass slide, using the same exposure time and illumination source. The mean squared displacements measured for tracer particles in our PVA/PEG samples are typically at least an order of magnitude larger than this.

6.2.4 Microrheology

The mean squared displacement of a probe particle embedded in a complex fluid is directly related to the mechanical response of the medium surrounding the particle, both the dissipation of energy due to the viscous response and the storage of energy due to the elastic response. In a purely viscous material, the probe particle will diffuse freely, and its mean squared displacement will increase linearly with time. In a strongly elastic system, the particle's mean squared displacement will reach a plateau value $\langle \Delta r^2(\tau) \rangle_p$ which can be used to estimate the elastic modulus G_e of the medium through an energy balance argument [4, 35, 36]. The elastic modulus can be expressed as

$$G_e \approx k_B T / (\pi a \langle \Delta r^2(\tau) \rangle_p), \tag{6.3}$$

where k_B is the Boltzmann constant, T the temperature, and a the particle radius.

In the general case, both the microscopic viscous and elastic moduli can be determined from the mean squared displacement using the method introduced by Mason [12, 37], under the assumption that the Stokes-Einstein relation can be generalized to viscoelastic fluids. We convert the mean square displacement data obtained from our light scattering and particle tracking experiments to viscous and elastic moduli using a modified algebraic form of the generalized Stokes-Einstein equations introduced in Refs. [34, 38]. We calculate

$$|G^*(\omega)| = \frac{k_B T}{\pi a \langle r^2(1/\omega) \rangle \Gamma [1 + \alpha(\omega)] [1 + \beta(\omega)/2]}, \tag{6.4}$$

where

$$\alpha(\omega) = \frac{\mathrm{d} \ln \langle r^2(1/\omega) \rangle}{\mathrm{d} \ln \tau} |_{\tau = 1/\omega} \tag{6.5}$$

and

$$\beta(\omega) = \frac{\mathrm{d}^2 \ln \langle r^2(1/\omega) \rangle}{d(\ln \tau)^2}|_{\tau=1/\omega} \tag{6.6}$$

are the first- and second-order logarithmic derivatives of $\langle \Delta r^2(\tau) \rangle$, both evaluated at $\tau = 1/\omega$. Γ is the gamma function. The viscous modulus $G''(\omega)$ and elastic modulus $G'(\omega)$ are then given by

$$G''(\omega) = |G^*(\omega)| \left\{1/\left[1 + \beta'(\omega)\right]\right\} \sin\left[\frac{\pi\alpha'(\omega)}{2} - \beta'(\omega)\left[1 - \alpha'(\omega)\right]\left(\frac{\pi}{2} - 1\right)\right] \tag{6.7}$$

and

$$G'(\omega) = |G^*(\omega)| \left\{1/\left[1 + \beta'(\omega)\right]\right\} \cos\left[\frac{\pi\alpha'(\omega)}{2} - \beta'(\omega)\alpha'(\omega)\left(\frac{\pi}{2} - 1\right)\right], \tag{6.8}$$

respectively, where $\alpha'(\omega)$ and $\beta'(\omega)$ are the local first- and second-order logarithmic derivatives of $|G^*(\omega)|$. A second-order polynomial fit using a sliding Gaussian window is used to numerically calculate the logarithmic derivatives and to smooth the data. This method gives a better estimate of the moduli than Mason's original method [12, 37] when the mean squared displacement is highly curved [38, 19].

The range of accessible time (frequency) scales in the light scattering experiments is much wider than that in the video-based particle tracking experiments. However, the information obtained is different: the mean squared displacements obtained from light scattering are averages over all particles in the scattering volume, and thus result in averaged viscoelastic moduli. The concentrated PVA/PEG system is, however, expected to be inhomogeneous on small scales as a result of phase separation, so ensemble-averaged moduli may not completely describe the system. Video-based particle tracking uses the trajectories of individual tracer particles to determine the local viscoelastic properties, allowing study of the spatial heterogeneity.

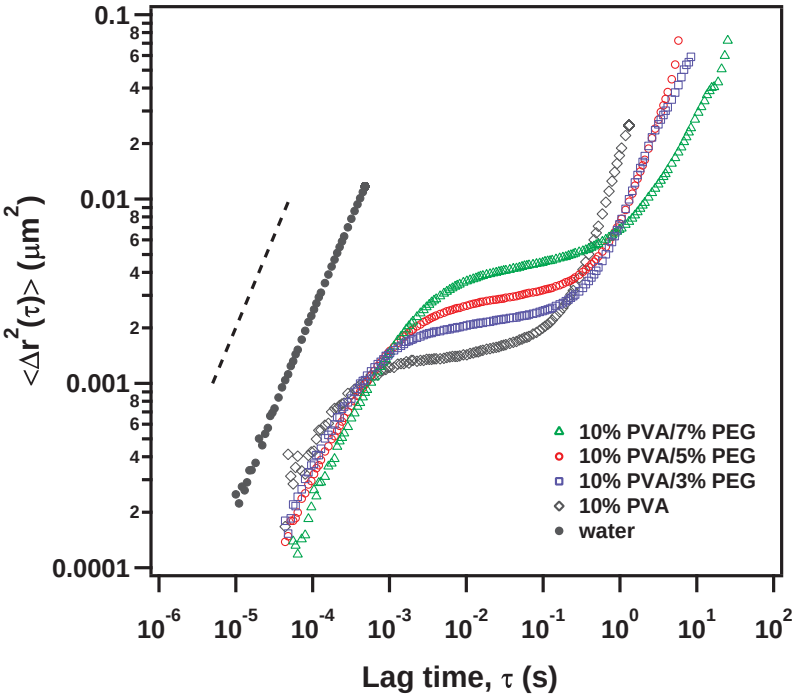

Figure 6.1: Mean square displacements of 110 nm microspheres measured from dynamic light scattering experiments in water (filled black circles), 10% PVA solution (black diamonds) and 10% PVA/PEG blends with PEG concentrations of 3% (blue squares), 5% (red circles) and 7% (green triangles). The dynamic light scattering experiments were done 1 hour after each sample was prepared. The dashed line has a slope of 1.

6.3 Results

6.3.1 Dynamic Light Scattering

Figure 6.1 shows the mean squared displacement $\langle \Delta r^2(\tau) \rangle$ obtained from light scattering from 110 nm probe particles suspended in blends of 10% PVA with 0%, 3%, 5% and 7% PEG. Data for the same sized particles in water are also shown. These experiments were done 1 hour after each sample was prepared. In water, $\langle \Delta r^2(\tau) \rangle$ increases linearly with time, indicating the purely diffusive motion of the particles. At short time scales ($\tau < 3 \times 10^{-4}$ s) the logarithmic slopes of $\langle \Delta r^2(\tau) \rangle$ in the polymer samples are very close to 1 as well, indicating that the motion of the microspheres in the polymers is near-diffusive in this range

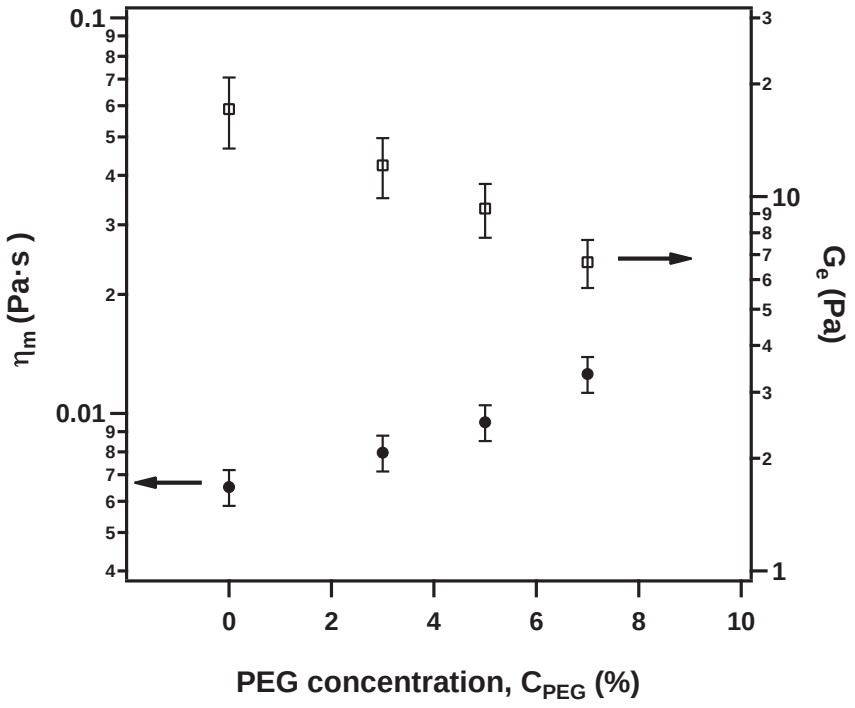

Figure 6.2: The filled circles show the microscopic viscosity η_m, computed from the $\langle \Delta r^2(\tau) \rangle$ data of Fig. 6.1 at short lag times. The local elasticity G_e obtained from the plateau of $\langle \Delta r^2(\tau) \rangle$ in Fig. 6.1 are plotted as open squares. Both are plotted as a function of PEG concentration.

of τ.

We can use the mean squared displacement for short times in this range of τ to compute the microscopic viscosity η_m from the Stokes-Einstein equation,

$$D = \frac{k_B T}{6\pi a \eta_m}, \tag{6.9}$$

where D is the diffusion coefficient and $\langle \Delta r^2(\tau) \rangle = 6D\tau$ for pure diffusion. The results are plotted as a function of PEG concentration c_{PEG} in Fig. 6.2. The uncertainty in the data is dominated by the polydispersity of the probe particles. We found η_m on this time scale to be 0.0065 ± 0.0006 Pa s for the 10% PVA solution. This is about six times larger than the viscosity of water and much smaller than the bulk viscosity of 2.87 Pa s measured with

a shear rheometer for a PVA sample of the same concentration as shown in Chapter 5 [39]. The microviscosity increases with PEG concentration, with $\eta_m = 0.013 \pm 0.001$ Pa s for the 10% PVA/7% PEG blend. Because $\langle \Delta r^2(\tau) \rangle$ from the dynamic light scattering is averaged over particles probing the material on the micron scale, we infer that the increase in η_m with PEG concentration is due to changes in the microrheological environment around the probe particles. The bulk viscosity, which is measured on a much larger length scale, shows a smaller relative increase (10% vs. 200%) to 3.15 Pa s for a 10% PVA/7% PEG blend. The difference between η_m and the bulk viscosity of each sample indicates the presence of micron-scale inhomogeneities in these materials, and that the PEG has a much larger effect on the micron-scale properties than on the bulk properties samples at this age.

At intermediate time scales (around 10^{-3} to 10^{0} s, depending on the concentration of PEG), each of the $\langle \Delta r^2(\tau) \rangle$ curves in Fig 6.1 shows a near-plateau, indicating that the motion of the probe particles becomes constrained by the surrounding medium. The logarithmic slope of $\langle \Delta r^2(\tau) \rangle$ increases again at high τ, however, approaching 1 for long lag times, showing that the probe particles are not permanently trapped by the material—the constraints eventually relax, allowing the particles to move more freely over longer times.

The plateau in $\langle \Delta r^2(\tau) \rangle$ could be due to the elasticity of the material as discussed above, or it could result from trapping of the probe particles in pores or “cages" formed by the surrounding material. In the former case, the product $\langle \Delta r^2(\tau) \rangle a$ should be independent of a, as implied by Eq. (6.3) [4, 35, 36]. Fig. 6.3 shows this quantity for three different values of a, for 1-day old samples of 10% PVA (Fig. 6.3(a)) and the 10% PVA/7% PEG blend (Fig. 6.3(b)). Results for two sizes of particles in water are also shown in Fig. 6.3(a) and overlap well within the experimental uncertainty. For the pure PVA solution, the three curves collapse reasonably well at short lag times and in the plateau region, but not at large τ. For the blend, the curves for the two smaller sized particles overlap very well for all τ, but the curve for the 520 nm particles lies above the other two curves. The overlap in the plateau region indicates that the restriction of particle motion at intermediate τ is due to elasticity. The difference observed for the 520 nm particles in the blend suggests that the

elastic properties of the surrounding medium are homogeneous on scales less than 200 nm but inhomogeneous on larger scales [2, 40]. We can estimate the local elasticity of the medium surrounding the probe particles from the plateau value of $\langle \Delta r^2(\tau) \rangle$ for the 110 nm particles. The results are plotted in Fig. 6.2, which shows that the elasticity on the 110 nm length scale decreases with increasing PEG concentration.

The mobility of the tracer particles changes significantly as the polymer blends age. This is illustrated in Fig. 6.4, which shows the mean squared displacements of the 110 nm tracer particles in a 10% PVA/7% PEG sample at different aging times. The values of $\langle \Delta r^2(\tau) \rangle$ at $\tau = 0.0002$ s, 0.02 s and 2 s are plotted as a function of aging time in Fig. 6.5(a). We also determined the logarithmic slopes α_1, α_2 and α_3 of $\langle \Delta r^2(\tau) \rangle$ at these short, intermediate and long lag times, respectively, as indicated in Fig. 6.4. These results are plotted in Fig. 6.5(b). At short times, $\langle \Delta r^2(\tau = 0.0002 \text{ s}) \rangle$ decreases until the 4th day and then stays around 0.0001 μm^2, but the logarithmic slope α_1 remains close to 1. This indicates that the particles continue to move diffusively on short time scales, but with a diffusion constant that decreases with age. In the intermediate-time regime, $\langle \Delta r^2(\tau = 0.02 \text{ s}) \rangle$ also decreases until the 4th day but then fluctuates with aging time. The logarithmic slope α_2 of the plateau regime increases until the 10th day, and then becomes roughly constant at around 0.2. In addition, the plateau region becomes narrower with aging as the short-time regime extends to longer τ and the long-time regime to shorter τ. α_3, the slope at long lag times, decreases from close to 1 for the fresh samples to 0.4 for samples that have aged for 27 days, although $\langle \Delta r^2(\tau = 2.0 \text{ s}) \rangle$ stays around 0.01 μm^2.

The frequency-dependent microscopic viscous and elastic moduli were calculated from $\langle \Delta r^2(\tau) \rangle$ using Eqs. (6.7) and (6.8). The moduli for fresh samples of 10% PVA and the PVA/PEG blends are shown in Figure 6.6. The behavior of G' and G'' as a function of ω is similar to that expected for an entangled polymer [41, 42]. Three distinct viscoelastic regimes are observed at low, intermediate and high frequencies. G'' dominates at low and high frequencies, while at intermediate frequencies $G' > G''$ and displays a broad plateau. The two crossover frequencies at which $G' = G''$ are plotted as function of PEG concentra-

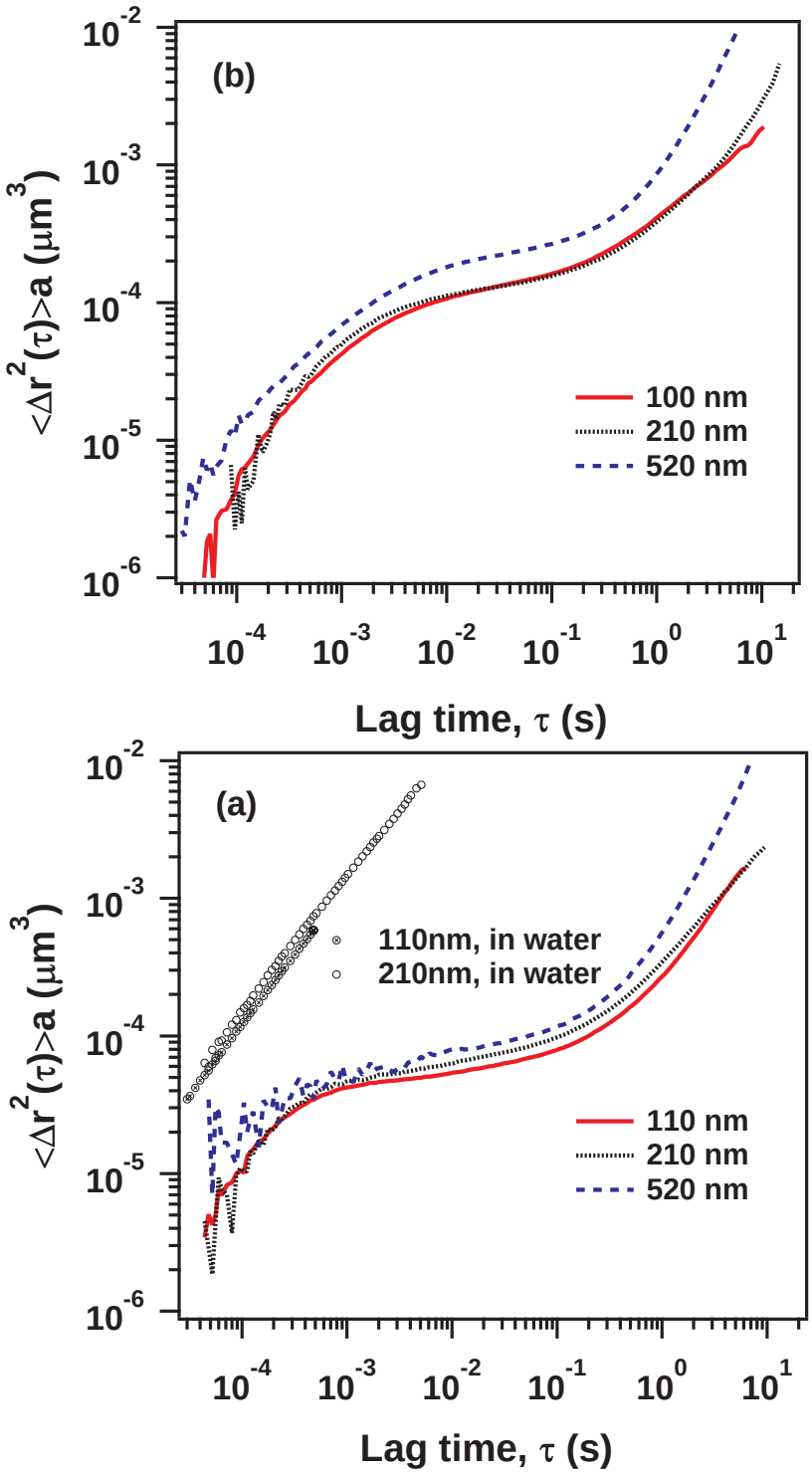

Figure 6.3: $\langle \Delta r^2(\tau) \rangle a$ for microspheres with different sizes measured from dynamic light scattering experiments in (a) a 10% PVA solution and (b) a 10% PVA/7% PEG blend. Scaled $\langle \Delta r^2(\tau) \rangle$ data for 110 nm and 210 nm microspheres in water are also shown in (a) for comparison (circles).

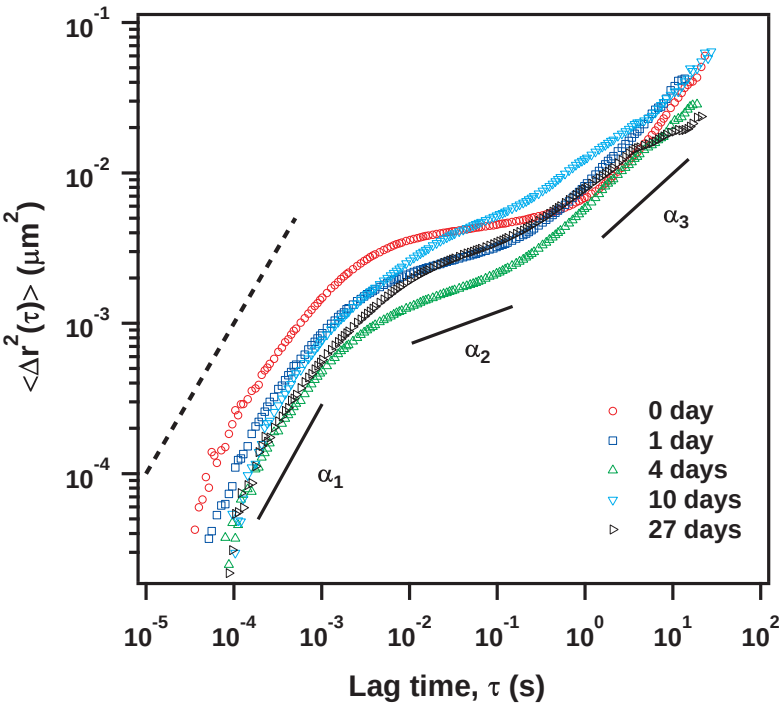

Figure 6.4: Mean square displacements of 110 nm microspheres measured from dynamic light scattering experiments in a 10% PVA/7% PEG blend at different aging times as indicated. The dashed line has a slope of 1. The line segments with slopes α_1, α_2 and α_3 schematically represent the behavior of $\langle \Delta r^2(\tau) \rangle$ at short, intermediate, and long times, respectively.

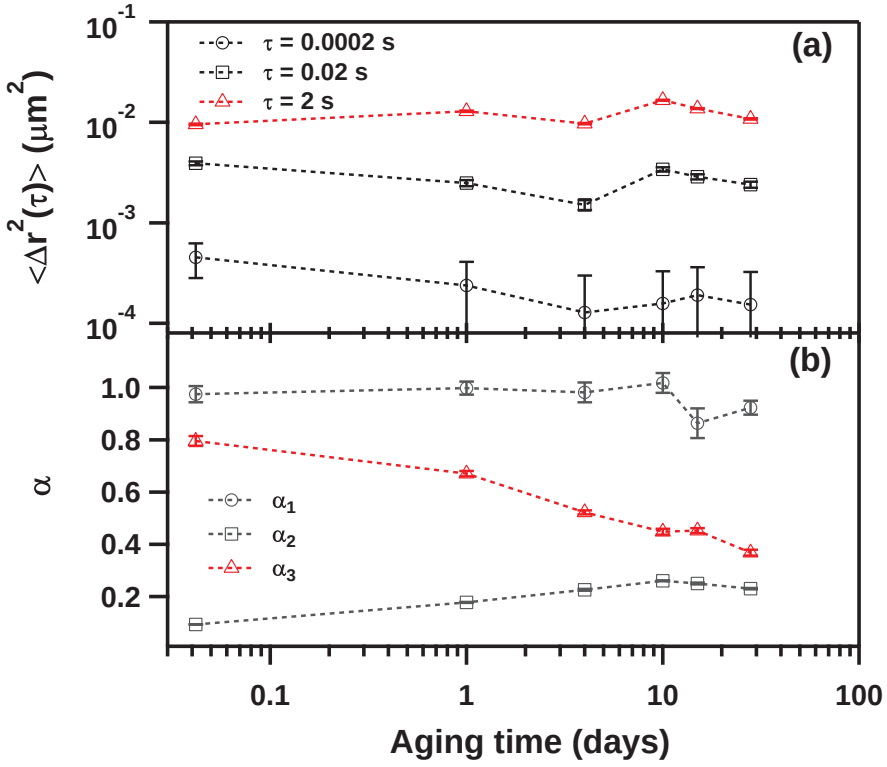

Figure 6.5: (a) Mean square displacement at three different lag times as a function of aging time for 110 nm tracer particles in a 10% PVA/7% PEG blend. The error bars are based on the uncertainty in the light scattering measurements. (b) The logarithmic slopes at short, intermediate, and long lag times as a function of aging time for tracer particles in a 10% PVA/7% PEG blend, with uncertainties due to the fits to $\langle \Delta r^2(\tau) \rangle$ at each time scales. The lines are to guide the eye.

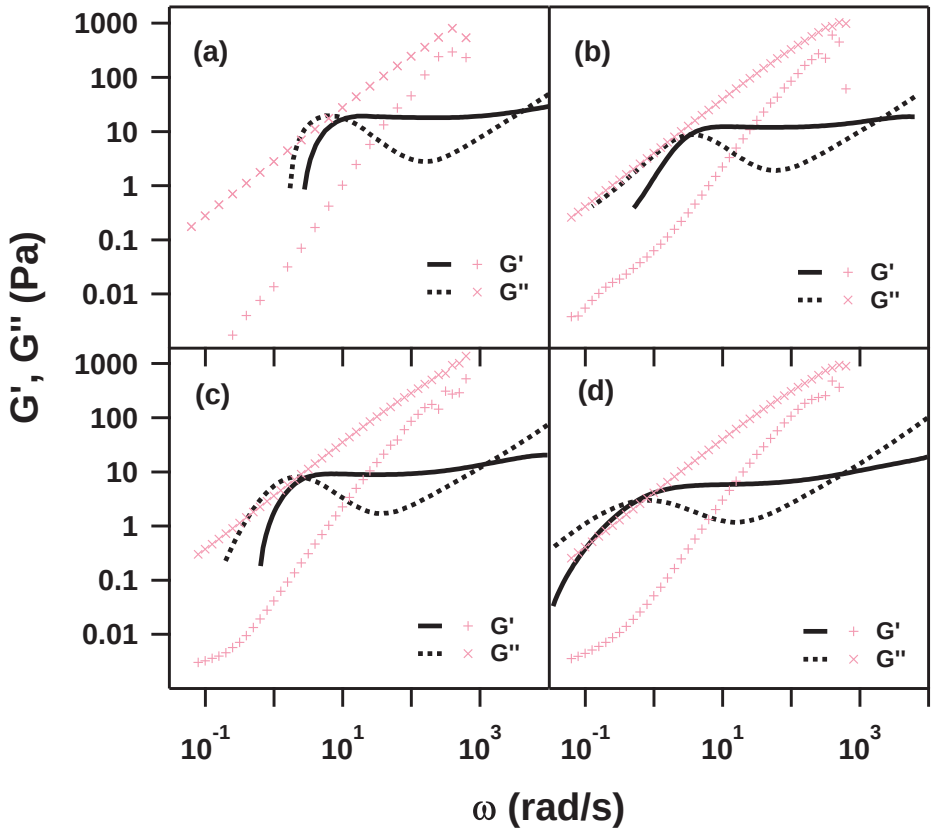

Figure 6.6: The microscopic viscous modulus (dashed lines) and elastic modulus (solid lines) calculated from the $\langle \Delta r^2(\tau) \rangle$ data shown in Fig. 6.1 using Eqs. (6.7) and (6.8) for fresh samples of (a) 10% PVA solution, (b) 10% PVA/3% PEG, (c) 10% PVA/5% PEG and (d) 10% PVA/7% PEG. + and × are the bulk values of $G'(\omega)$ and $G''(\omega)$, respectively, measured using small-amplitude oscillatory shear with a rheometer.

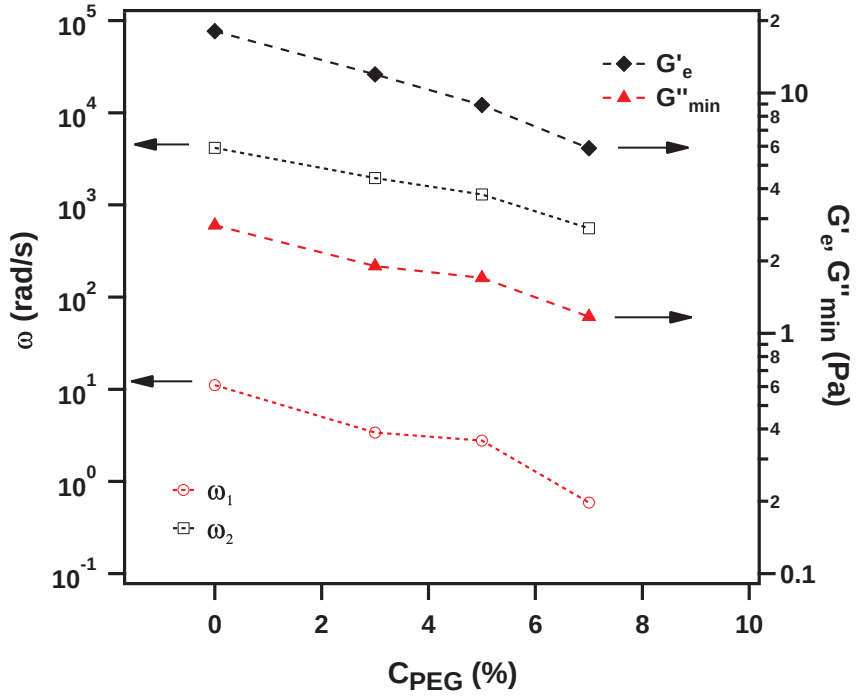

Figure 6.7: The open symbols show the crossover frequencies ω_1 and ω_2 at which $G' = G''$, obtained from the data in Fig. 6.6. The solid symbols are G''_{min}, the minimum value of the G'', and G'_e, the micro-elastic modulus at the same frequency.

tion in Fig. 6.7, along with G''_{min}, the minimum value of G'' in the intermediate frequency regime, and G'_e, the plateau value of G' determined at the same frequency. Both the low frequency crossover ω_1, corresponding to the slowest relaxation time τ_1, and the high frequency crossover ω_2, corresponding to the fastest relaxation time τ_2, decrease by about a factor of 10 as the concentration of PEG is increased. These results indicate that all of the relaxation processes probed by our tracer particles slow down as the concentration of PEG increases. In addition, the width of the plateau, characterized by the ratio ω_2/ω_1, increases slightly as the PEG concentration is increased. Both G'_e and G''_{min} decrease by a factor of about 3.

In the low-frequency regime, the microrheological moduli of the 10% PVA/3% PEG sample increase with frequency as $G' \propto \omega^{1.88\pm0.02}$ and $G'' \propto \omega^{1.097\pm0.004}$, while $G' \propto \omega^{1.72\pm0.04}$ and $G'' \propto \omega^{0.83\pm0.01}$ for the 10% PVA/7% PEG blend. The frequency range fitted is the lowest decade of each data set. The power law exponents in these cases are reasonably close to the values of 2 and 1 predicted by the Maxwell model [41, 42, 43]. The slightly lower exponents at the higher concentration may be due to polydispersity [9]. The steep increases in the low-frequency moduli observed for the other samples may be an artifact of the data analysis. At high frequencies, the moduli for all samples increase approximately as $G' \propto \omega^{0.21\pm0.03}$ and $G'' \propto \omega^{0.83\pm0.03}$.

The bulk viscous and elastic moduli for PVA and the PVA/PEG blends, measured with an AR 1500ex stress-controlled rheometer as shown in Chapter 5 [39], are also plotted in Fig. 6.6 for comparison. In contrast to the microrheological results, the bulk moduli increase with frequency and the viscous modulus dominates at all accessible frequencies. The data suggest a crossover frequency slightly above the maximum frequency studied, but no elastic plateau is accessible in our bulk-scale measurements. At low frequencies, the bulk values of the viscous modulus are similar to the microrheological values, while the bulk elastic modulus is much smaller than the microrheological G'. These differences indicate that the samples are inhomogeneous and that the bulk and microscopic rheology are determined by structure on different length scales. In addition, the bulk moduli do not change significantly as the PEG concentration is increased, while the microscopic moduli do, suggesting as above that the

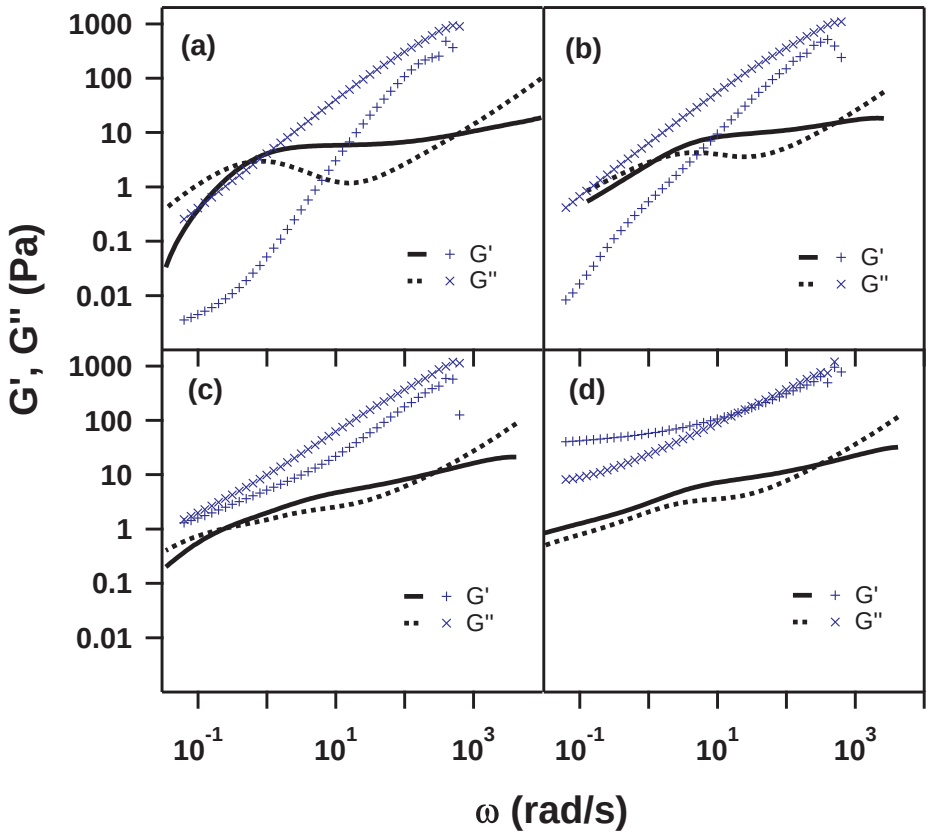

Figure 6.8: The microscopic viscous modulus (dashed lines) and elastic modulus (solid lines) calculated from the data shown in Fig. 6.4 for a 10% PVA/7% PEG blend. The sample ages are (a) 0 day, (b) 1 day, (c) 8 days and (d) 27 days. + and × are the bulk values of G' and G'', respectively, measured with a rheometer using small amplitude oscillatory shear.

bulk scale rheology is dominated by the PVA, while the effect of the small PEG molecules is much more significant on the microscale.

Fig. 6.8 shows the viscoelastic moduli for a 10% PVA/7% PEG blend at different aging times. The corresponding bulk rheometric moduli are also shown in Chapter 5 [39]. The low-frequency crossover of the microscopic moduli moves to lower frequency as the material ages, eventually moving out of the experimental frequency range, and the intermediate-frequency elastic plateau becomes less well-defined. In Fig. 6.8(d), corresponding an age of 27 days, G' is approximately parallel to G'' over much of the accessible frequency range, and both appear to be approaching a power law dependence on frequency. This suggests that the blend is

undergoing a gel transition as it ages [44, 45]. At low frequency the power law exponents for $G'(\omega)$ and $G''(\omega)$ are the same: $G' \propto \omega^{0.50\pm0.01}$ and $G'' \propto \omega^{0.499\pm0.004}$.

As above, the bulk moduli do not agree with the microrheological moduli, again indicating that the sample is inhomogeneous. However, the bulk moduli also show a gel transition as the material ages: the bulk elastic modulus increases with age and becomes greater than the bulk viscous modulus shortly after day 8. Around this age (Fig. 6.8(c)), the bulk values of both G' and G'' show a roughly power-law dependence on frequency, with approximately the same exponent: $G' \propto \omega^{0.84\pm0.02}$ and $G'' \propto \omega^{0.802\pm0.002}$. For older samples (Fig. 6.8(d)), $G' > G''$ on the bulk scale at low frequencies and G' approaches a finite limit as ω goes to zero. These results indicate a gel transition on the bulk scale at an age of approximately 8 days, substantially earlier than the transition observed with the 110 nm tracers. This scale dependence of the gel transition has been observed previously in a gelling clay suspension [20].

6.3.2 Video-Based Particle Tracking

The dynamic light scattering data presented in the previous section are an average over all the tracer particles in the scattering volume. The differences between the viscous and elastic moduli obtained from dynamic light scattering and those from bulk rheological measurements indicate, however, that the materials are heterogeneous on the micron scale. We therefore performed video-based particle tracking experiments using probe particles of 110 nm diameter to directly probe the local microrheological environments within the samples.

In Fig. 6.9 we plot the two-dimensional mean squared displacements determined from particle tracking experiments on all four materials. The data are averaged over all particles tracked over the course of the experiments. The behavior displayed in Fig. 6.9 is consistent with that observed in the dynamic light scattering experiments discussed above. The shortest lag times accessible in the dynamic light scattering experiments, at which $\langle \Delta r^2(\tau) \rangle$ increased

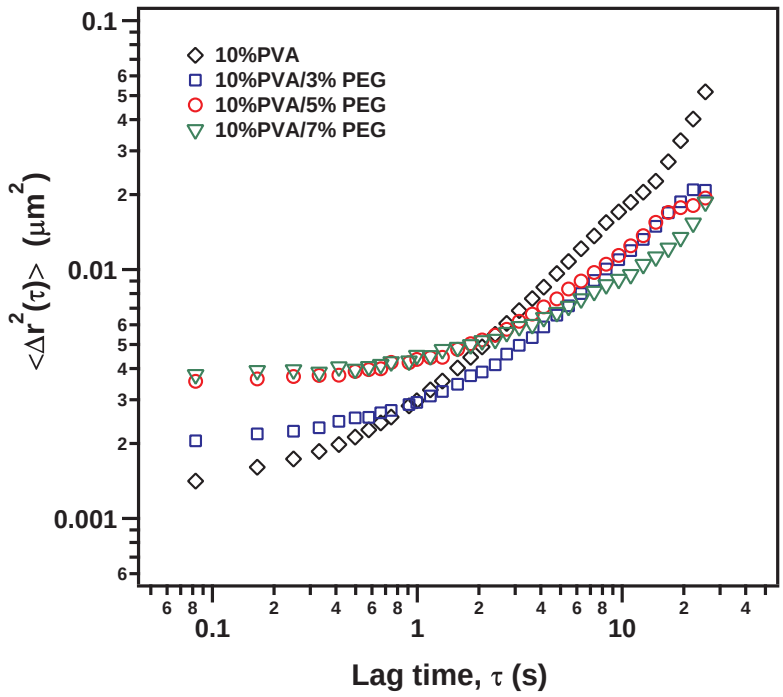

Figure 6.9: Mean square displacements of 110 nm microspheres measured from video-based particle tracking experiments in freshly prepared samples of: 10% PVA (diamonds), 10% PVA with 3% PEG (squares), 10% PVA with 5% PEG (circles), and 10% PVA with 7% PEG (triangles).

linearly, are not accessible in the particle tracking experiments. Thus the $\langle \Delta r^2(\tau) \rangle$ data in Fig. 6.9 show a plateau for $\tau \lesssim 0.4$ s, corresponding to the plateau in the dynamic light scattering data plotted in Fig. 6.1. $\langle \Delta r^2(\tau) \rangle$ increases at high τ. As the PEG concentration is increased, the plateau value of $\langle \Delta r^2(\tau) \rangle$ increases, as does the value of τ at which $\langle \Delta r^2(\tau) \rangle$ begins to increase. All of these results are in qualitative agreement with the dynamic light scattering experiments. There are quantitative differences, however, which may be due to aggregation of the tracer particles, despite our efforts to prevent it by sonication. Some aggregates were observed in the particle tracking data and eliminated from the analysis. These aggregates would presumably also be present in the light scattering studies, but in that case they cannot be eliminated. In this section, we examine the behavior of the individual probe particles and use the results to help us characterize the microstructure of the PVA/PEG materials.

The mean squared displacements of many individual particles in a freshly-made 10% PVA solution are shown in Fig. 6.10(a). Similar data for a freshly-made blend of 10% PVA and 7% PEG are shown in Fig. 6.11(a). In both figures, the curves span at least an order of magnitude in $\langle \Delta r^2(\tau) \rangle$ at a given τ, indicating that both samples are highly inhomogeneous. Some of the particles in the PVA solution (such as the one whose $\langle \Delta r^2(\tau) \rangle$ curve is labeled (i) in Fig. 6.10(a)) show nearly diffusive behavior over the full experimental range of τ. In contrast, others show strongly subdiffusive motion, such as those with $\langle \Delta r^2(\tau) \rangle$ labeled (ii) and (iii). For the latter particles, $\langle \Delta r^2(\tau) \rangle$ has a plateau at small τ, but increases at larger τ. Most of the particles in the 10% PVA/7% PEG blend move subdiffusively, as shown in Fig. 6.11(a). In some cases, such as the curve labeled (iv), $\langle \Delta r^2(\tau) \rangle$ again increases at long lag times following a flat regime at short τ, while for others (e.g., curve (v)), $\langle \Delta r^2(\tau) \rangle$ is almost flat over the full range of τ.

The distribution $P(\Delta x)$ of particle displacements Δx for a lagtime of 1 s is shown in Fig. 6.10(b) for the three particles with mean squared displacements labeled (i) to (iii) in Fig. 6.10(a). Similarly, the distributions corresponding to particles (iv) and (v) in Fig. 6.11(a) are shown in Fig. 6.11(b). All of these individual distributions are reasonably well described by

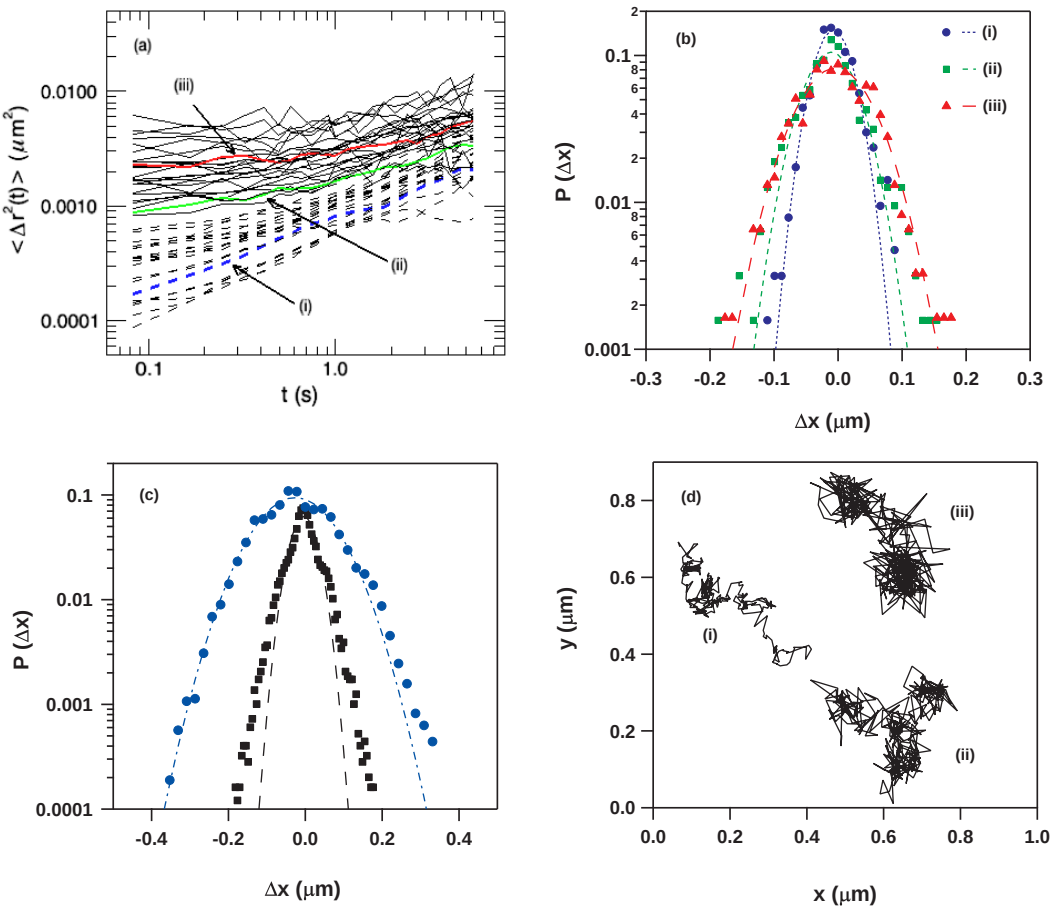

Figure 6.10: (a) Mean square displacements of individual 110 nm tracer particles in the 10% PVA solution. The measurements were performed 1 hour after the sample was prepared. The dashed lines are for particles with nearly diffusive motion and the solid lines for particles that are strongly subdiffusive at short τ. (b) Distribution of particle displacements at a lag time of 1 s for the particles labeled (i) to (iii) in (a). (c) The particle displacement distributions averaged over all particles at lag times $\tau = 1$ s (squares) and $\tau = 10$ s (circles). The dashed lines in (b) and (c) are fits to Gaussian functions. (d) Trajectories of particles (i) to (iii).

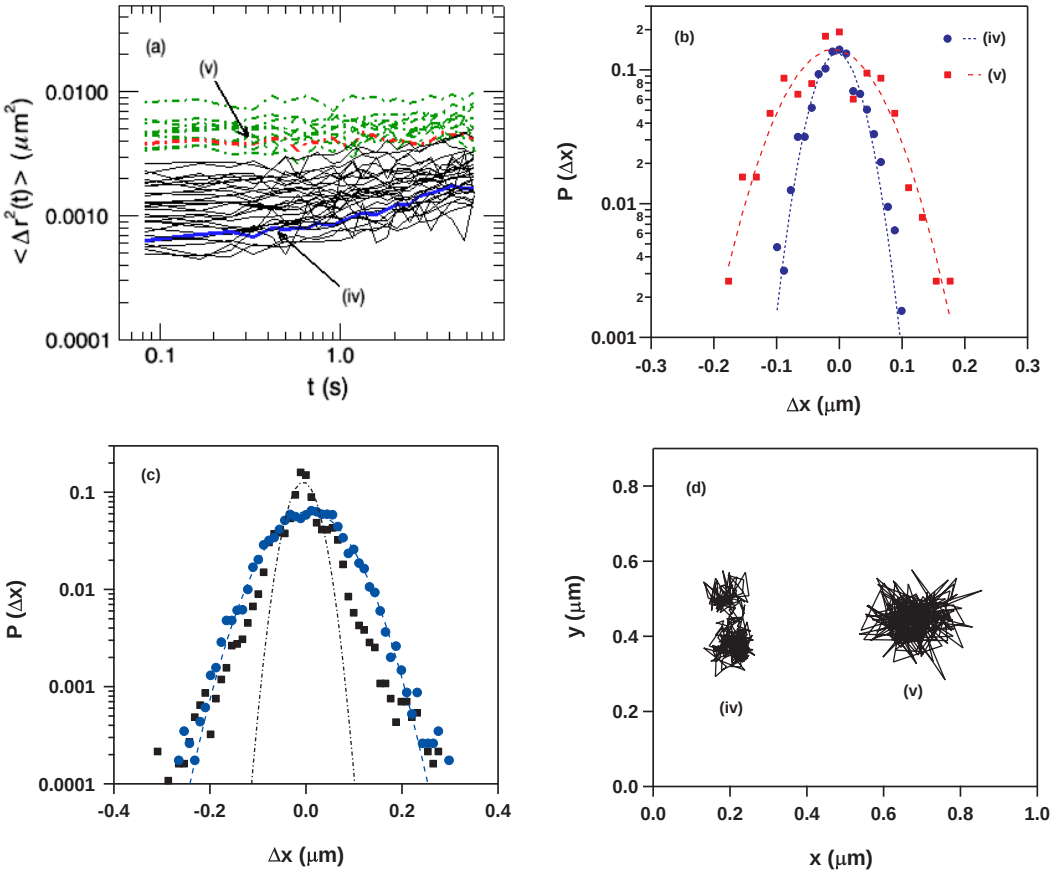

Figure 6.11: (a) Mean square displacements of individual 110 nm tracer particles in the 10% PVA/7% PEG blend. The measurements were performed 1 hour after the sample was prepared. The solid lines are for particles that are subdiffusive at short τ while the dot-dashed lines are for particles whose $\langle \Delta r^2(\tau) \rangle$ curves are nearly flat over all the accessible times. (b) Distribution of particle displacements at a lag time of 1 s for the particles labeled (iv) and (v) in (a). (c) The particle displacement distributions averaged over all particles at lag times $\tau = 1$ s (squares) and $\tau = 10$ s (circles). The dashed lines in (b) and (c) are fits to Gaussian functions. (d) Trajectories of particles (iv) and (v).

a Gaussian distribution, but with a different width for each particle. For a particle diffusing in a homogeneous medium, $P(\Delta x)$ is expected to be Gaussian with a width proportional to $\sqrt{D}$, where D is the diffusion coefficient of the medium [19, 46]. The different widths seen in Figs. 6.10(b) and 6.11(b) indicate that each particle sees a different rheological environment, confirming that the materials are inhomogeneous. Averaging $P(\Delta x)$ over all the tracked particles in the field of view for each sample for lag times τ=1 s and 10 s results in the distributions plotted in Fig. 6.10(c) and Fig. 6.11(c). For τ=1 s, the ensemble-averaged distributions are strongly non-Gaussian in both cases, even though the distributions for the individual particles are nearly Gaussian. This is due to the averaging of many individual distributions of different widths. At the longer lag time, the ensemble-averaged distributions are much more closely Gaussian, indicating that the media appear more homogeneous when sampled over longer times.

The trajectories of the individual particles singled out above are plotted in Figs. 6.10(d) and 6.11(d). Particle (*i*), for which $\langle \Delta r^2(\tau) \rangle$ is nearly linear, follows a path that is close to a random walk. Particles (*ii*) to (*iv*) are confined to a small region at short times then escape from one region to another over longer times. Particle (*v*) remains confined in one place for the entire observation time. As indicated in Fig. 6.10(d), the size of the regions to which the probe particles are confined is 50–150 nm for the 10% PVA solution, while it is 100–300 nm for the 10% PVA/7% PEG blend (Fig. 6.11(d)). The behaviors of the tracer particles in the other two blends are similar to those in the 10% PVA/7% PEG blend shown here. The confinement of the particles explains the non-Gaussian behavior of the ensemble-averaged $P(\Delta x)$ at short times while the hopping of particles from one region of confinement to another makes the motion diffusive over longer time scales [47]. We refer to the hopping of the particles between confining regions as dynamic caging, while a particle that remains trapped for the duration of the experiment we refer to as permanently caged. The scaling of the dynamic light scattering data with particle size, discussed above, indicates that the confinement results from the elasticity of the medium surrounding the tracer particles.

To gain some insight into the properties of the microrheological environments probed by

the tracers, we separate the tracers into three groups according to the behavior of their $\langle \Delta r^2(\tau) \rangle$ curves [14]. Group 1 has $\langle \Delta r^2(\tau) \rangle$ curves that are nearly linear, with an average slope greater than 0.7, corresponding to near-diffusive behavior. The $\langle \Delta r^2(\tau) \rangle$ curves for this group are plotted with dashed lines in Fig. 6.10(a). Group 2 has $\langle \Delta r^2(\tau) \rangle$ curves with slopes close to zero at short τ but rising to a value between 0.2 and 0.7 at long τ. Data for this group are plotted with solid lines in Fig. 6.10(a) and Fig. 6.11(a). Particles in this group generally show dynamic caging behavior as defined above. Particles in group 3 have $\langle \Delta r^2(\tau) \rangle$ curves that are almost flat, with slopes between 0 and 0.2 over the entire range of τ studied, and are plotted with dot-dashed lines in Fig. 6.11(a). These particles are typically permanently caged. From the average of the plateau of $\langle \Delta r^2(\tau) \rangle$ for groups 2 and 3, and using Eq. (6.3), we can estimate the elasticity G_e of the regions in which the particles display dynamic and permanent caging, respectively. We plot the results as a function of aging time for samples with different concentrations of PEG in Fig. 6.12. Generally, the elasticity seen by the particles which show dynamic caging is about five times higher than that seen by particles that are permanently caged. In both cases, the elasticity decreases over the first day of aging, then increases again over longer aging times. No clear effect of PEG concentration on the elasticities of the blends is observed.

The viscous and elastic moduli for groups 2 and 3 are also calculated from the mean square displacement using Eqs. (6.7) and (6.8). The results for the 10% PVA solution are shown in Fig. 6.13, in which plots (a) to (d) are for group 2 at different aging times and plots (e) to (g) are for group 3. For the particles which display dynamic caging (group 2), G'' is bigger than G' at low frequencies while the opposite is true at high frequencies. These data are reasonably well described by a Maxwell model with a single relaxation time as shown by the curves plotted in Fig. 6.13(c) [36, 48]. The crossover frequency is around 0.5 s^{-1} for the fresh material, but decreases to about 0.3 s^{-1} for samples that have aged one day or more. As for the dynamic light scattering data, the crossover is identified with the longest relaxation time of the material. Since the crossover frequency discussed here is obtained for particles in only one of the distinct populations (group 2), its value is different from that obtained from

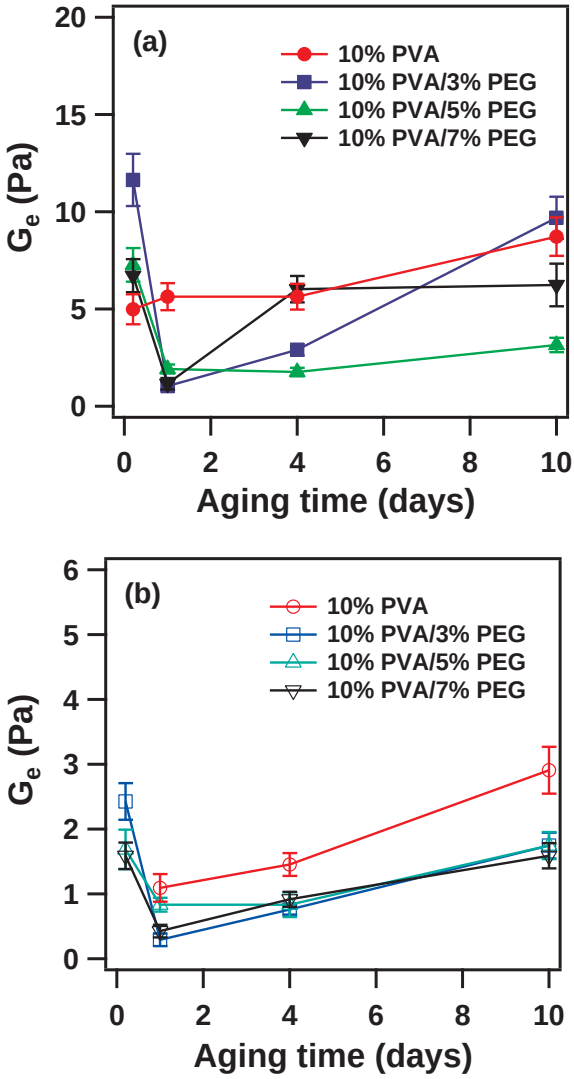

Figure 6.12: Elasticity as a function of aging time for (a) particles which show dynamic caging effects (group 2) and (b) particles which show permanent caging (group 3). G_e is estimated from the plateau of $\langle \Delta r^2(\tau) \rangle$ measured in the video particle tracking experiments. The uncertainties include those from the temperature fluctuation, the probe-size polydispersity, and the mean squared displacement measurements in the particle tracking experiments. Note that there are no particles in group 3 in the PVA solution at age 0.

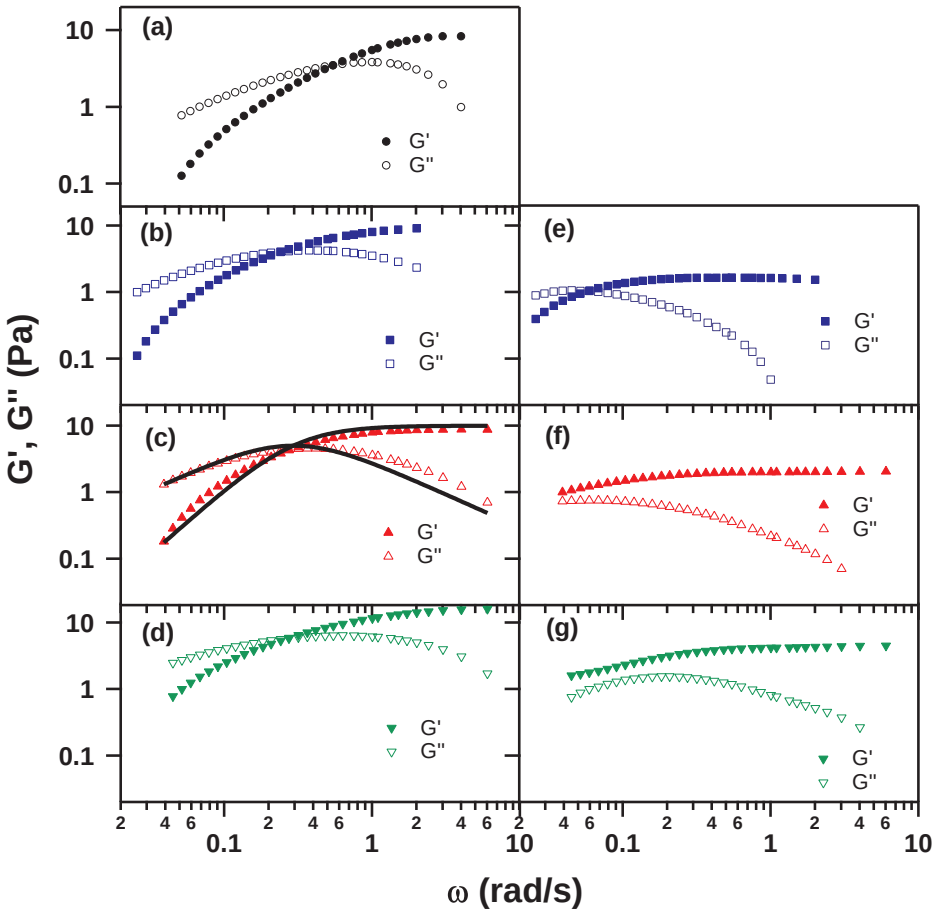

Figure 6.13: Viscous (open symbols) and elastic moduli (filled symbols) calculated from video particle tracking data for particles in a 10% PVA sample. (a) to (d) are for particles in group 2, which show dynamic caging, and (e) to (g) are for group 3, which show permanent caging. The different plots are for different aging times: (a) 0 day; (b) and (e) 1 day; (c) and (f) 4 days; (d) and (g) 10 days. There are no permanently caged particles in the pure PVA solution at age 0. The solid lines in (c) are fits to a Maxwell model.

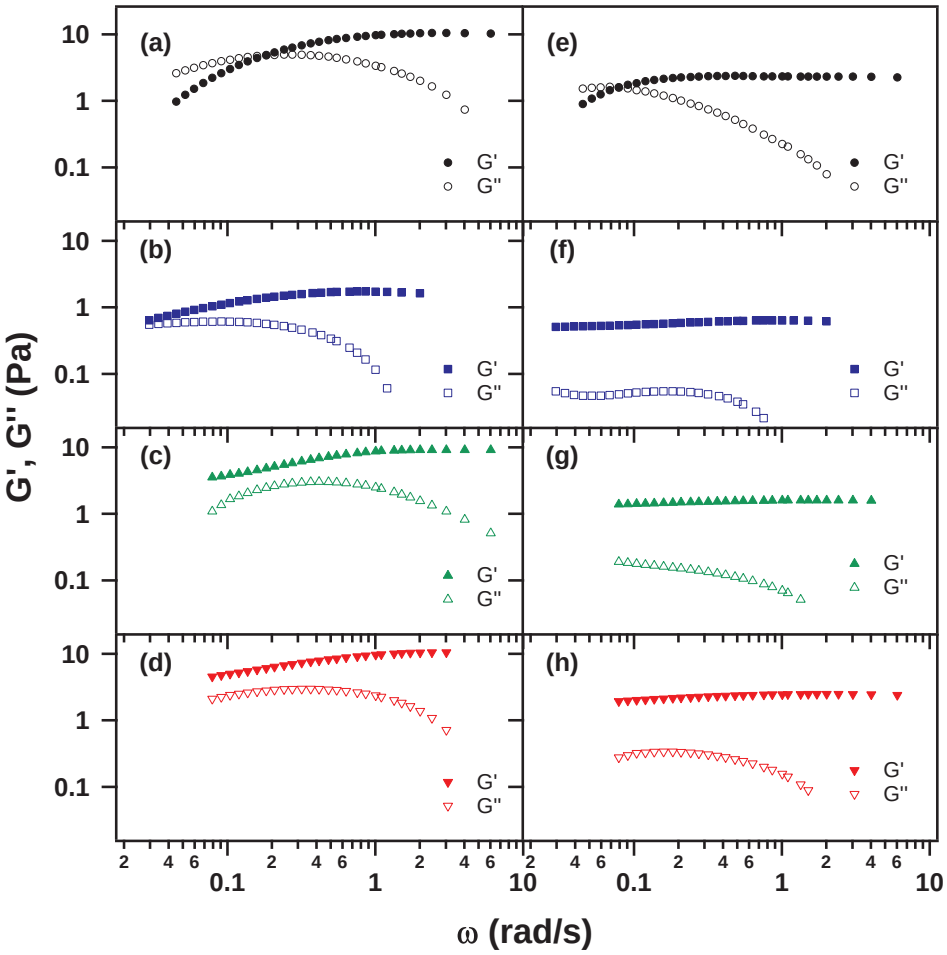

Figure 6.14: Viscous (open symbols) and elastic moduli (filled symbols) calculated from video particle tracking data for particles in a 10% PVA/7% PEG blend. (a) to (d) are for particles in group 2, which show dynamic caging, and (e) to (g) are for group 3, which show permanent caging. The different plots are for different aging times: (a) and (e) 0 day, (b) and (f) 1 day, (c) and (g) 4 days, and (d) and (h) 10 days.

dynamic light scattering. The group 3 data show a crossover at 0.2 s^{-1} at an age of 1 day, and the crossover evidently moves to lower frequency as the sample ages. $G' > G''$ over the entire accessible frequency range and both moduli increase with aging time. At an age of 10 days (Fig. 6.13(g)), G' and G'' are approximately parallel at low frequencies, suggesting that the system is approaching a gel transition.

The moduli for particles in groups 2 and 3 in the 10% PVA/7% PEG blend are shown in Fig. 6.14(a) to (d) and (e) to (h), respectively. In this case, a crossover is seen only for the fresh sample, shown in Fig. 6.14(a) and (e). After one day, the crossover frequency shifts to a frequency too low to be observed, as shown in Fig. 6.14(b) and (f). Comparison with Fig. 6.13 suggests that the relaxation times in the blend are much longer than those in the pure PVA solution, which is consistent with the dynamic light scattering results shown in Fig. 6.7. For older samples, $G' > G''$ for both groups. In (c) and (d) of Fig. 6.14, the values of both G' and G'' seen by the group 2 particles increase roughly as $\omega^{0.4}$ at low frequencies. On the other hand, G' as seen by the group 3 particles is almost independent of frequency. The rheological behavior seen by both groups is suggestive of a material gelling as it ages [44], with the group 3 particles showing gel behavior at day 1, and the group 2 particles at around day 4.

6.4 Discussion

The lag-time dependence of the mean-squared displacement of the tracer particles observed in our dynamic light scattering microrheology experiments is similar to that observed for linear polymer solutions and associative polymers [43, 9]. At short time scales, particles in the fresh PVA solution showed near-diffusive behavior, with a microscopic viscosity approximately six times higher than the viscosity of the solvent. In this regime, the particle displacements are small and their motion is not significantly restricted. The freshly-made PVA/PEG blends also showed near-diffusive behavior at short time scales, but the microscopic

viscosity η_m of the blends increased with PEG concentration. On the other hand, while the bulk viscosities of both the pure PVA solution and the PVA/PEG blends were much larger than their microscopic viscosities, they were not strongly dependent on PEG concentration. These results suggest that the PEG modifies the structure and rheology of these materials on the microscopic scale without strongly changing their macroscopic properties. On the other hand, addition of PEG has a strong effect on the gelation of these materials, as discussed below.

On intermediate time scales, $\langle \Delta r^2(\tau) \rangle$ showed a plateau regime, with a value that increased with PEG concentration. From the scaling of the mean squared displacement with the size of the tracer particles, we found that the plateau of $\langle \Delta r^2(\tau) \rangle$ results from restrictions of the tracer motion due to the elasticity of the materials. While plots of $\langle \Delta r^2(\tau) \rangle a$ overlapped for all tracer sizes studied in pure PVA, we observed a deviation from this scaling for the largest (520 nm) tracer particles in the 10% PVA/7%PEG blend. We interpret this to mean that elasticity remains the cause of the restricted tracer motion in the blend, but that the elasticity is not homogeneous on the scale of the largest particles.

The microscopic elastic modulus calculated from the plateau value of the mean squared displacement for the smallest (110 nm) tracer particles provides an indication of the rheological environment in the materials on this length scale. For the freshly-prepared materials, this quantity decreased with increasing PEG concentration. In contrast, the bulk-scale elastic moduli were an order of magnitude larger and independent of PEG concentration. This again indicates that the bulk rheological properties of the materials are largely determined by a large-scale PVA network. The smaller PEG molecules do not significantly affect the strength or structure of this network, but they do affect the micro-environment seen by the tracer particles.

The elastic confinement of the tracers is not permanent, however. The hydrogen bonds in the PVA network break and reform over longer time scales. This partially frees the tracer particles and causes the logarithmic slope of $\langle \Delta r^2(\tau) \rangle$ for both the fresh PVA solution and

the blends to increase to almost 1 at long τ, indicating that the tracers undergo near-diffusive motion over long time scales. Similar behavior has been observed in entangled linear polymer solutions [50], wormlike micelles [51], and associative polymers [9].

Linear viscoelasticity theory predicts that G' and G'' will increase as ω^2 and ω^1, respectively, at low frequencies. G' for a concentrated polymer solution displays a plateau at intermediate frequencies due to polymer entanglements, while Rouse dynamics predicts G' and $G'' \propto \omega^{1/2}$ at high frequencies [41, 42, 43, 49]. The microscopic moduli calculated from the motion of the microspheres in the fresh PVA solution and blends follow these predictions reasonably well at low frequency, although the low-frequency power law exponents found for the blends with higher PEG concentration are lower than the theoretical values. Similar behavior has been reported previously for other associative polymers [9, 43, 52, 53], and has been attributed to polydispersity. We do not observe behavior characteristic of Rouse dynamics at high frequencies, likely because the motion of the polymer molecules does not couple well to the tracer particles at high frequencies. Rouse-like behavior at high frequency was observed in Ref. [50] only when the tracer particles were actually bound to the polymer molecules.

The motion of the tracer particles and the viscoelastic properties of the pure PVA solution change extremely slowly with time, but the PVA/PEG blends show significant aging effects. Although the short-lag-time motion of the tracers remains diffusive, the microscopic viscosity increases with aging time, suggesting that the concentration of polymers surrounding the particles and/or the amount of hydrogen bonding between the polymers increases with time. The slope of the intermediate-τ plateau of $\langle \Delta r^2(\tau) \rangle$ increases, and the plateau itself becomes less distinct as the blends age. At high τ, the particle motion becomes subdiffusive with age. These results suggest that the aggregates in the blends grow larger and their distribution becomes broader with time, which in turn is a sign of gelation.

The frequency dependence of the microscopic elastic modulus in the intermediate frequency regime becomes stronger with age for the 10% PVA/7% PEG blend. We find $G' \propto \omega^{0.126 \pm 0.002}$ at an age of 1 day and $G' \propto \omega^{0.243 \pm 0.001}$ after 8 days. The weak frequency dependence of the

shear modulus is consistent with previous observations in associative polymers and polymer melts [9, 43, 54, 55], and has been attributed to the existence of fast Rouse motions of the polymer segments between entanglements or network points acting in addition to the slow reptation process.

At low frequencies, the microscopic value of $G'(\omega)$ obtained from dynamic light scattering experiments increases with aging time and its slope decreases until it becomes parallel with G'' at an age of 27 days. This is the gel point as measured on the scale of 110 nm tracer particles. It occurs much later than the bulk gel transition, which we observe from bulk rheology to take place at an age of about 8 days. Similar length-scale-dependent gelation has been observed previously in a colloidal suspension [20, 22]. We will discuss the gelation process in more detail below.

As discussed in Section 6.1, the blends phase separate into PVA-rich and PVA-poor domains when quenched, with a corresponding increase in c_{PEG} in the PVA-poor domains [31, 32]. The large range of $\langle \Delta r^2(\tau) \rangle$ observed in the video-based particle tracking experiments illustrates the resulting strong heterogeneity of the materials. After full phase separation, c_{PEG} becomes high (but may not reach the overlap concentration of 43% calculated for PEG with the molecular weight used here [56]) in the PVA-poor regions. In the absence of a PVA network, the elasticity felt by the tracer particles in the PVA-poor domains will likely be due to this high concentration of PEG molecules, as well as whatever free PVA molecules remain in these regions. On the other hand, the elasticity in the PVA-rich regions should come from aggregates of hydrogen-bonded and entangled PVA molecules. The smaller PEG molecules would be expected to have a much lower elasticity than the PVA aggregates, so the small-scale elastic modulus of a PVA-poor region should be lower than that of a PVA-rich region. Our data show that particles in group 3 see a lower G' than particles in group 2, from which we infer that group 3 particles must be moving in PVA-poor regions while group 2 particles are in the PVA-rich regions. Group 1 particles were only observed in the fresh PVA solution, suggesting that there are relatively large homogenous regions in the PVA solution when it is freshly made, but not at later ages and not in the blends.

On the other hand, the group 3 particles do not move as far as those in group 2, and are permanently trapped in regions of order 400 nm in size. We interpret this to mean that the PVA-poor regions are small pores surrounded by the PVA-rich network.

We found from the particle tracking experiments that the microscopic elasticity of freshly prepared blends is stronger than that of older samples. We interpret this to be due to the fact that the polymers in the fresh blends are highly entangled but not well phase-separated. The subsequent increase of G' for both the PVA-poor and PVA rich regions as the samples age further may be due to gelation. The data plotted in Fig. 6.12 do not show a clear dependence of the elasticity of either the PVA-rich or PVA-poor regions on c_{PEG}. This is consistent with the dynamic light scattering results, which showed that addition of PEG alters the microscopic viscosity, but does not affect the PVA networks. The relatively short PEG molecules have very little effect on the elasticity in the PVA-poor regions.

A gel transition results from the development of a percolation network which spans the sample. Although gelation has been studied in PVA materials [57, 58, 59, 60], there is no consensus about the details of the process [60]. PVA solutions have an upper-critical-solution-temperature-type phase diagram and phase separation is often concomitant with gelation upon cooling into the two-phase region [60]. Static light scattering and small angle neutron scattering measurements on PVA in a mixed solvent consisting of dimethyl sulfoxide and water showed that the system initially phase separated by spinodal decomposition into a bicontinuous structure of PVA-rich and PVA-poor phases [57, 58]. Gelation subsequently occurred in the PVA-rich regions [57, 58]. Recently, however, Talahashi et al. explained some results of their light scattering experiments on the PVA/dimethyl sulfoxide/water system by proposing that gelation occurs first and then induces phase separation [60].

Our experiments were performed on PVA and blends of PVA/PEG using pure water as a solvent, and so cannot be directly compared with the work of Ref. [60]. However, our results do not support the gelation-induced phase separation mechanism. First, we do not see evidence for gelation in our younger samples on either the bulk scale or the microscopic

scale. For the 10% PVA/7% PEG blend, our macroscopic rheology measurements showed that gelation occurred after about 8 days on the bulk scale, while the dynamic light scattering experiments showed a gel transition on the microscopic scale at an age of 27 days. On the other hand, these samples became slightly turbid within several hours of being cooled to room temperature, as mentioned in Sec. 6.3. Since turbidity is an indication of small scale heterogeneity, this indicates that phase separation occurs well before gelation in this blend. The different gel times observed by bulk rheology and dynamic light scattering indicate that the gel transition is length scale dependent and proceeds from large to small scales [9]. It is therefore unlikely that the early microscopic phase separation was induced by gelation. Further evidence showing the existence of phase separation before gelation comes from the shape of shear modulus from our oscillatory rheometry measurements. As seen in Fig. 6.6, we found G' to be roughly proportional to $\propto \omega^{0.5}$ at low frequencies for the freshly prepared blends. This weak frequency dependence is an indication of inhomogeneity due to phase separation [59]. More detailed rheological measurements presented in Chapter 5 [39] show that near the gel point of these PVA/PEG blends, $\tan\delta = G''/G'$ is smaller than one at low frequencies but greater than one at high frequencies. This behavior has been previously been interpreted as evidence that phase separation occurs before gelation [59].

Our results show that the addition of PEG to a PVA solution causes the system to phase separate into PVA-rich and PVA-poor domains when quenched to room temperature. Aggregates in the PVA-rich domains grow as the sample ages, and eventually form a continuous gel network. As discussed above, the gelation proceeds from large scales to smaller scales. However, even at the microscopic gel point seen in the light scattering data of Fig. 6.8(d), the motion of the tracer particles at the very short time scales (or very high frequencies) is still diffusive, indicating the existence of small regions which still have not gelled. At the bulk gel point, a fractal percolation network spans the sample and the material becomes predominately elastic. Although now a gel on the bulk scale, the sample still contains many small regions that remain fluid, and tracer particles in these regions continue to undergo restricted diffusion. As the sample ages further, these regions eventually gel as well.

6.5 Conclusion

We have carried out dynamic light scattering and video-based particle tracking experiments on tracer particles in PVA solutions and PVA/PEG blends. The use of dynamic light scattering allowed us to probe the ensemble-averaged motion of the tracer particles over a wide range of time scales, while the use of video-based particle tracking allowed us to probe the inhomogeneity of the samples. The results from the two techniques are consistent when their time scales overlapped. Combining them, we have developed an understanding of the evolution of the microstructure and microrheology of these physically cross-linked PVA-based materials as they age. Their microstructure is quite inhomogeneous both spatially and as function of time. Increasing the concentration of PEG alters the micro-rheological environment significantly but has little effect on the bulk properties. PEG also plays a role in the structural evolution of the materials over time since it induces gelation. We found that gelation occurs later on the microscopic scale than on the bulk scale, consistent with our previous work on the gelation of a clay suspension.

Our work gives some insight into the gelation process in these PVA blends, and in particular provides evidence that phase separation occurs before gelation in these materials, and that the gelation is induced by the micro-phase separation. As the refractive index of the separated phases are very similar, light scattering is not particularly useful for investigating the structure of the phase-separated blends, especially in the initial stages of the separation. A time-resolved small angle neutron scattering study of these blends as a function of c_{PEG} and aging time is currently being undertaken to provide further information on the microstructure and phase behavior of these materials.

BIBLIOGRAPHY

[1] T. M. Squires and T. G. Mason, Annu. Rev. Fluid Mech. **42**, 413 (2010).

[2] T. A. Waigh, Rep. Prog. Phys. **68**, 685 (2005).

[3] T. G. Mason and D. A. Weitz, Phys. Rev. Lett. **74**, 1250 (1995).

[4] T. G. Mason, H. Gang, and D. A. Weitz, J. Mol. Struct. **383**, 81 (1996).

[5] K. Svoboda and S. M. Blocks, Annu. Rev. Biophys. Biomol. Struct. **23**, 247 (1994).

[6] P. Bartlett, S. I. Henderson, and S. J. Mitchell, Phil. Trans. R. Soc. Lond. A **359**, 883 (2001).

[7] J. van der Gucht, N. A. M. Besseling, W. Knoben, L. Bouteiller, and M. A. Cohen Stuart, Phys. Rev. E. **67**, 051106 (2003).

[8] E. D. Cola, T. A. Weigh, and R. H. Colby, J. Polym. Sci. Pol. Phys. **45**, 774 (2007).

[9] F. K. Oppong and J. R. de Bruyn, Eur. Phys. J. E **31**, 25 (2010).

[10] J. C. Crocker and D. G. Grier, J. Colloid Interf. Sci. **179**, 298 (1996).

[11] Y. Tseng and D. Wirtz, Biophys. J. **81**, 1643 (2001).

[12] T. G. Mason, K. Ganesan, J. H. van zanten, D. Wirtz, and S. C. Kuo, Phys. Rev. Lett. **79**, 3282 (1997).

[13] B. Schnurr, F. Gittes, F. C. MacKintosh, and C. F. Schmidt, Macromolecules **30**, 7781 (1997).

[14] F. K. Oppong and J. R. de Bruyn, J. Non-Newton. Fluid. **142**, 104 (2007).

[15] F. K. Oppong, L. Rubatat, B. J. Frisken, A. E. Bailey, and J. R. de Bruyn, Phys. Rev. E. **73**, 041405 (2006).

[16] G. Nisato, P. Hebraud, J. P. Munch, and S. J. Candau, Phys. Rev. E. **61**, 2879 (2000).

[17] T. Narita, A. Knaebel, J. P. Munch, and S. J. Candau, Macromolecules **34**, 8224 (2001).

[18] T. Narita, A. Knaebel, J. P. Munch, M. Zrnyi, and S. J. Candau, Macromol. Symp. **207**, 17 (2004).

[19] B. R. Dasgupta and D. A. Weitz, Phys. Rev. E **71**, 021504 (2005).

[20] F. K. Oppong, P. Coussot, and J. R. de Bruyn, Phys. Rev. E **78**, 021405 (2008).

[21] H. A. Houghton, I. A. Hasnain, and A. M. Donald, Eur. Phys. J. E. **25**, 119 (2008).

[22] J. P. Rich, G. H. McKinley, and P. S. Doyle, J. Rheol. **55**, 273 (2011).

[23] J. Xu, A. Palmer, and D. Wirtz, Macromolecules **31** 6486 (1998).

[24] D. Velegol and F. Lanni, Biophys. J. **81**, 1786 (2001).

[25] J. Xu, Y. Tseng, C. J. Carriere, and D. Wirtz, Biomacromolecules **3**, 92 (2002).

[26] H. W. Gao, R. J. Yang, J. Y. He, and L. Yang, J. Appl. Polym. Sci. **116**, 1459 (2010).

[27] W. S. Lyoo, S. J. Lee, J. H. Kim, S. K. Noh, B. C. Ji, and B. C. Kim, J. Appl. Polym. Sci. **93**, 41 (2004).

[28] E. J. Lee, N. H. Kim, K. S. Dan, and B. C. Kim, J. Polym. Sci. Polym. Phys. **42**, 1451 (2004).

[29] E. J. Lee, K. S. Dan, and B. C. Kim, J. Appl. Polym. Sci. **101**, 465 (2006).

[30] J. H. Choi, S. W. Ko, B. C. Kim, J. Blackwell, and W. S. Lyoo, Macromolecules **34**, 2964 (2001).

[31] E. Oral, H. Bodugoz-Senturk, C. Macias, and O. K. Muratoglu, Nucl. Instrum. Meth. B **265**, 92 (2007).

[32] A. Dashevsky, A. R. Ahmed, J. Mota, M. Irfan, K. Kolter, and R. A. Bodmeier, Biomaterials **29**, 141 (2008).

[33] B. J. Berne, and R. Pecora, *Dynamic Light Scattering: With Applications to Chemistry, Biology, and Physics* (Wiley, New York, 1976).

[34] E. Weeks and J. C. Crocker, http://www.physics.emory.edu/∼weeks/idl/.

[35] M. L. Gardel, M. T. Valentine, and D. A. Weitz, http://squishycell.uchicago.edu/papers/urheo-chapter.pdf.

[36] D. van den Ende, E. H. Purnomo, M. H. G. Duits, W. Richterung, and F. Mugele, Phys. Rev. E **81**, 011404 (2010).

[37] T. G. Mason, Rheol. Acta **39**, 371 (2000).

[38] B. R. Dasgupta, S. Y. Tee, J. C. Crocker, B. J. Frisken, and D. A. Weitz, Phys. Rev. E **65**, 051505 (2002).

[39] N. Yang, J. L. Hutter, and J. de Bruyn, in preparation.

[40] I. Y. Wong, M. L. Gardel, D. R. Reichman, Eric R. Weeks, M. I. Valentine, A. R. Bausch, and D. A. Weitz, Phys. Rev. Lett. **92**, 178101 (2004).

[41] M. Doi and S. F. Edwards, *The Theory of Polymer Dynamics* (Oxford University Press, New York, 1986).

[42] J. E. Mark, et al., *Physical Properties of Polymers* (Cambridge University Press, Cambridge, 2004).

[43] A. Maestro, C. Gonzalez, and J. M. Gutierrez, J. Rheol. **46**, 127 (2002).

[44] F. Chambon and H. H. Winter, Polym. Bull. (Berlin) **13**, 499 (1985).

[45] H. H. Winter and M. Mours, Adv. Polym. Sci. **134**, 164 (1997).

[46] M. T. Valentine, P. D. Kaplan, D. Thota, J. C. Crocker, T. Gisler, R. K. Prud'Homme, M. Beck, and D. A. Weitz, Phys. Rev. E **64**, 061506 (2001).

[47] E. R. Weeks and D. A. Weitz, Phys. Rev. Lett. **89**, 095709 (2002).

[48] F. A. Morrison, *Understanding Rheology* (Oxford, New York, 2001).

[49] R. G. Larson, *The Structure and Rheology of Complex Fluids* (Oxford University Press, New York, 1999).

[50] J. Sprakel, J. van der Gucht, M. A. C. Stuart, and N. A. M. Besseling, Phys. Rev. E **46**, 061502 (2008).

[51] J. H. van Zanten and K. P. Rufener, Phys. Rev. E **62**, 5389 (2000).

[52] T. Svanholm, F. Molenaar, and A. Toussaint, Prog. Org. Coat. **30**, 159 (1997).

[53] L. Karlson, F. Joabson, and K. Thuresson, Carbohyd. Polym. **41**, 25 (2000).

[54] E. J. Regalado, J. Selb, and F. Candau, Macromolecules **32**, 8580 (1999).

[55] Y. H. Lin, J. Rheol. **28**, 1 (1984).

[56] K. Devanand, and J. C. Selser, Macromolecules **24**, 5943 (1991).

[57] T. Kanaya, M. Ohkura, H. Takeshita, K. Kaji, M. Furusaka, H. Yamaoka, and G. D. Wignall, Macromolecules **28**, 3168 (1995).

[58] H. Takeshita, T. Kanaya, K. Nishida, and K. Kaji, Macromolecules **32**, 7815 (1999).

[59] H. Takeshita, T. Kanaya, K. Nishida, and K. Kaji, Macromolecules **34**, 7894 (2001).

[60] N. Takahashi, T. Kanaya, K. Nishida, and K. Kaji, Macromolecules **40**, 8750 (2007).

Chapter 7

Summary and Discussion

7.1 Summary

In this thesis, we have presented the results of three studies aimed at understanding the micro-scale properties and structure of soft materials. We developed a technique to study the frequency-dependent surface microrheological behavior of poly(vinyl alcohol) (PVA) hydrogels using atomic force microscopy. We have studied the microstructure and microrheological properties of PVA-based physical gels during gelation, and investigated their relationship with the bulk-scale material properties.

7.1.1 The New Atomic Force Microscopy Technique for Measuring Viscoelasticity

We modified the electronic feedback circuit of an atomic force microscope by adding a small oscillatory voltage to the deflection signal to cause a vertical oscillatory motion of the sample. By monitoring the amplitude and phase of this motion via a lock-in amplifier, we determined the viscous and elastic moduli of the sample as a function of frequency during contact imaging. The main advantages of this technique over conventional atomic force microscopy-based techniques for measuring mechanical properties are that it can be done in imaging mode,

simplifying the setup and analysis, and that the excitation frequency can be easily varied.

This technique was applied to suspended PVA nanofibers and PVA hydrogels prepared by thermal cycling. The moduli of both the fibers and the hydrogels exhibit a significant frequency dependence, showing that static measurements are not sufficient to describe the mechanical properties of these materials. The Young's modulus of the fibers increased with frequency. Viscoelastic effects were evident in the hydrogels, with the storage modulus dominating the response of these materials at low frequency, and the loss modulus dominating at high frequency. We also found that the average modulus of the PVA hydrogel increased with the number of thermal cycles. The moduli varied from point to point on a given hydrogel sample by substantially more than the experimental uncertainties, confirming earlier reports that the hydrogel surface is nonuniform [1, 2].

7.1.2 Rheology and Structural Evolution of Poly(vinyl alcohol)/Poly(ethylene glycol)

Physically cross-linked polymer blends of concentrated PVA and poly(ethylene glycol) (PEG) undergo gelation as they age. We studied the rheology and structure of PVA/PEG blends as a function of PEG concentration and time. Using rheological and dynamic light scattering measurements, we found that shear, the concentration of PEG, and aging all affect the structure and properties of PVA materials. The changes in the bulk viscosity showed that moderate shear increased hydrogen bonding while stronger shear broke up the networks. PEG affected the microscopic environment, as shown by the increase in the fast relaxation time with increasing PEG concentration, but had little effect on the macroscale response of the samples at early ages, as indicated by the invariance of the slow relaxation time and the similarity in the viscosity and shear modulus at these ages. Both the rheological and dynamic light scattering results suggest that increasing the concentration of PEG leads to the formation of stronger physical gels and faster gelation.

We found that the blends were rheologically inhomogeneous due to the existence of micro-phase separation. The structure of the blends changed with aging time demonstrated by the changes in the fast and slow relaxation modes observed in the light scattering measurements. Our results suggest that the growth of aggregates in the phase-separated regions eventually resulted in the gelation of the blends. The gel point determined by dynamic light scattering was later than that determined by the bulk rheology, indicating that the gelation of the PVA/PEG gel proceeds from large to small scales.

7.1.3 Microstructure and Microrheology of Poly(vinyl alcohol)/Poly(ethylene glycol)

We investigated the microrheology and microstructure of the PVA/PEG blends by performing video particle tracking and dynamic light scattering experiments. Both techniques measure the thermal motion of small polystyrene spheres suspended in the materials. Dynamic light scattering allowed us to probe the ensemble-averaged motion of all the probe particles over a wide range of time scales, while video-based particle tracking allowed us to probe the inhomogeneity of the samples by analyzing the motion of individual particles.

We found that the microstructure of the PVA/PEG blends was quite inhomogeneous both spatially and as a function of time. Increasing the concentration of PEG altered the micro-rheological environment significantly but had little effect on the bulk properties. PEG also plays a key role in the structural evolution of the materials over time since it induces gelation. We again found that gelation occurs later on the microscopic scale than on the bulk scale, consistent with the results presented in Chapter 5. This work provides evidence that phase separation occurs before gelation in these materials, and that the gelation is induced by the micro-phase separation.

7.2 Discussion

7.2.1 Significance of Work

Our new AFM technique allowed us to measure the viscoelastic properties of soft materials during contact mode imaging. The set-up and the data analysis are simple, and the frequency is easy to control, allowing frequency-dependent properties to be determined. This allows mechanical properties to be determined at high spatial resolutions.

The use of the dynamic light scattering and microrheology techniques has enabled us to observe properties of our PVA-based materials which would not have been observed by conventional bulk rheometry. On the other hand, the use of parallel bulk measurements has allowed us to correlate the microscopic and bulk behavior of the materials. To the best of our knowledge, our work is the first microrheological study of physically cross-linked PVA gels.

Our results show that the structure of the PVA/PEG blends is inhomogeneous, and suggests the following gelation mechanism: The presence of PEG alters the micro-environment and forces the system to phase separate, inducing aggregation in the PVA-rich domains. The aggregates grow larger during aging and finally connect to form a gel network.

Our results also show that the gelation of PVA/PEG gels is length-scale dependent, occurring faster on the bulk scale than on the microscopic scale. This has been seen in other physical gels [3, 4], suggesting that this is a general feature of physical gelation.

7.2.2 Future Work

It has been reported that the mechanical properties of nano-fibers depend on diameter, with the elastic modulus increasing with decreasing diameter [5, 6]. It is not clear, however, if this

is an artifact due to the tip sliding along the fiber during force-volume imaging [5] or a real material effect [6]. Our AFM technique, with its small amplitude excitation, would be well suited to study this effect.

Our results showed that the microstructure of the PVA/PEG gels is inhomogeneous and that the rheological properties depended on the length scales probed. It would be interesting to perform microrheological measurements as a function of tracer particle size to get further information about the dependence of rheological properties of the PVA/PEG gels on length scale.

Another technique that could be used to study the length-scale dependent rheology of the material is two-point microrheology [7]. In this technique, the complex shear modulus $G^*(\omega)$ is determined by measuring the cross correlation in the thermal motion of pairs of tracer particles. By varying the distance between the two tracer particles considered, the microscopic properties can be examined as a function of length scale. The advantage of this technique is that the result does not depend on the size or shape of the tracer particles. Moreover, the cross correlation is dominated by the material properties between tracer particles, rather than their local environment. This technique can therefore be used to study the length-scale dependence of the rheological properties, and would provide more information about the microstructures of our PVA/PEG gels.

The inhomogeneous structure of the PVA/PEG blends is formed by phase-separation into PVA-rich and PEG-rich domains. Static scattering techniques can be used to study the morphology of these domains. As the refractive indices of the separated phases are very similar, light scattering is not particularly useful for this. Contrast between the two domains could be obtained by deuterating one of the polymers and performing a neutron scattering experiment. We have carried out a time-resolved small angle neutron scattering study of these blends as a function of PEG concentration and aging time to further investigate their microstructure and phase behavior. This work will be reported elsewhere.

Nuclear magnetic resonance (NMR) imaging could be used to establish the existence of crystalline structure in the PVA/PEG gels and to measure the degree of crystallinity [8]. Since the NMR frequency of protons depends strongly on their local environment, different peaks would be seen for hydrogen atoms in polymers in solution, and hydrogens in PVA crystals. Such measurements would provide more information about the structure and gelation mechanism in these materials.

BIBLIOGRAPHY

[1] L. E. Millon, M.-P. Nieh, J. L. Hutter, and W. K. Wan, Macromolecules **40** 3655 (2007).

[2] S. D. Hudson, J. L. Hutter, M.-P. Nieh, J. Pencer, L. E. Millon, and W. K. Wan, J. Chem. Phys. **130**, 034903 (2009).

[3] F. K. Oppong, P. Coussot, and J. R. de Bruyn, Phys. Rev. E **78**, 021405 (2008).

[4] J. P. Rich, G. H. McKinley, and P. S. Doyle, J. Rheol. **55**, 273 (2011).

[5] K. K. H. Wong, M. Zinke-Allmang, J. L. Hutter, S. Hrapovic, J. H. T. Luongd, W. K. Wan, Carbon **47**, 2571 (2009).

[6] S. Cuenot, C. Fretigny, S. Dmeoustier-Champagne S, and B. Nysten, Phys. Rev. B **69**, 165410 (2004).

[7] J. C. Crocker, M. T. Valentine, E. R. Weeks, T. Gisler, P. D. Kaplan, A. G. Yodh, and D. A. Weitz, Phys. Rev. Lett. **85**, 888 (2000).

[8] R. Ricciardi, F. Auriemma, C. Gaillet, C. De Rosa, and F. Laupretre, Macromolecules **37**, 9510 (2004).

Nan Yang

Condensed Matter Physics
Department of Physics and Astronomy
University of Western Ontario
1151 Richmond Street, London, Ontario

EDUCATION and DEGREES

M.Sci., Condensed Matter Physics
Jilin University, Changchun, China
2003 – 2006

B.Sci., Optical Information and Technology
Jilin University, Changchun, China
1999 - 2003

HONORS AND AWARDS

- Western Graduate Thesis Research Awards, 2010-2011
- Western Graduate Thesis Research Awards, 2009-2010
- Western SOGS Travel Award, 2008
- NSERC Best Female Poster Paper at Canadian Association of Physists Congress, 2008
- Best Student Poster-Presentation at Canadian Association of Physists Congress, 2008
- Western Graduate Thesis Research Awards, 2007-2008
- Western Graduate Research Scholarship, 2006--2011
- Western Graduate Teaching and Research Assistantship, 2006--2011
- Excellent Graduate Student of Jilin University Award, 2003-2004
- Second Class Academic Excellence Scholarship, 2002-2003
- Second Class Academic Excellence Scholarship, 2001-2002
- "Chi-Tian-Wen-Hao" Scholarship, 2000-2001
- Third Class Academic Excellence Scholarship, 2000-2001
- "Zhan-Hong" Societal Scholarship, 1999-2000
- First Class Academic Excellence Scholarship, 1999-2000

EMPLOYMENT

Teaching Assistant, University of Western Ontario, 2006-2011
Research Assistant, University of Western Ontario, 2006-2011

PUBLICATIONS

1. **N. Yang**, J. L. Hutter and J. R. de Bruyn, "Microrheology, microstructure and aging of physically cross-linked poly(vinyl alcohol)/poly(ethylene glycol) blends", under review.

2. **N. Yang**, J. L. Hutter and J. R. de Bruyn, "Rheology and dynamic structure evolution of poly(vinyl alcohol)-poly(ethylene glycol) blends during aging", in preparation.

3. **N. Yang**, K. K. Ho Wong, J. R. de Bruyn and J. L. Hutter, "Frequency-dependent viscoelasticity measurement by atomic force microscopy", *Measurement Science and Technology* **20**, 025703 (2009).

4. **N. Yang**, J. R. de Bruyn and J. L. Hutter, "Viscoelastic properties of poly(vinyl alcohol) nanofibres and hydrogels measured by atomic force microscopy", *Physics in Canada* **64**, 141 (2008).

5. K. Du, H. B. Yang, R. H. Wei, M. H. Li, Q. J. Yu, W. Y. Fu, **N. Yang**, H. Y. Zhu and Y. Zeng, "Electric-pulse discharge as a novel technique to synthesize-SiC nano-crystallites from liquid-phase organic precursors", *Materials Research Bulletin* **43**, 120-126 (2008).

6. **N. Yang**, H. B. Yang, J. J. Jia and X. F. Pang, "Formation and magnetic properties of nanosized $PbFe_{12}O_{19}$ particles synthesized by citrate precursor technique", *Journal of Alloys and Compounds* **438**, 263-267 (2007).

7. Y. Z. Fan, H. B. Yang, H. Y. Zhu, X. Zh. Liu, M. H. Li, Y. Q. Qu, **N. Yang** and G. T. Zou, "Metallization of carbon fibers with nickel by electroless plating technique", *Metallurgical and Materials Transactions A* **38**, 2148-2152 (2007).

8. **N. Yang**, H. B. Yang, Y. Q. Qu, Y. Z. Fan, L. X. Chang, H. Y. Zhu, M. H. Li and G. T. Zou, "Preparation of Cu-Zn/ZnO core-shell nanocomposite by surface modification and precipitation process in aqueous solution and its photoluminescence properties", *Materials Research Bulletin* **41**, 2154-2160 (2006).

9. Y. Q. Qu, H. B. Yang, **N. Yang**, Y. Z. Fan, H. Y. Zhu and G. T. Zou, "The effect of reaction temperature on the particle size, structure and magnetic properties of coprecipitated $CoFe_2O_4$ nanoparticles," *Materials Letters* **60**, 3548-3552 (2006).

10. L. X. Chang, H. B. Yang, W. Y. Fu, **N. Yang**, J. J. Chen, M. H. Li, G. T. Zou and J. X. Li, "Synthesis and thermal stability of W/WS_2 inorganic fullerene-like nanoparticles with core-shell structure", *Materials Research Bulletin* **41**, 1242-1248 (2006).

11. W. Y. Fu, H. B. Yang, M. H. Li, M. H. Li, **N. Yang** and G. T. Zou, "Anatase TiO_2 nanolayer coating on cobalt ferrite nanoparticles for magnetic photocatalyst," *Materials Letters* **59**, 3530-3534 (2005).